

# Fracture behaviour of clayey soils overlying cavities

Giulia Forlati

Dissertation submitted for the degree of Doctor of Philosophy at  
the University of Sheffield



The  
University  
Of  
Sheffield.

Department of Civil and Structural Engineering  
University of Sheffield

December 2016



# Declaration

I hereby declare that, except where specific reference is made to the work of others, the contents of this dissertation are entirely the result of my own work and include nothing, except where explicitly mentioned, that is the outcome of work done in collaboration. This dissertation is original and has not been submitted, in whole or part, for consideration for any degree, diploma or other qualifications to this university or any other institution.

December 2016



# Abstract

The frequent appearance of sinkholes has become a hazard due to their instantaneous development and the damage they can cause to infrastructure. The term sinkhole indicates a location in which the ground is sinking into cavities. The process is caused by water penetration into the ground. Water causes dissolution of soluble rocks in the bedrock resulting in the creation of a void and consequent collapse of the overlying soil. Water also affects the stability of voids from former old mine works. Despite the increasing interest in this phenomenon, rarely the geotechnical aspects of the event are studied. In particular, the characteristics of the soil standing over the cavity are usually neglected.

This research aimed to study clay behaviour in tensile conditions, investigating the effects of moisture content and plasticity index. The results will aid future research on the determination of a predictive model for sinkhole appearance. The project was divided into two parts: the first was based on the collection of data of previous events, the second was related to laboratory tests performed on small clay models. The creation of the historical database showed the importance of studying cohesive soils behaviour and common features of past sinkholes. The laboratory tests allowed the effect of moisture content and plasticity index on the fracture failure modes of clay to be determined. Two types of experiments were performed to study the instantaneous failure caused by cracks propagation: direct tensile and bending tests. The results found showed that fracture in clay is affected by both moisture content and plasticity index. High moisture contents determined gradual collapses in which clays underwent large deformations before reaching failure. This explained why sinkholes usually form after some time from the rain event. Instead, dry clays

iv

represent a more dangerous situation for their unexpected collapse without any deformation.

# Contents

<b>Declaration</b>	<b>i</b>
<b>Abstract</b>	<b>iii</b>
<b>Table of Contents</b>	<b>viii</b>
<b>List of Figures</b>	<b>xvi</b>
<b>List of Tables</b>	<b>xix</b>
<b>List of Symbols</b>	<b>xxi</b>
<b>List of Abbreviations</b>	<b>xxv</b>
<b>1 Introduction</b>	<b>1</b>
1.1 Objectives . . . . .	5
1.2 Thesis structure . . . . .	6
<b>2 Literature review</b>	<b>7</b>
2.1 Sinkholes . . . . .	7
2.1.1 Dropout sinkhole . . . . .	8
2.1.2 Past sinkhole events . . . . .	11
2.2 Fundamental concepts of unsaturated soils . . . . .	15
2.2.1 Stress state variables . . . . .	15
2.2.2 Soil-water characteristic curve . . . . .	16
2.3 Fundamental concepts of fracture mechanics . . . . .	18

2.3.1	Linear elastic fracture mechanics . . . . .	20
2.3.2	Elasto-plastic fracture mechanics . . . . .	24
2.4	Tensile tests on soils . . . . .	28
2.4.1	Direct tensile test . . . . .	29
2.4.2	Indirect tensile tests . . . . .	35
2.4.3	Results from the literature . . . . .	39
2.5	Fracture mechanics in soils . . . . .	42
2.5.1	Linear elastic fracture mechanics in soils . . . . .	44
2.5.2	Elasto plastic fracture mechanics in soils . . . . .	46
2.6	Summary . . . . .	52
<b>3</b>	<b>Experimental methodology</b>	<b>53</b>
3.1	Material selection . . . . .	53
3.1.1	Sample preparation . . . . .	55
3.2	Tensile test samples . . . . .	58
3.3	Bending test samples . . . . .	59
3.4	Drying analysis . . . . .	63
3.5	Test procedure . . . . .	64
3.6	GeoPIV . . . . .	68
3.7	Visual analysis . . . . .	71
3.8	Test limitations . . . . .	73
<b>4</b>	<b>Direct tensile test results</b>	<b>79</b>
4.1	Test results . . . . .	79
4.2	Tensile strength calculation . . . . .	83
4.3	Results discussion . . . . .	85
4.3.1	Kaolin . . . . .	86
4.3.2	Durham clay . . . . .	88
4.3.3	London clay . . . . .	89
4.3.4	Discussion . . . . .	91
4.3.5	Yield strength and initial Young's modulus . . . . .	95
4.3.6	Plasticity index . . . . .	98

4.4	Summary . . . . .	99
<b>5</b>	<b>Bending test results</b>	<b>101</b>
5.1	Test results . . . . .	101
5.2	Flexural strength calculation . . . . .	104
5.3	Results discussion . . . . .	108
5.3.1	Kaolin . . . . .	108
5.3.2	Durham clay . . . . .	108
5.3.3	London clay . . . . .	109
5.3.4	Discussion . . . . .	110
5.3.5	Plasticity index . . . . .	113
5.4	Summary . . . . .	115
<b>6</b>	<b>Analysis of fracture in bending tests</b>	<b>117</b>
6.1	Crack behaviour . . . . .	118
6.1.1	Crack initiation . . . . .	118
6.1.2	Crack extension . . . . .	121
6.1.3	GeoPIV . . . . .	121
6.2	Ductile cracks . . . . .	125
6.2.1	Crack-mouth opening $V_{pl}$ . . . . .	127
6.2.2	Crack opening angle COA . . . . .	130
6.2.3	Crack tip opening angle CTOA . . . . .	131
6.3	J-integral . . . . .	134
6.3.1	J-integral calculation . . . . .	135
6.3.2	Fracture toughness calculation . . . . .	138
6.4	Summary . . . . .	145
<b>7</b>	<b>Conclusions</b>	<b>147</b>
7.1	Main findings . . . . .	147
7.2	Potential use in design . . . . .	148
7.3	Suggestions for future research . . . . .	151
	<b>References</b>	<b>153</b>

<b>A Historical cases database</b>	<b>165</b>
<b>B Direct tensile test tables</b>	<b>179</b>
B.1 Tensile strength . . . . .	180
B.1.1 Kaolin . . . . .	180
B.1.2 Durham clay . . . . .	181
B.1.3 London clay . . . . .	182
B.2 Yield strength and Initial Young's modulus . . . . .	183
B.2.1 Kaolin . . . . .	183
B.2.2 Durham clay . . . . .	184
B.2.3 London clay . . . . .	185
<b>C Bending test tables</b>	<b>187</b>
C.1 Flexural strength . . . . .	188
C.1.1 Kaolin . . . . .	188
C.1.2 Durham clay . . . . .	190
C.1.3 London clay . . . . .	192

# List of Figures

1.1	Examples of sinkholes: a) collapse of a road in Fukuoka, Japan, in November 2016 (taken from ‘La Repubblica’ website, <a href="http://www.repubblica.it">www.repubblica.it</a> ); b) collapse of a garage in Ripon, UK, 1997 (taken from the BGS website, <a href="http://www.bgs.ac.uk">www.bgs.ac.uk</a> ) . . . . .	2
1.2	Map of the soil types across the UK (taken from the UK Soil Observatory website, <a href="http://www.ukso.org">www.ukso.org</a> ) . . . . .	4
1.3	Most recent map of the sinkholes occurred in February 2014 (taken from the British Geological Survey website, <a href="http://www.bgs.ac.uk">www.bgs.ac.uk</a> ) . . . . .	4
1.4	Parameters affecting sinkhole formation (taken from Waltham et al. (2005)) . . . . .	5
2.1	Types of sinkholes (taken from the British Geological Survey website, <a href="http://www.bgs.ac.uk">www.bgs.ac.uk</a> , 2011) . . . . .	9
2.2	Process of formation of a dropout sinkhole . . . . .	10
2.3	Mechanical model used to simplify the mechanism of sinkhole formation	12
2.4	Typical soil water characteristic curve (SWCC) taken from Fredlund et al. (2012) . . . . .	17
2.5	Filter paper a) calibration curve for the two filter papers most used, b) setup, c) relationship between water content of the filter paper and suction taken from Fredlund and Rahardjo (1993) . . . . .	18
2.6	Pressure plate (Soilmoisture, 2008) . . . . .	19
2.7	Tensiometer developed by Take (2003) for his investigation on the effects of climate changes on embankments . . . . .	19

2.8	Potential energy and applied force between particles at the atomic level (taken from Anderson (2005)). $k$ is the bond stiffness, $\lambda$ is the amplitude of the sine wave with which the cohesive force is simplified	21
2.9	Main types of cracks related to their load system (taken from Janssen et al. (2002)) . . . . .	21
2.10	Infinite plate with a crack of length $2a$ under tensile stress (taken from Anderson (2005)). $B$ is the plate width . . . . .	22
2.11	Fracture mechanics theories (taken from Anderson (2005)) . . . . .	23
2.12	Sketch of the crack tip plasticity zone (taken from Ewalds and Wanhill (1984)) . . . . .	24
2.13	Different theories of fracture mechanics and their applicability (taken from Janssen et al. (2002)) . . . . .	25
2.14	Stress-strain curve for a nonlinear response (taken from Ewalds and Wanhill (1984)) . . . . .	25
2.15	Crack tip opening displacement CTOD or $\delta$ (modified from Anderson (2005)) . . . . .	26
2.16	Parameters used for the calculation of the CTOD (modified from Anderson (2005)) . . . . .	26
2.17	Calculation process of the $J$ integral used by Landes and Begley (taken from Anderson (2005)). $U$ is the energy absorbed by the sample during the test, $P$ the load applied to the specimen, $\Delta$ is the displacement, $a$ the crack length . . . . .	28
2.18	Determination of $J_{Ic}$ showed in ASTM:E1820-15 (2015) for metals . . . . .	29
2.19	Direct tensile test setup adopted by Tschebotarioff et al. (1953) . . . . .	30
2.20	Direct tensile test setup and example of the loading curve of Trabelsi et al. (2012) tests . . . . .	30
2.21	Direct tensile test setup used by Divya et al. (2014) . . . . .	31
2.22	Direct tensile test setup and example of the loading curve of Wang et al. (2007 <i>b</i> ) tests . . . . .	32
2.23	Symbols used in Table 2.2 . . . . .	32
2.24	Direct tensile test setup adopted by Zeh and Witt (2007) . . . . .	33

2.25 Loading curve obtained for the direct tensile tests of Tang et al. (2015) 35

2.26 3-point bending configuration a) adopted by Hallett and Newson (2001) and b) the symbols used to describe the geometry of the specimen 36

2.27 Exponential, polynomial and bell-shaped trends of tensile strength  $\sigma_t$  taken from Trabelsi et al. (2012), Towner (1987) and Tang et al. (2015).  $\rho_d$  indicates the dry density at which the samples were tested 40

2.28 Approximation of the direct tensile results determined by Tang et al. (2015) (x-axis modified substituting the degree of saturation with the moisture content).  $\rho_d$  indicates the dry density at which the samples were tested . . . . . 41

2.29 Variation of tensile strain at failure in relation with the moisture content for a) Gault clay and b) Balderhead clay (from Ajaz and Parry (1975)) . . . . . 42

2.30 Relation between the Young’s modulus and the moisture content from by Amarasiri et al. (2011) . . . . . 43

2.31 Variation of the tensile strength in relation to the plasticity index (Fang and Hirst, 1973) . . . . . 43

2.32 Variation of the fracture toughness with the moisture content from Amarasiri et al. (2011). . . . . 45

2.33 Relationship between the fracture toughness  $K_{IC}$  and the moisture content taken from Wang et al. (2007a) . . . . . 46

2.34 Fracture energy  $G_F$  variation with the moisture content (taken from Amarasiri et al. (2011)) . . . . . 46

2.35 Crack tip plastic zone extension in dependence with the moisture content (taken from Amarasiri et al. (2011)) . . . . . 47

2.36 Linear variation between the fracture toughness  $K_{IC}$  and the tensile strength  $\sigma_t$  taken from Wang et al. (2007b) . . . . . 47

2.37 Stress-strain curves (a) for bending tests and (b) direct tensile tests on Gault clay (Ajaz and Parry, 1975) . . . . . 47

2.38  $J_R$  curves versus the resistant ligament length found by Chandler (1984) 48

2.39	Loading diagrams obtained by Hallett and Newson (2005) and stages of the crack development in a kaolin beam wetted with saline . . . .	48
2.40	Symbols adopted by Hallett and Newson (2005) to describe the ductile crack growth . . . . .	50
2.41	Difference in the crack formation in relation to the initial negative pore pressure (Thusyanthan et al., 2007) . . . . .	51
3.1	Particle size distribution of the kaolin, Durham and London clays . .	55
3.2	Kaolin sample extracted from a single height Rowe cell (a) and a Durham clay sample extracted from a double height Rowe cell (b) .	57
3.3	Specimens preparation from a Rowe cell sample . . . . .	57
3.4	Trial and final geometries tested during the direct tensile tests (dimensions in mm) . . . . .	60
3.5	Modified geometry adopted for samples made with Durham clay (dimensions in mm) . . . . .	61
3.6	Tensile sample fixed to the loading frame . . . . .	62
3.7	Preparation of samples in London clay to use in bending tests . . . .	63
3.8	Drying analysis on the clayey beams used during the laboratory tests	65
3.9	Simple load cell calibration in tensile conditions . . . . .	66
3.10	Load cell percent error under tension loads . . . . .	67
3.11	Relationship between the percent error and the tensile force calculated from the load cell calibration in tension . . . . .	67
3.12	Setup adopted during the 3-point bending tests . . . . .	68
3.13	Modeling flock on a kaolin clay beam . . . . .	71
3.14	Standard deviation calculated on the original images captured during the tests . . . . .	72
3.15	Standard deviation calculated on the greyscale images captured during the tests . . . . .	72
3.16	Standard deviation calculated on the enhanced grayscale images . .	73
3.17	K0d_2403_b1 not centred on the bending support and development of a mixed mode crack . . . . .	75

4.1	Specimen geometry and setup of the direct tensile test (dimensions in mm) . . . . .	80
4.2	Typical tensile load-displacement curves for Speswhite kaolin, London and Durham clay samples . . . . .	81
4.3	Example of London clay sample used in the direct tensile test: (a) at the end of the setup before the beginning of the test, (b) cracked at the end of the test . . . . .	81
4.4	Tensile force plateau for Speswhite kaolin, London and Durham clay samples . . . . .	84
4.5	Stress-strain graph for a Speswhite kaolin sample at $\omega = 32.3\%$ . . . . .	84
4.6	Stress-strain graph for a London clay sample at $\omega = 26.2\%$ . . . . .	85
4.7	Stress-strain graph for a Durham clay sample at $\omega = 18.8\%$ . . . . .	85
4.8	Tensile strength variation in kaolin samples related to the moisture content . . . . .	87
4.9	Tensile strength comparison between the Speswhite kaolin and the literature results taken from Lakshmikantha et al. (2008) (symbol L in the legend), Tang et al. (2015) (symbol T in the legend) . . . . .	87
4.10	Strain variation in kaolin samples related to the moisture content . . . . .	88
4.11	Tensile strength variation in Durham clay samples related to the moisture content . . . . .	89
4.12	Strain variation in Durham clay samples related to the moisture content . . . . .	89
4.13	Tensile strength variation in London clay samples related to the moisture content . . . . .	90
4.14	Strain variation in London clay samples related to the moisture content . . . . .	90
4.15	Relationship between the tensile strength and moisture content for the samples prepared with the three different clays . . . . .	91
4.16	Relationship between the strain at the tensile strength and moisture content for the samples prepared with the three different clays . . . . .	92
4.17	Kaolin, Durham and London clay approximation of the tensile strength . . . . .	93

4.18	Comparison between the exponential trendline found for kaolin, London, Durham clay and the trendline found in literature. The equations of the approximated lines are reported in Table 4.4 . . . . .	94
4.19	Relationship between the tensile yield strength $\sigma_{YS}$ and moisture content for the specimens prepared with the three different clays . . . .	96
4.20	Relationship between the Young's modulus $E_0$ and moisture content for the specimens prepared with the three different clays . . . . .	97
4.21	Approximation of the kaolin yield strength . . . . .	97
4.22	Approximation of the kaolin and London clay initial Young's modulus	98
4.23	Relationship between the plasticity index and the tensile strengths recorded at the peak and at the OMC . . . . .	99
5.1	Load-displacement graph for Speswhite kaolin (PI=31.0 %) beams at different moisture contents . . . . .	104
5.2	Load-displacement graph for Durham clay (PI=18.4 %) beams at different moisture contents . . . . .	105
5.3	Load-displacement graph for London clay (PI=41.8 %) beams at different moisture contents . . . . .	105
5.4	Average moisture contents around the central section of kaolin beams	106
5.5	Tensile strength for kaolin, Durham and London clays calculated using the Navier formula . . . . .	107
5.6	Bending symbols used by Indraratna and Lasek (1996) to calculate the tensile strain . . . . .	108
5.7	Kaolin, Durham and London clays strain recorded at the moment of maximum flexural strength . . . . .	109
5.8	Relationship between the peak load and the moisture content for the three different clays . . . . .	111
5.9	Kaolin tensile strengths calculated from bending and direct tensile tests	112
5.10	Durham clay tensile strengths calculated from bending and direct tensile tests . . . . .	113

5.11 London clay tensile strengths calculated from bending and direct tensile tests . . . . . 113

5.12 Comparison between flexural strength values found in literature and in this investigation . . . . . 114

5.13 Tensile strengths of the three clays calculated from both the tensile tests . . . . . 114

6.1 Notch geometry modification during the beam bending . . . . . 119

6.2 Initial configuration of the beam notch (a) and the deformed (blunted) notch with a crack developed from the tip (b) in test K0d\_2403\_b2 . . . . . 119

6.3 Relationship between the displacement at which the crack starts to be visible, the displacement at the peak load and the moisture content 120

6.4 Crack initiation in relation to the load-displacement graph . . . . . 120

6.5 Crack extension related to the amount of vertical displacement applied during the test . . . . . 122

6.6 Results of the PIV analysis on the beam K0d\_1609\_b2 with  $\omega = 45.2\%$  123

6.7 GeoPIV mesh used to analyse the beam K0d\_1609\_b2 with  $\omega = 45.2\%$  123

6.8 Horizontal displacements tracked in beam K0d\_1609\_b2 ( $\omega = 45.2\%$ ) 125

6.9 Rigid body movement in bending tests . . . . . 126

6.10 Horizontal displacement tracked in beam K90d\_1109\_b4 ( $\omega = 38.7\%$ ) 127

6.11 Crack tip opening displacement  $\delta_t$  calculated from the images analysis and from the GeoPIV . . . . . 127

6.12 Blunted notch seen during test K0d\_2403\_b2 . . . . . 128

6.13 Load-crack mouth displacement  $V_{pl}$  graph for the beam test K0d\_0903\_b1 128

6.14 Relationship between the crack-mouth opening  $V_{pl}$  and the vertical displacement . . . . . 129

6.15 Notch geometry modification in beam K0d\_0903\_b3 . . . . . 129

6.16 Relationship between the Crack Opening Angle COA and the normalised ligament length  $b/b_0$  . . . . . 131

6.17 Relationships between the logarithm of the ligament length $b$ and the vertical displacement. The equations of the linear relationships are reported in Table 6.2 . . . . .	132
6.18 Linear relationships between the vertical plastic displacement and the crack-mouth opening. The equations of the linear relationships are reported in Table 6.3 . . . . .	134
6.19 Calculation of the plastic area for the test K0d_2403_b2 ( $\omega = 42.9\%$ )	136
6.20 Different contributions in the calculation of the J-integral for the test K0d_2403_b2 ( $\omega = 42.9\%$ ) . . . . .	136
6.21 Typical curve obtained from metals in tensile conditions taken from ASTM:E1820-15 (2015) . . . . .	138
6.22 J-integral values calculated during the tests . . . . .	138
6.23 Range of values delimited by $\Delta a_{max}$ and $J_{max}$ for the test K0d_2403_b2 ( $\omega = 42.9\%$ ) . . . . .	140
6.24 J-R curve approximation for the test K0d_2403_b2 ( $\omega = 42.9\%$ ) . . . . .	141
6.25 J-R curve approximation for the kaolin tests calculated in the range $0 - \Delta a_{max}$ . . . . .	141
6.26 J- $\delta_t$ relationship and best linear approximation for the test K0d_0903_b1 ( $\omega = 43.9\%$ ) . . . . .	142
6.27 Blunting line drawn in relation to the R-curve for the test K0d_0903_b1 ( $\omega = 43.9\%$ ) . . . . .	143
6.28 Variation of the parameter $M$ in relation to the moisture content . . . . .	143
6.29 Graphic construction to determine $J_Q$ (N/m) for the test K0d_0903_b1 ( $\omega = 43.9\%$ ) . . . . .	145
6.30 Provisional fracture toughness $J_Q$ in relation to the variation of the moisture content . . . . .	145

# List of Tables

1.1	Examples of sinkhole events happened in the world and reported by the local news . . . . .	3
2.1	Summary of the data regarding past sinkhole events . . . . .	13
2.2	Dimensions of the samples tested in direct tensile tests found in the literature. The geometry symbols are shown in Figure 2.23 . . . . .	33
2.3	Physical properties of the clays tested in direct tensile tests used in literature. $\Delta\sigma_t$ is the tensile strength range of values in relation to the moisture content at which the samples were tested . . . . .	34
2.4	Dimensions of the samples tested in bending tests used in literature	37
2.5	Physical properties of the clays tested in bending tests used in literature	38
2.6	Parameters obtained by Hallett and Newson (2001) after studying soil beams in 3-point bending tests . . . . .	51
3.1	Geotechnical properties of the clays used for the laboratory experiments <sup>a</sup> indicates a value found in Glendinning et al. (2014) <sup>b</sup> average of the values found by Sivakumar et al. (2015), Mavroulidou et al. (2013) . . . . .	54
3.2	Pentax K10D specifications . . . . .	70
3.3	Geometry differences measured in the central section of the samples used in the direct tensile tests . . . . .	74
3.4	Variations in the beam geometry caused by the oven drying . . . . .	75
3.5	Displacements supported by the beams before the load was applied .	76

4.1 Summary of the moisture contents studied in the tensile tests.  $\Delta\omega = \omega_{max} - \omega_{min}$  . . . . . 82

4.2 Number of tensile tests performed for different moisture contents . . . . . 82

4.3 Summary of the direct tensile test results . . . . . 86

4.4 Approximation parameters for tensile strength values . . . . . 92

4.5 Variation of the tensile strength in specimens with the same moisture content  $\Delta\sigma = \sigma_{t,max} - \sigma_{t,min}$ ,  $\Delta\varepsilon = \varepsilon_{max} - \varepsilon_{min}$  . . . . . 95

4.6 Approximation parameters for yield strength values . . . . . 96

4.7 Approximation parameters for initial Young’s module values . . . . . 97

5.1 Summary of the moisture contents studied in the 3-point bending tests.  $\Delta\omega = \omega_{max} - \omega_{min}$  . . . . . 103

5.2 Summary table of the bending test results . . . . . 107

6.1 Fracture mechanics parameters determined from the 3-point bending tests performed on wet kaolin beams. The tests with the subscript ‘*a*’ are taken from Hallett and Newson (2001) . . . . . 133

6.2 Equations of the linear relationships between the logarithmic measurement of the ligament length *b* and the vertical displacement applied on the beams . . . . . 133

6.3 Equations of the linear relationships between the vertical displacement applied on the beams and the crack-mouth opening  $V_{pl}$  . . . . . 134

6.4 Fracture parameters related to the slope of the blunting line and the proposed fracture toughness . . . . . 142

A.1 Database of the past sinkholes cases . . . . . 166

A.2 Database of the past sinkholes cases . . . . . 167

A.3 Database of the past sinkholes cases . . . . . 168

A.4 Database of the past sinkholes cases . . . . . 169

A.5 Database of the past sinkholes cases . . . . . 170

A.6 Soil properties of the past sinkhole cases . . . . . 171

A.7 Soil properties of the past sinkhole cases . . . . . 172

A.8	Soil properties of the past sinkhole cases . . . . .	173
A.9	Soil properties of the past sinkhole cases . . . . .	174
A.10	Soil properties of the past sinkhole cases . . . . .	175
A.11	Soil properties of the past sinkhole cases . . . . .	176
A.12	Soil properties of the past sinkhole cases . . . . .	177
B.1	Tensile strength, moisture content and maximum strain for the kaolin tensile tests . . . . .	180
B.2	Tensile strength, moisture content and maximum strain for the Durham clay tensile tests . . . . .	181
B.3	Tensile strength, moisture content and maximum strain for the Lon- don clay tensile tests . . . . .	182
B.4	Initial Young's modulus and yield strength for the kaolin tensile tests	183
B.5	Initial Young's modulus and yield strength for the Durham clay tensile tests . . . . .	184
B.6	Initial Young's modulus and yield strength for the London clay tensile tests . . . . .	185
C.1	Peak loads, moisture contents and displacements at the point of max- imum load for the kaolin bending tests . . . . .	189
C.2	Peak loads, moisture contents and displacements at the point of max- imum load for the Durham clay bending tests . . . . .	191
C.3	Peak loads, moisture contents and displacements at the point of max- imum load for the London clay bending tests . . . . .	192



# List of Symbols

$a$	Crack length
$A$	Area
$b$	Resistant ligament. Distance between the physical crack tip and the specimen edge
$B$	Specimen width
$B_c$	Specimen width in the central section
$c$	Cohesion
$c_u$	Undrained shear strength
$d$	Depth of the sinkhole
$D$	Energy dissipation rate
$E$	Young's modulus
$E_0$	Initial Young's modulus
$G$	Energy release rate
$G_c$	Critical energy release rate
$G_s$	Specific gravity of solids
$H$	Depth from the bedrock to the surface
$H_l$	Height of the collapsed soil, layer's height over the soluble rocks
$H^*$	Depth from the underground cavity to the surface
$K_0$	Lateral earth pressure at rest
$K_I$	Stress intensity factory for mode I cracks
$K_{IC}$	Critical stress intensity factory for mode I cracks
$L$	Specimen length

$n$	Pore size
$P$	Force
$P_x$	External work
$q$	Point displacement
$r$	Rotational factor between 0 and 1
$r_y$	Length of the yielded region ahead the crack tip
$s$	Soil suction
$S$	Degree of saturation
$S_c$	Critical degree of saturation
$S_e$	Equivalent degree of saturation
$S_p$	Beam span
$S_r$	Residual degree of saturation
$U_a$	Change in the elastic energy due to the introduction of a crack in an element
$U_c$	Strain energy accumulated by the sample when the crack is present
$V_{pl}$	Crack mouth opening during the plastic phase
$w$	Weight
$W$	Specimen height
$\alpha$	Inverse value of the air-entry pressure
$\alpha_{g,pl}$	Crack tip opening angle
$\beta$	Shape factor determined as ratio between the length of the initial crack and the specimen height
$\gamma$	Specific weight
$\gamma_d$	Specific dry weight
$\delta$	Crack Tip Opening Displacement, CTOD
$\delta_t$	Crack Tip Opening Displacement at the crack formation
$\Delta$	Displacements
$\varepsilon$	Strain
$\eta$	Constant adopted to calculate the fracture toughness

$\nu$	Poisson's ratio
$\phi$	Angle of internal friction
$\rho$	Soil density
$\sigma$	Applied stress
$\sigma_{YS}$	Yield stress
$\sigma_t$	Tensile strength
$\sigma_{t,r}$	Residual tensile strength
$\omega$	Moisture content
$\emptyset$	Diameter



# List of Abbreviations

<i>AEV</i>	Air entry value
<i>COA</i>	Crack opening angle
<i>COD</i>	Crack opening displacement
<i>CTOA</i>	Crack tip opening angle
<i>CTOD</i>	Crack tip opening displacement
<i>EPFM</i>	Elasto-plastic fracture mechanics
<i>LEFM</i>	Linear elastic fracture mechanics
<i>LL</i>	Liquid limit
<i>PI</i>	Plasticity index
<i>PL</i>	Plastic limit
<i>SD</i>	Standard deviation
<i>SWCC</i>	Soil water characteristic curve (equal to SWRC)
<i>SWRC</i>	Soil water retention curve
<i>WT</i>	Water table



# Chapter 1

## Introduction

The collapse of the ground into underlying cavities is a common hazard in many countries due to the presence of karst terrain and mine workings (Figure 1.1(a)). This problem is widespread around the world as the news continuously reports (Table 1.1).

The UK is particularly affected by sinkholes, which have increased in the last 30 years as reported by the British Geological Society (BGS). For example numerous sinkholes can be counted in the city of Ripon, North Yorkshire, where frequent collapses have occurred since 1979. The last sinkhole reported from the BGS happened on the 10 November 2016. It had a 10 m diameter and extended to a depth of 5 m. In February 2014, again in Ripon, a house collapsed into a ground depression of depth 0.7 m after the development of large cracks on the walls of the building. Another example of similar soil collapse in Ripon is shown in Figure 1.1(b).

Limited research has been conducted into the problem, in most of the cases with a focus on sandy material behaviour. For this reason, a deeper investigation of cohesive soils prone to collapse is required to support the development of predictive methods for sinkhole formation. This is particularly important due to the ability of cohesive soil to be temporarily stable before collapse.

The increasing appearance of sinkholes in the UK is linked to three main factors:

- the change in weather characterised by the increase of exceptional rain events.
- the presence of soluble rock deposits across the UK.



(a)



(b)

Figure 1.1: Examples of sinkholes: a) collapse of a road in Fukuoka, Japan, in November 2016 (taken from ‘La Repubblica’ website, [www.repubblica.it](http://www.repubblica.it)); b) collapse of a garage in Ripon, UK, 1997 (taken from the BGS website, [www.bgs.ac.uk](http://www.bgs.ac.uk))

- the existence of abandoned mines.

According to the BGS, the wet climate that characterises the UK and the increase of exceptional rainstorms result in the dissolution of the underlying rocks and the formation of large cavities. Water infiltrates the soil reaching the soluble strata and then dissolves them generating cavities. Abandoned mine workings are also reached by infiltrating water. This creates preferred paths that cause the loss of stability as water collects in mine workings. At the same time, climate variations through wet and dry periods degrade the soil resistance causing mine instability.

Droughts or dry spells contribute to the formation of cracks in the soil mass which can be seen as infiltrating paths for water during the subsequent wet season. These two types of instability become dangerous because they lead to the collapse of the overlying soil.

In the UK, rock layers are covered by clays in most regions (Figure 1.2). Due to the ability of cohesive soils to temporarily span over cavities and to support deformations, collapses in clays are often unexpected and catastrophic. The map in Figure 1.3 shows most of the sinkholes that occurred in February 2014 happened where clayey strata were located. This month was exceptional for sinkhole formation, due to intense rainfall during that period.

Following the appearance of many sinkholes, predictive methods to assess the likelihood of sinkholes have become more pressing. This is made more difficult and more

<b>Date</b>	<b>Location</b>	<b>Damages</b>	<b>Dimensions</b>	<b>Source</b>
08/11/2016	Fukuoka, Japan	Swallowing of road sections near underground work	27 m wide, 30 m long, 15 m deep	CNN website
08/11/2016	Ripon, UK	Garden swallowing	20×10 m, unknown depth	The Guardian website
28/06/2016	Carmarthen-shire, Wales, UK	Damage to a house	9.1 m wide	South Wales Evening Post website
12/02/2014	Corvette Museum, Bowling Green, KY, USA	Swallowing of eight classic Corvettes	7.6 - 9.1 m deep, 12.2 m wide	Corvette Museum website
11/05/1981	Winter Park, Florida, USA	Swallowing of house, car dealership, five porches, parts of two streets, swimming pool	22.9 m deep, 106.7 m wide	The Guardian website
28/01/2013	Guangzhou, China	Swallowing of buildings	9 m deep, 100×300 m	The Telegraph website, National Geographic website
30/05/2013	Guatemala city, Guatemala	Swallowing of three-story factory	100 m deep, 20 m wide	National Geographic website
27/09/2015	Queensland, Australia	Swallowing of cars and tents	100 m wide, 100 m deep	The Guardian website

Table 1.1: Examples of sinkhole events happened in the world and reported by the local news



Figure 1.2: Map of the soil types across the UK (taken from the UK Soil Observatory website, [www.ukso.org](http://www.ukso.org))

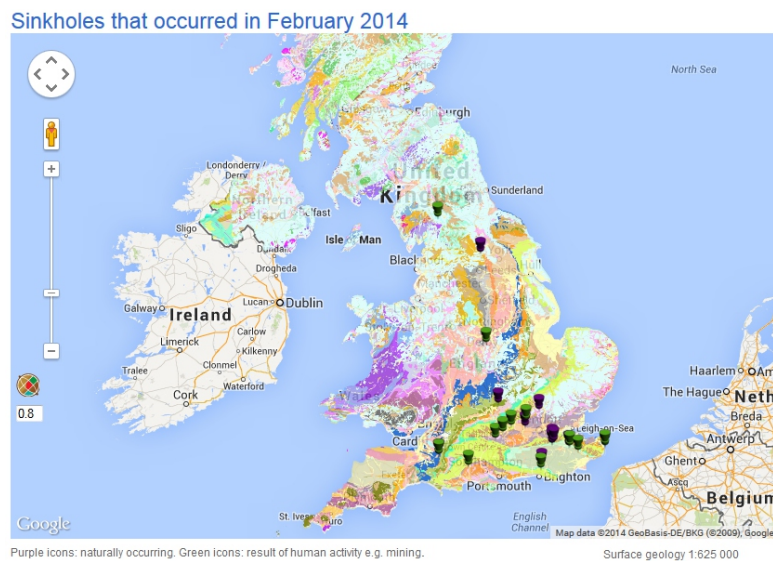


Figure 1.3: Most recent map of the sinkholes occurred in February 2014 (taken from the British Geological Survey website, [www.bgs.ac.uk](http://www.bgs.ac.uk))

important due to the catastrophic nature of sinkhole collapse events. Unfortunately, geotechnical investigations are not usually carried out after the events, as they are believed to be not important anymore. However, many authors have underlined

Observable parameters	Zhou <i>et al.</i> (2003)	Zisman (2001)	Edmonds (2001)	Van Rooy (1989)	Venter <i>et al.</i> (1987)
Bedrock type (lithology and fracturing)	✓		✓	✓	
Cover soil type (structure and strength properties)	✓	✓	✓	✓	✓
Rockhead depth	✓				
Rockhead nature (fissured or pinnacled)		✓			✓
Proximity to geological boundary or fault	✓		✓		
Topography (slope and position relative to thalweg)	✓		✓		
Local sinkholes (number, size, type)					
Distance to nearest sinkhole	✓				
Water table elevation (relative to rockhead)			✓		✓
Drainage history			✓	✓	✓
Ground investigation data if available					
SPT N-value of soils		✓			
Known geophysical anomalies	✓			✓	✓
Loss of drilling fluid, or caving of bored holes		✓			
Variable depths to water table in boreholes		✓			
Recorded ground settlement		✓			

SPT = standard penetration test.

Figure 1.4: Parameters affecting sinkhole formation (taken from Waltham et al. (2005))

the relevance of geotechnical characterisation of the soil overlying the rock cavity (Figure 1.4 taken from Waltham et al. (2005)).

## 1.1 Objectives

It is reasonable to hypothesise that cracks can develop along the bottom edge of the layer of soil cover, as the tensile force determines stresses that exceed the tensile strength of the material. The propensity for crack formation must therefore influence the collapse point and the formation of a sinkhole.

This research aimed to study the behaviour of clays in tensile and bending conditions demonstrating the relationship of the fracture behaviour with varying moisture content and plasticity index, in order to define trends that can be used in predictive calculations for sinkhole formation.

This has been achieved by:

- creating a database of geotechnical information regarding historical data of sinkholes in clayey soils. These data demonstrate the need to study cohesive soil behaviour. They show common features or trends between sinkhole events reported around the world.

- determining the influence of plasticity index and moisture content on clay behaviour. The maximum load and strain that cohesive soils can sustain is related to the moisture content at which they are undergoing tensile and bending deformations. Moisture content governs the soil failure mechanism.
- applying elasto-plastic fracture mechanics theory to understand the geotechnical performance of fracturing clays. Linear elastic fracture mechanics (LEFM) is not sufficient to explain the fracture formation. The application of the elasto-plastic fracture mechanic (EPFM) is considered more appropriate to study nonlinear material behaviour.

## 1.2 Thesis structure

The thesis is divided into seven chapters. The following bullet-points outline the contents of each chapter.

- **Chapter 2** reviews the geotechnical characteristics of some past events of sink-holes and analyses previous research conducted on fracture mechanics when applied to soils.
- **Chapter 3** describes the methodology used to study the behaviour of soils in tensile and bending conditions.
- **Chapter 4** outlines the results obtained from the direct tensile tests performed on clay samples.
- **Chapter 5** outlines the results obtained from the bending tests performed on clay samples.
- **Chapter 6** discusses the application of fracture mechanics theories to the bending tests.
- **Chapter 7** presents the conclusions and further developments to the research.

## Chapter 2

# Literature review

This chapter is divided into four sections. At the beginning, a description of the sinkhole phenomenon is presented. Differences in sinkholes formed in clays and in sand are then described. This research is focused on sinkholes that form in clay layers, which are called dropout sinkholes.

Subsequently an overview of the main characteristics of past sinkhole events is reported for a better understanding of soils usually involved in sinkhole formation. The events quoted regard only sinkholes formed in fine-grained soils because this was the focus of the tests.

An introduction to unsaturated soils is then presented. The chapter also describes the fundamental concepts of fracture mechanics dividing between the linear elastic and elasto-plastic theories. One of the causes of sinkhole formation is the appearance of tensile cracks in the clay layers. Therefore, a review of different tensile tests is included.

At the end, previous studies on the application of the fracture mechanics principles to clays are examined.

### 2.1 Sinkholes

The term sinkhole (also referred to as a “doline”) is used to identify a site where the ground is sinking into a void (Waltham et al., 2005; Donnelly, 2008). The term spans different processes of formation such as bedrock dissolution, rock collapse,

soil down-washing and soil collapse. Waltham et al. (2005) identified six types of sinkholes (Figure 2.1):

1. solution sinkhole: dissolution of the surface that takes place in rocks over a long period;
2. collapse sinkhole: failure of the rock roof which overlies a cave, this failure involves rocks and is rapid and catastrophic;
3. dropout sinkhole: is a collapse of the soil into a soil void which is formed over bedrock fissures, it happens in cohesive soil over a very short period of time;
4. buried sinkhole: is a sinkhole in rock, soil-filled after environmental change, it takes place in a rockhead depression in soluble rocks after a very long length of time .
5. caprock sinkhole: is a failure of insoluble rock into a cavity in soluble rock below and takes place in any rock, requires a long length of time;
6. suffusion sinkhole: down-washing of non-cohesive soil into fissures in the bedrock, it is a slow process that develop during many years. Suffusion and dropout sinkholes are usually grouped together with the name of subsidence sinkholes.

Most sinkholes require many years to arrive at an unstable condition. However, two types form rapidly and produce the most catastrophic effects: collapse sinkholes and dropout sinkholes. Due to the potential soil capacity for bridging over voids, these two types of sinkhole can have sizable dimensions. Before the sudden soil collapse, unseen cavities can increase their size until failure is reached.

Only dropout sinkholes are described in subsequent sections and they are referred with the general term “sinkholes”. This approach has been taken due to their unexpected appearance, allowing this thesis to focus on cohesive soil loading and fracture formation.

### **2.1.1 Dropout sinkhole**

Dropout sinkholes take place where an underground soluble rock, like limestone or dolomite, is covered by a layer of cohesive soil, like clay, or where a layer of cohesive

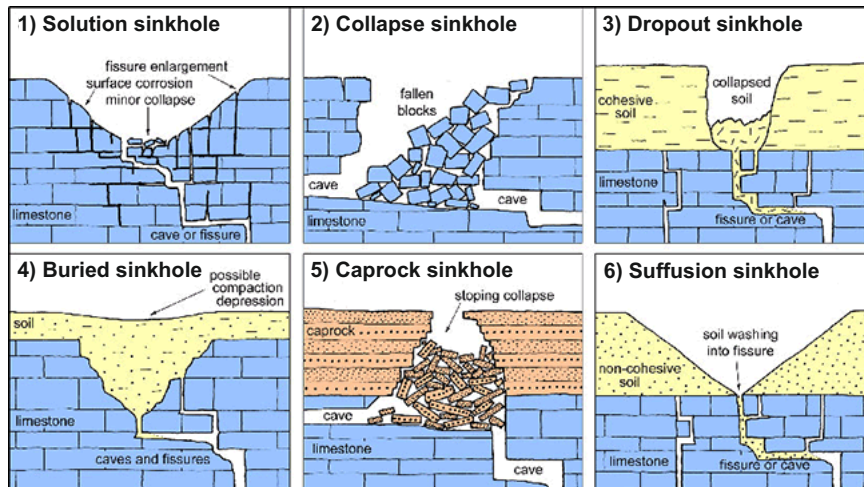


Figure 2.1: Types of sinkholes (taken from the British Geological Survey website, [www.bgs.ac.uk](http://www.bgs.ac.uk), 2011)

soil covers mine tunnels. This process is illustrated in Figure 2.2.

- Water infiltrates into the rock and dissolves the soluble parts creating cracks and fissures until a system of interconnected caves is created (Figure 2.2(b) and 2.2(c)).
- During the process, the size of the cracks and fissures increase forming a ‘bridge’ or arch in the cohesive soil (Figure 2.2(e)).
- As the process is started by water percolation, the water that infiltrates from the ground surface to the bedrock system of cavities carries some fine particles (Figure 2.2(f)).
- In this manner, the arch created over the soluble rock increases in size until it reaches the maximum loading capacity and fails in bending after the appearance of fractures in the areas of maximum tensile stress (Figure 2.2(g)).
- At that point the soil suddenly ‘drops out’ diminishing the thickness of the soil cover or creating a void at the surface (Figure 2.2(d) and 2.2(h)).

The failure can also be caused by the collapse of the bedrock into the system of cavities, but this type of failure is rare. In this type of sinkhole settlements appear

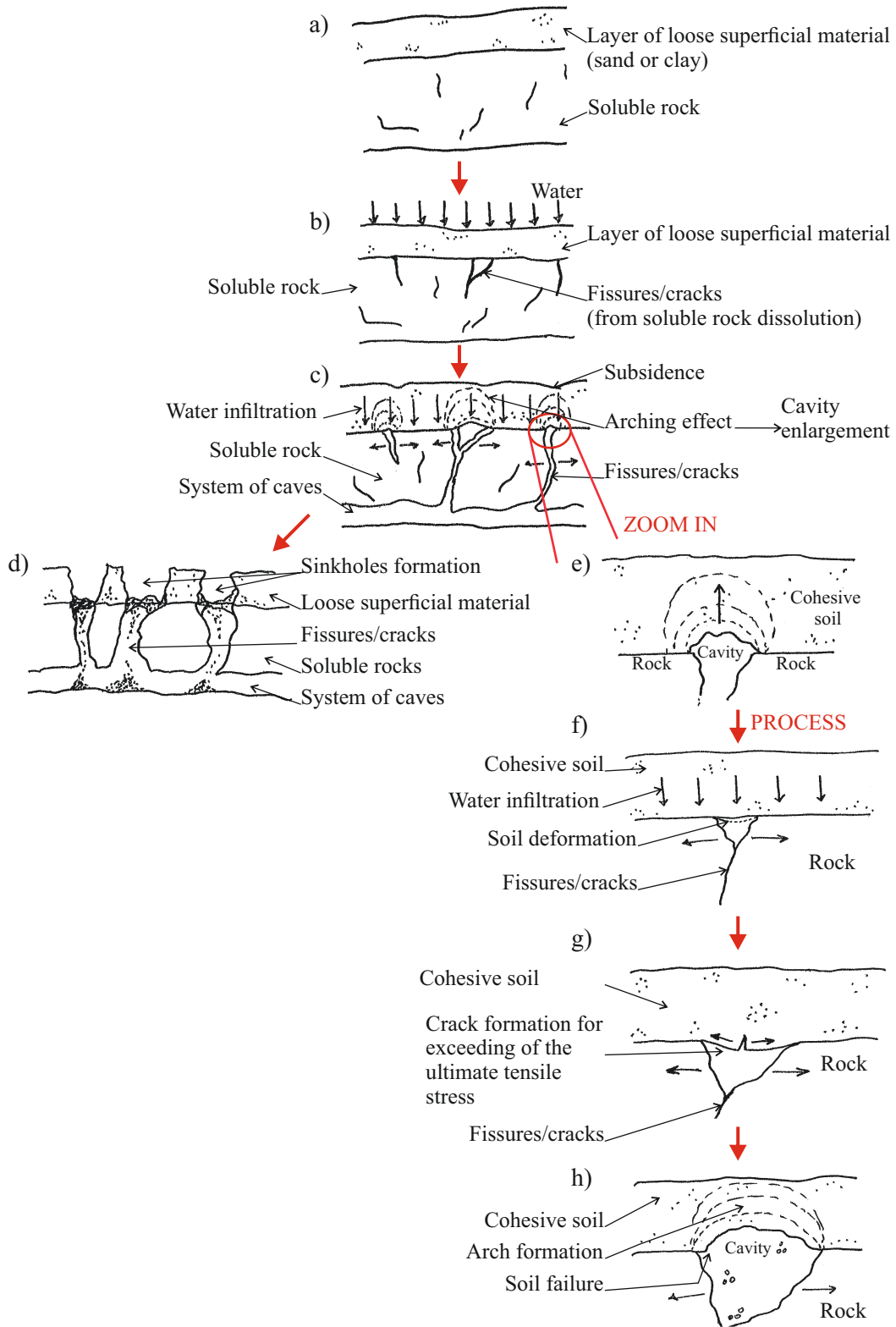


Figure 2.2: Process of formation of a dropout sinkhole

on the surface during its formation (Waltham et al., 2005).

The clayey layer over a cavity undergoes bending deformation which provokes the drop of part of the clayey layer in the cavity below. The remaining soil over the void is left in an arch configuration. Once the arch formation has reduced the layer's height to a minimum of approximately 15 m, the clayey stratum is relatively thin compared to the span. For this reason, the layer undergoes bending and tensile loads must be mobilised.

Considering the geometry as a fully-fixed ended beam, the soil starts to deform developing tensile stresses in the central section (Figure 2.3). The crack formation is hypothesised to have a key role in the sinkhole formation. Tensile cracks start to appear in the bottom edge where the ultimate tensile strength is exceeded while mixed mode cracks appear at the fixed beam extremities due to the presence of moment and shear. In a similar configuration the system deforms until collapse.

In this study, a simpler mechanical model than the fully-fixed ended beam is adopted. The clayey layer is simplified as a simply supported beam in which only tensile cracks appear. The simplification can be justified by the importance of the central section of the bending beam in which only tensile stresses are developed. Both the mechanical models produce a maximum moment and no shear in the central section, but a simply supported beam is easier to reproduce in a laboratory model than a fixed-ended beam.

### 2.1.2 Past sinkhole events

Collapses of soil overlying cavities occur around the world. Many authors (see Appendix A) have reported collapses, both natural and human-induced, in the past 50 years. However, they usually did not investigate the event from a geotechnical point of view. Instead they limited their analysis to the description of the collapse, reporting the dimensions, type of soil involved and triggering factors.

To introduce the topic of the research, a study of the geotechnical characteristics of the collapsed soils has been completed. The full database is given in Appendix A, Tables A.1-A.5, A.6-A.12, with the findings summarised below in Table 2.1 and in the bullet-points.

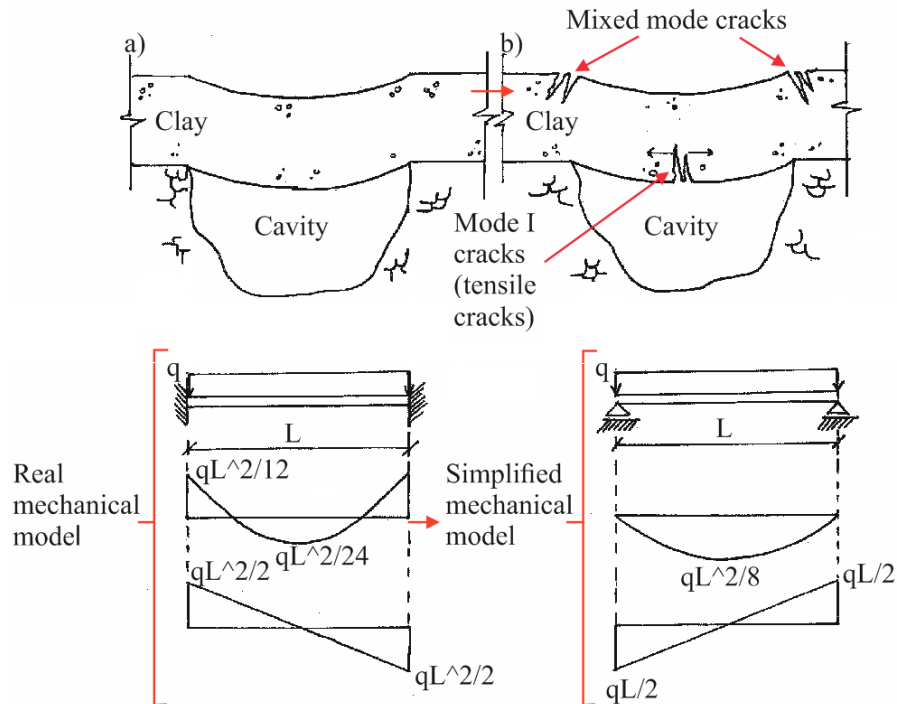


Figure 2.3: Mechanical model used to simplify the mechanism of sinkhole formation

- Sinkholes in clay were very rare. Instead, collapses usually involved mixtures of clay with sand or silt. This would indicate collapses in cohesive soils with low plasticity.
- In most of cases the triggering factor which caused sinkhole initiation was related to the movement of the ground water table. Decline of the water table caused the appearance of the sinkholes.
- Most cases of sinkholes took place where clayey strata were shallow. In the majority of the events reported clayey layers had a thickness less than or equal to 15 m. However, few cases of sinkholes happened in thick layers. Sinkholes initiated in clayey soils thickness of approximately 20 or 30 m have been reported in literature but they seem less likely to happen compared to the scenario in which the clay layer is  $< 15$  m thick. This was probably related to the fact that wider underground cavities were necessary to trigger the sinkhole mechanism or by the improved performance of thicker clay deposits.

<b>Past sinkhole characterisation</b>	
<b>Cover soil</b>	clay+sand and silt
<b>Triggering factor</b>	Lowering of the water table
<b>Sinkhole diameter (m)</b>	<10
<b>Sinkhole depth (m)</b>	<10
<b>Clayey layer height (m)</b>	<15
<b>Layer depth from the surface (m)</b>	<20
<b>Water table depth (m)</b>	1.6-30
<b>Clayey layer geotechnical parameters</b>	
<b>Plasticity index <math>PI</math> (%)</b>	28-42
<b>Composition</b>	Chert debris
<b>Moisture content <math>\omega</math> (%)</b>	16-175
<b>Liquid limit <math>LL</math> (%)</b>	26-153
<b>Unit weight <math>\gamma</math> (kN/m<sup>3</sup>)</b>	16.4-27.2
<b>Dry unit weight <math>\gamma_d</math> (kN/m<sup>3</sup>)</b>	13.9-17.4
<b>Cohesion <math>c'</math> (kPa)</b>	6-18
<b>Internal friction angle <math>\phi</math> (°)</b>	8.7-29.5

Table 2.1: Summary of the data regarding past sinkhole events

- The depth of the clayey layer to the surface was reported to be less than 20 m in the majority of the events studied. Rarely sinkholes occurred at high depths, but there were few examples of sinkholes initiated from clayey layers at depths of 120 and 235 m.
- Few studies reported the soil plasticity index and they were equal to 28 and 42 %.
- In many cases, a component of chert debris was found in the clayey mass. Few references to the mineral composition were found. They were generally montmorillonite, illite, smectite and chlorite.
- Dimensions of the sinkholes occurred varied from  $\approx 2$  m to  $\approx 100$  m both in

diameter and depth. Most of the cases had a small diameter and depth, usually not greater than 10 m. However, the literature also reported the appearance of very large and deep sinkholes. For example, the sinkhole that developed in Florida in 1981 which caused the collapse of the Winter Park measured 106 m in diameter and 30 m in depth.

- Little data on the moisture content was collected. Moisture contents varied from a minimum of 16 % in a loess and clay layer to a maximum of 175 % in a siliciclastic clay. Indications of a very high moisture content similar to the liquid limit were found.
- Few values of unit weight of the clayey layer collapsed were reported. The range varied from 16 to 27 kN/m<sup>3</sup>. In dry conditions, the unit weight varied from 14 to 17 kN/m<sup>3</sup>.
- Past sinkholes occurred in clayey layers which presented a small effective cohesion (< 20 kPa) and a small internal friction angle. The maximum cohesion was recorded in a silty/sandy loam and the maximum internal friction angle in a boulder clay.
- Many sinkholes occurred as a consequence of the water table lowering. The depth of the water table was found to be in between 1.6 and 30 m. This seemed to agree with the depth of the clayey layer found from the analysis. The collapsed clayey stratum was generally located at a depth lower than 20 m. This depth was strongly affected by the water table variation.

From the data collected it is not possible to recognise a distinctive trend of the geotechnical parameters. However, sinkholes seem to develop in thin layers of clayey soils rather than in thick layers. The soil involved in the collapses is usually a mixture of clay with some sand and silt. The soil collapses create small holes in which the diameter and the depth are generally less than 10 m. Finally, no data regarding the tensile properties of the clayey strata collapsed were reported.

## 2.2 Fundamental concepts of unsaturated soils

Soils are usually simplified as two-phase materials made of solids and voids, which can be completely saturated or completely dry. The voids inside the solids are filled with water and no air is present when the soils is completely saturated. In a completely dry condition, the voids are filled with air and no water is present. However, an inbetween condition is defined as unsaturated soils. In this state, soils are characterised by a three-phase system: solids, water and air. The properties of unsaturated soils are determined by the relative distribution between the three components.

### 2.2.1 Stress state variables

The physical behaviour of saturated soils is commonly described using the effective stress variable. It controls the volume change process and the shear strength of a saturated soil. In 1977, Fredlund and Morgenstern defined the equilibrium equations for unsaturated soils based on the concept of multiphase continuum mechanics. The stress state variable combinations that are usually used in the unsaturated soils mechanics problems are the net normal stress  $(\sigma - u_a)$  and matric suction  $(u_a - u_w)$ , where  $\sigma$  is the total normal stress,  $u_a$  the pore-air pressure and  $u_w$  the pore-water pressure. These two independent stress state variables take the form of two independent stress tensors when considering the state of stress at a point in three dimensions (Fredlund and Rahardjo, 1993):

$$\begin{bmatrix} (\sigma_x - u_a) & \tau_{yx} & \tau_{zx} \\ \tau_{xy} & (\sigma_y - u_a) & \tau_{zy} \\ \tau_{xz} & \tau_{yz} & (\sigma_z - u_a) \end{bmatrix} \quad (2.1)$$

$$\begin{bmatrix} (u_a - u_w) & 0 & 0 \\ 0 & (u_a - u_w) & 0 \\ 0 & 0 & (u_a - u_w) \end{bmatrix} \quad (2.2)$$

in which  $\sigma_x, \sigma_y, \sigma_z$  are the net normal stress in the  $x, y, z$  directions and  $\tau$  is the shear stress.

Attempts were made to define a single effective stress variable for unsaturated soils. Bishop (1959) proposed the equation:

$$\sigma' = (\sigma - u_a) + \chi(u_a - u_\omega) \quad (2.3)$$

in which  $\chi$  is the soil parameter related to the degree of saturation and varies between 0 and 1.

This equation is not considered as a fundamental description for an unsaturated soil. It contains a soil property and should be referred to as a constitutive equation (Fredlund et al., 2012). In addition,  $\chi$  is not of easy determination.

### 2.2.2 Soil-water characteristic curve

The relationship between the amount of water in the soil and the matric suction is expressed by the soil-water characteristic curve, SWCC (or soil water retention curve, SWRC). This relationship is normally plotted as the variation of gravimetric moisture content  $\omega$ , volumetric moisture content  $\theta$ , or degree of saturation  $S$ , with respect of matric suction. The importance of the SWCC is related to the relationship between the moisture content with one of the controlling stress variables, the matric suction.

A typical SWCC is shown in Figure 2.4. Due to the ability to estimate the unsaturated soil property from the SWCC, it becomes the most valuable piece of information for geotechnical engineering practice (Fredlund et al., 2012).

Three distinct zones of desaturation can be identified along the SWCC: boundary effect, transition and residual zones (Fredlund and Rahardjo, 1993). Two transition points can be identified on the SWCC: the air-entry value (AEV) and the residual value condition. The AEV is defined as the matric suction value at which the air enters the voids of the soil, determining the passage of the soil from a saturated to an unsaturated state. The residual value, instead, is the residual volumetric moisture content from which any increase of matric suction does not produce a change in moisture content.

Different methods can be used to determine the SWCC. The most widely used are the filter paper method, pressure plate and tensiometers. The filter paper method

is an indirect method that can be used to determine both the total and the matric suction (Charles and Menzies, 2007). A soil sample and a filter paper placed in a container are allowed to reach an equilibrium moisture content (Figure 2.5.b)). The equilibrium moisture content of the filter paper is corresponding to the suction of the soil specimen (Figure 2.5.c)). A filter paper calibration curve is used to obtain the suction value (Perera et al., 2004). Figure 2.5.a) shows the calibration curve for the two filter papers that are commonly adopted: Whatman No. 42 and Schleicher and Schuell No. 589.

In the pressure plate method, the soil specimen is placed inside a pressure chamber and a specified air pressure is applied to pressurise the chamber (Figure 2.6). The applied air pressure can be considered equal to the applied suction on the base of the axis-translation technique. The soil inside the pressure chamber equilibrates the applied suction by releasing or absorbing water through a ceramic plate (permeable media). Once equilibrium is reached, the moisture content of the specimen is determined. Performing the test at several applied suction values, the SWCC can be determined. The maximum applied suction is equal to 1500 kPa, which correspond to the maximum air-entry value of the ceramic plate (Perera et al., 2004).

Tensiometers measure the absolute negative pore water pressure. The water is ex-

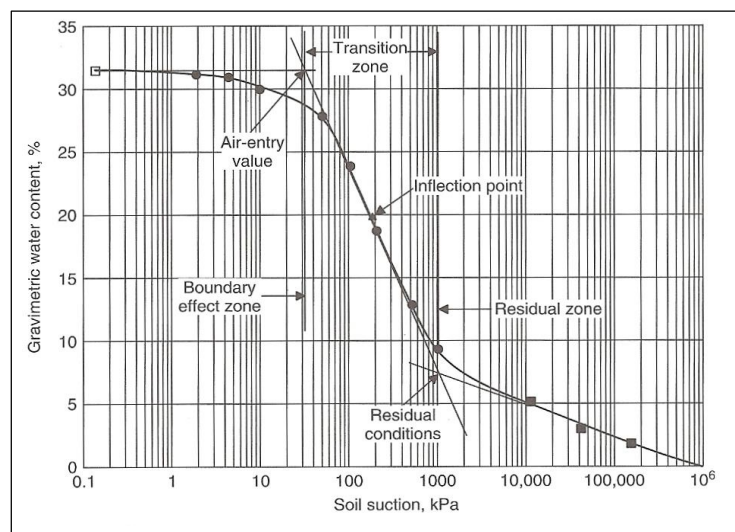


Figure 2.4: Typical soil water characteristic curve (SWCC) taken from Fredlund et al. (2012)

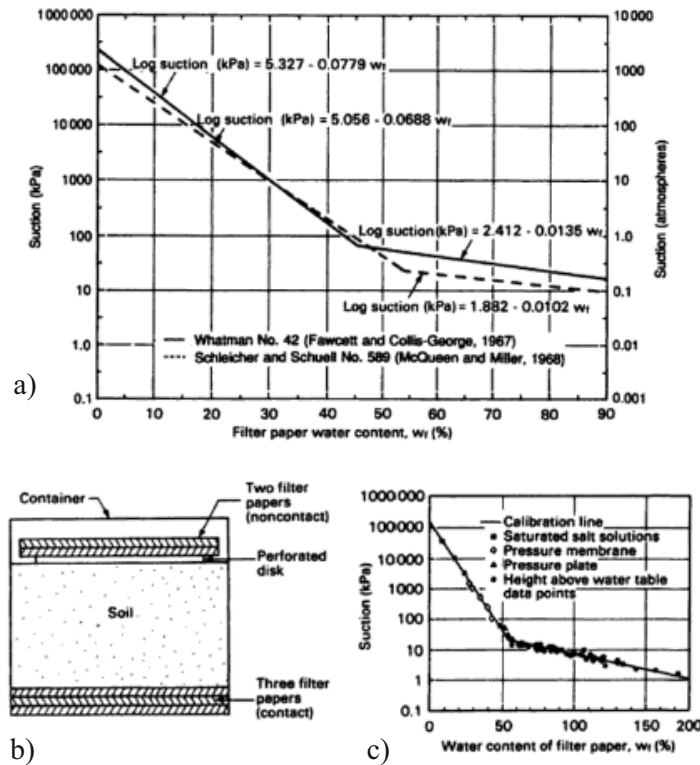


Figure 2.5: Filter paper a) calibration curve for the two filter papers most used, b) setup, c) relationship between water content of the filter paper and suction taken from Fredlund and Rahardjo (1993)

tracted from a reservoir in the tensiometer through a porous ceramic filter and it is released in the soil. This happens until the stress holding the water inside the tensiometer is equal to the stress holding the water in the soil, which is the soil suction (Figure 2.7). Once equilibrium is reached no further flow of water occurs between the soil and the tensiometer. The suction is seen as a tensile stress in the reservoir water and can be measured with any stress measuring instrument (Charles and Menzies, 2007).

## 2.3 Fundamental concepts of fracture mechanics

The phenomenon of sinkhole formation is related to the development of tensile cracks. It has been hypothesised in Section 2.1.1 that soil layers that overlay underground cavities undergo tensile loading and therefore can fail from crack formation.



Figure 2.6: Pressure plate (Soilmoisture, 2008)

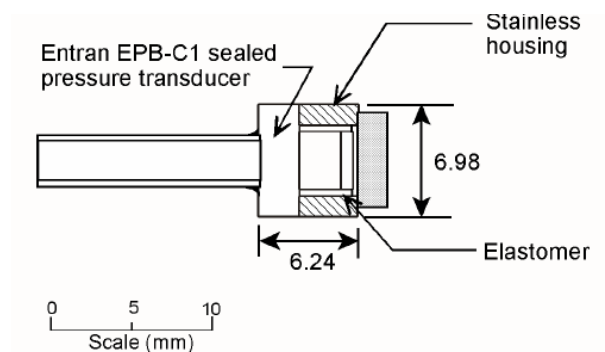


Figure 2.7: Tensiometer developed by Take (2003) for his investigation on the effects of climate changes on embankments

A crack is a discontinuity that can be seen as an element of weakness through the soil which facilitates failure. For this reason, an important aspect often overlooked in sinkhole formation is focused on the understanding of crack initiation and growth. The mechanism of creating new surfaces (cracks) in a body is called fracture and is facilitated by the presence of defects inside the element mass (Janssen et al., 2002). The fracture process was initially studied in metals. From an atomic point of view, a metal cracks when the bonds between the atoms are broken either by cleavage of the bonds or replacement of the metal-to-metal atom bonds by alternative ion-to-metal bonds and a rearrangement of the atomic metal structure. The bonds between atoms

are supplied by cohesive forces which keep the atoms together (Anderson, 2005). Atoms are at equilibrium between attraction and repulsion when the potential energy is at the minimum. To separate the atoms completely a tensile force has to exceed the cohesive force and increase the distance between the atoms. However, the fracture usually takes place at a lower strength compared to that corresponding to the theoretical value that is keeping the atoms together, as Griffith (1920). The difference between these two forces is related to the presence of flaws inside the element. Flaws lower the global cohesive force increasing the stress locally and facilitating the crack formation. Thus, the tensile force can exceed the cohesive force and cause the atoms to separate (Figure 2.8).

The system of forces acting on the element determines the type of crack that will appear. The three main types of cracks and loading systems are:

- mode I, in which the soil fails by tensile opening (Figure 2.9(a)).
- mode II, where the crack opens for sliding due to shearing forces (Figure 2.9(b)).
- mode III, which is a non-planar fracture as the element is subjected to out-of-plane forces, also called tearing (Figure 2.9(c)).

The simplest material behaviour to describe crack formation is a linear elastic material response, which is named Linear Elastic Fracture Mechanics (LEFM). However, it is possible to have different types of material behaviour from the linear-elastic behaviour: elasto-plastic fracture under quasistatic conditions, dynamic and viscoelastic/viscoplastic behaviours. In the last two the response is time dependent. Those responses are grouped under the name nonlinear fracture mechanics. The adoption of one or another theory of fracture mechanics depends on the material response.

### 2.3.1 Linear elastic fracture mechanics

In linear elastic materials, two different approaches to study the fracture behaviour have been used in the past: the energy and the stress-intensity approach, which are

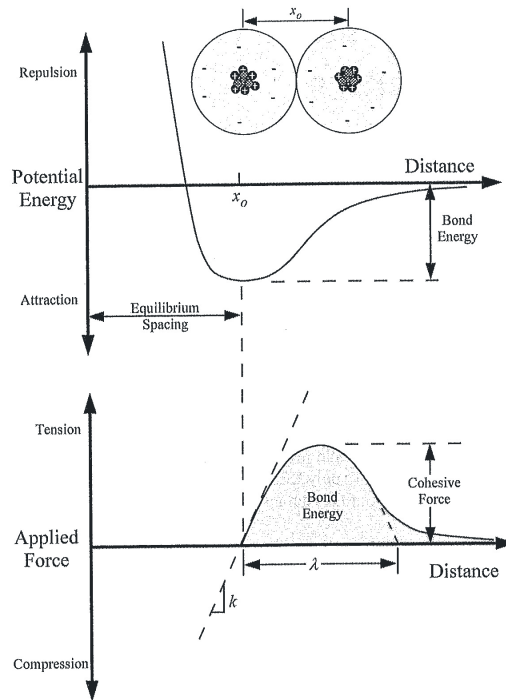


Figure 2.8: Potential energy and applied force between particles at the atomic level (taken from Anderson (2005)).  $k$  is the bond stiffness,  $\lambda$  is the amplitude of the sine wave with which the cohesive force is simplified

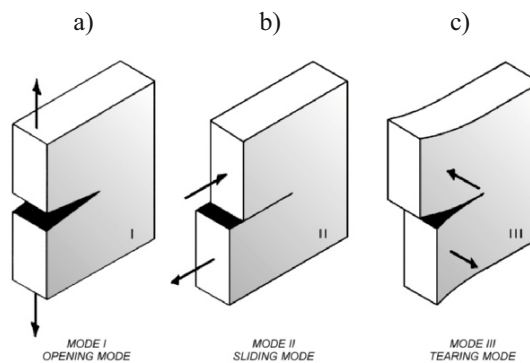


Figure 2.9: Main types of cracks related to their load system (taken from Janssen et al. (2002))

in a certain way equivalent.

The energy criterion was proposed by Griffith (1920) and developed by Irwin (1956). If the potential energy available to extend the crack is overcoming the energy required by the material to create new surfaces (surface energy), then fracture takes

place. In a linear elastic material, the energy release rate  $G$  is defined as the rate of variation in the potential energy with the crack area. When the fracture takes place  $G = G_c$ , where  $G_c$  represents the critical value of energy release rate and is a measure of the material's resistance to crack formation. Supposing to have a crack of length  $2a$  in an infinite plate (width of the plate  $\gg 2a$ , Figure 2.10), at the moment of fracture the energy equation determined by Irwin (1956) is:

$$G = \frac{\pi\sigma^2a}{E} = \frac{\pi\sigma_f^2a_c}{E} = G_c \quad (2.4)$$

in which  $E$  is the Young's modulus and  $\sigma$  is the uniform tensile stress applied at infinity. The subscript  $f$  denotes the values at the moment of failure and the subscript  $c$  indicates the critical value.

The second approach is called the stress-intensity approach (Irwin, 1956). The stress distribution at the crack tip can be characterised by a constant  $K_I$ . In a linear elastic material this constant is called the stress-intensity factor and gives the magnitude of the elastic field. When the material fails, the fracture occurs at a critical stress intensity  $K_{IC}$ . This value can be seen as a material property characterizing the crack resistance, and is called the plane strain fracture toughness. Using the same example as before the stress intensity factor is given by:

$$K_I = \sigma\sqrt{\pi a} \quad (2.5)$$

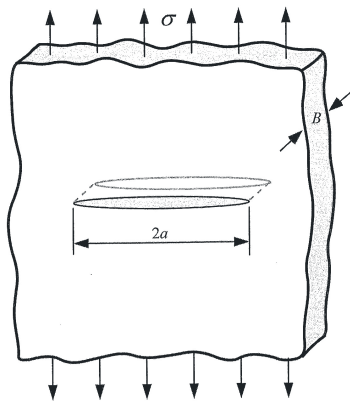


Figure 2.10: Infinite plate with a crack of length  $2a$  under tensile stress (taken from Anderson (2005)).  $B$  is the plate width

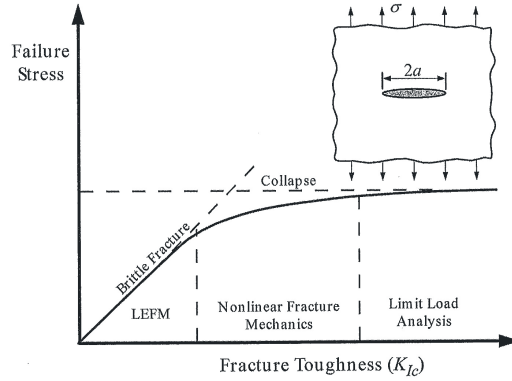


Figure 2.11: Fracture mechanics theories (taken from Anderson (2005))

and at failure

$$K_I = K_{Ic} = \sigma \sqrt{\pi a_c} \quad (2.6)$$

It is also possible to find a relationship between  $K_{Ic}$  and  $G_c$ . Combining Equations 2.4 and 2.5, the relationship between the two parameters can be expressed as:

$$G_c = \frac{K_{Ic}^2}{E} \quad (2.7)$$

Considering a cracked plate (Figure 2.11) high values of fracture toughness represent a material in which failure is governed by the flaw properties and LEFM results inappropriate. Low values of fracture toughness characterise materials that can be easily broken because little energy is required to produce the crack. These materials break in a brittle manner and critical stress varies linearly with  $K_{Ic}$ . The transition between linear elastic conditions and ductile overload is characterised by intermediate values of fracture toughness. The nonlinear fracture mechanics is placed between LEFM and failure.

For linear elastic materials, some fundamental assumptions are applied to the crack problem: at first, the fracture toughness is assumed independent from the size and geometry of the cracked element. For this reason a model fracture toughness can be used to study a prototype body.

The linear elastic analysis also implies a stress at the crack tip which should be infinite. However, this hypothesis is unrealistic as the stress next to the crack tip should be finite. Structural materials deform plastically above the yield stress, so a

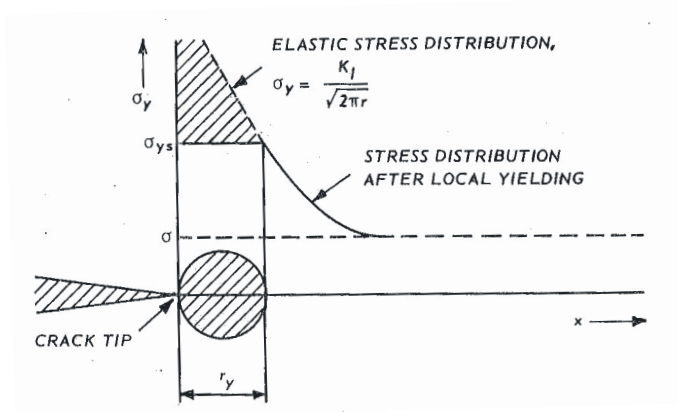


Figure 2.12: Sketch of the crack tip plasticity zone (taken from Ewalds and Wanhill (1984))

plastic zone exists in the vicinity of the crack tip in which the material is yielding. This zone is limited and is identified by the length  $r_y$  (Figure 2.12).

### 2.3.2 Elasto-plastic fracture mechanics

When plasticity is confined to a small zone around the crack tip, the linear elastic analysis is sufficient (Anderson, 2005). But, if the crack tip plastic zone of the material is too large, nonlinear fracture mechanics should be applied (Figure 2.13). The inadequacy of LEFM can also be detected from the stress-strain curve (Figure 2.14). At the beginning the curve is linear, but then deviates with the proceeding plastic deformation, therefore requiring a nonlinear approach.

When elasto-plastic fracture mechanics is adopted, two parameters are used in the description of crack initiation:

- the crack tip opening displacement, CTOD, and
- the J contour integral (defined also in case of LEFM).

During plastic deformation an initially sharp crack blunts at the tip, as Figure 2.15 shows. Wells (1961) noticed that the tip blunting increased with the increase of the fracture toughness. So, he proposed the use of the crack opening as a measure of fracture toughness. Measuring the distance between the two crack faces at the level

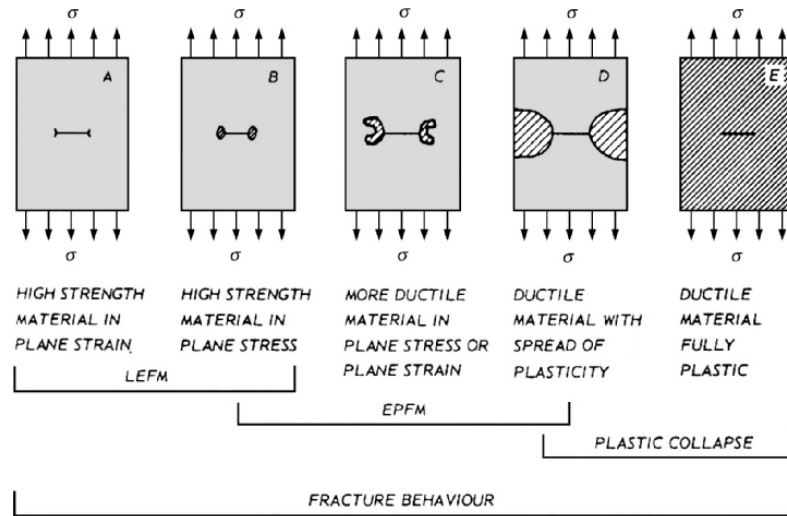


Figure 2.13: Different theories of fracture mechanics and their applicability (taken from Janssen et al. (2002))

of the tip ( $\delta$ ), the CTOD is estimated using the following equation:

$$CTOD = \delta = \frac{4}{\pi} \frac{K_I^2}{\sigma_{YS} E} \tag{2.8}$$

where  $K_I$  is the stress intensity factor and  $\sigma_{YS}$  is the yield stress. However, it is common practice to study edge-cracked beams in 3-point bending tests. Thus, the CTOD is usually calculated using a triangular construction (Figure 2.16). This leads to the equation:

$$\delta = \frac{r(W - a)V}{r(W - a) + a} \tag{2.9}$$

in which  $W$  is the height of the beam,  $a$  the length of the initial crack,  $V$  the crack

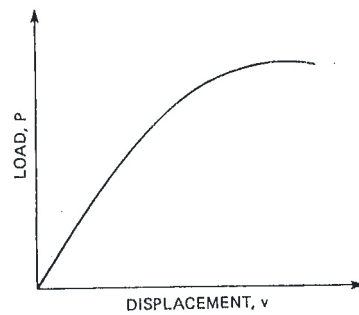


Figure 2.14: Stress-strain curve for a nonlinear response (taken from Ewalds and Wanhill (1984))

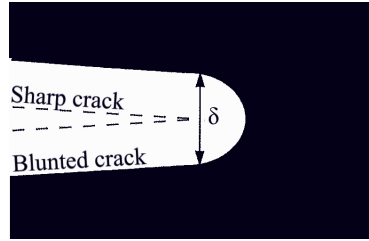


Figure 2.15: Crack tip opening displacement CTOD or  $\delta$  (modified from Anderson (2005))

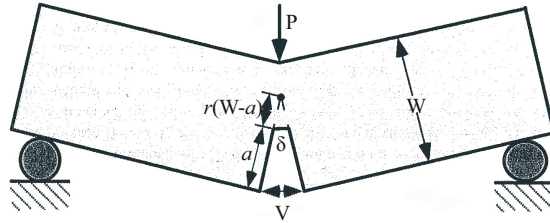


Figure 2.16: Parameters used for the calculation of the CTOD (modified from Anderson (2005))

mouth displacement (the length of the opening at the end of the initial crack).  $r$  is a rotational factor related to the two beam's halves that rotate around the point of load application and is a dimensionless constant between 0 and 1 (Anderson, 2005). This constant covers a wide range of values because many techniques can be used for its determination, as the double clip gauge method or the crack infiltration with plastic or silicone rubber. For the CTOD determination, Janssen et al. (2002) reports that  $r$  is equal to 0.4 for metal beam specimens (SENB).

The second parameter is the J contour integral which is defined by Rice (1968) as the energy release rate in a nonlinear body which contains a crack. The J-integral represents the linear-elastic energy release rate  $G$  in nonlinear conditions and can be written as:

$$J = \frac{d}{da}(P_x - U_a) \quad (2.10)$$

where  $P_x$  is the external work done,  $U_a$  is the change in the elastic energy due to the introduction of the crack in the body and  $a$  is the crack length. As  $J$  is a parameter to identify the elasto-plastic energy release rate, it is possible to expect the presence of a critical value  $J_c$ . This critical value is used to highlight crack initiation and is a characteristic material property.

Various methods can be used in the laboratory to measure the magnitude of the  $J$  value. The standard method has been developed by Begley and Landes (1972) who studied a series of cracked specimens under tensile loading. The samples studied were all of the same size, geometry and material but the initial notch length was varied. Once tested, they calculated the energy  $U$  absorbed by the specimen as the area under a load-displacement curve (Figure 2.17(a)). The  $J$  integral is expressed using the equation for a single-edge cracked specimen:

$$J = -\frac{1}{B} \left( \frac{\partial U}{\partial a} \right)_{\Delta} \quad (2.11)$$

where  $B$  is the specimen width,  $\Delta$  the applied vertical displacement and  $a$  the crack length.

In this manner,  $J$  can be calculated as the slope of the tangent to the curves  $U$ - $a$  (Figure 2.17(b)). So, Equation 2.11 is leading to the series of curves where  $J$  is related to the displacement at various crack lengths (Figure 2.17(c)). This approach for the calculation of the  $J$  integral is time consuming as it requires the preparation of many samples with various initial crack lengths.

The method that is most used to calculate the  $J$  integral is standardised by the ASTM (ASTM:E1820-15, 2015) for metallic materials. For various specimen configurations the integral can be calculated as:

$$J = \frac{\eta U_c}{Bb} \quad (2.12)$$

where  $U_c$  is the strain energy accumulated by the sample when the crack is present,  $B$  is the width of the specimen,  $b = W - a$  is the measurement of the resistant ligament (length between the physical crack front and the edge of the beam) and  $\eta$  is a dimensionless constant related to the load-displacement graph. The  $J$  integral is defined as the energy absorbed over the cross-sectional area times a dimensionless constant. In the case of a deeply cracked plate in pure bending,  $\eta = 1.9$  (value adopted for metals in the case of plastic area calculated using the load-displacement graph), as reported in ASTM:E1820-15 (2015). Equation 2.12 can also be divided into elastic (el subscript) and plastic (pl subscript) components:

$$J = J_{el} + J_{pl} = \frac{\eta_{el} U_{c(el)}}{Bb} + \frac{\eta_{pl} U_{pl}}{Bb} = \frac{K_I^2}{E'} + \frac{\eta_{pl} U_{pl}}{Bb} = G + J_{pl} \quad (2.13)$$

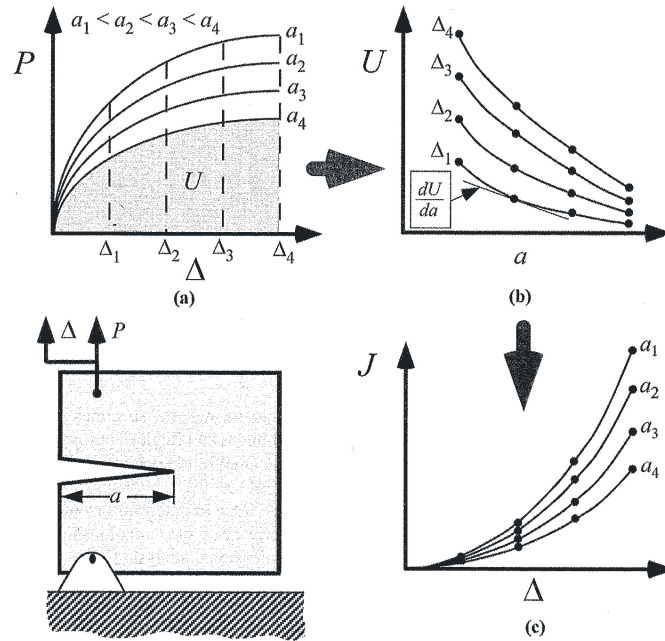


Figure 2.17: Calculation process of the  $J$  integral used by Landes and Begley (taken from Anderson (2005)).  $U$  is the energy absorbed by the sample during the test,  $P$  the load applied to the specimen,  $\Delta$  is the displacement,  $a$  the crack length

in which  $E' = E$  for plane stress and  $E' = \frac{E}{1-\nu^2}$  for plane strain.

Once the  $J$ -integral is calculated throughout the test, the results can be plotted in relation to the crack length. The curve determined is called  $J$ - $R$  curve. Using a construction drawing, the plane-strain fracture toughness can be calculated from the  $J$ - $R$  curve (Figure 2.18).

## 2.4 Tensile tests on soils

During the formation of some type of sinkhole, clay layers deform over cavities generating Mode I cracks which propagate from the bottom edge of the layer. Although, tensile mode is not the only mode of crack formation and consequently soil collapse, only the past literature focusing on Mode I cracks is presented. Tensile cracks represent the first step of the cracking process in sinkhole formation.

A wide range of tests can be used to assess the behaviour of soils under tension. However, all tests were originally designed and regulated for metallic specimens.

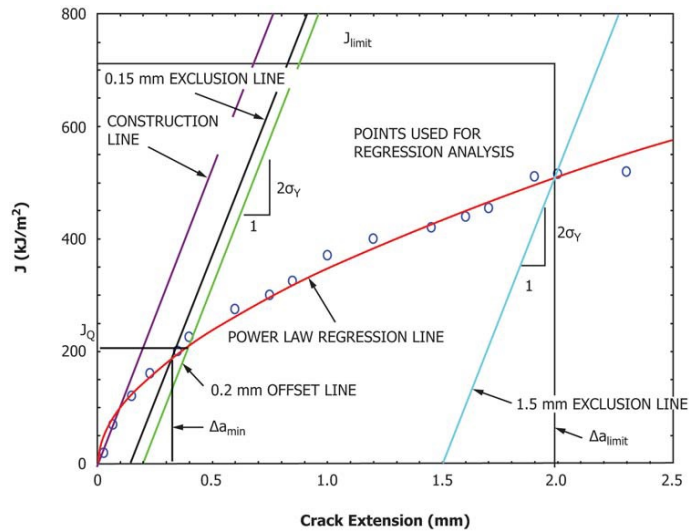


Figure 2.18: Determination of  $J_{Ic}$  showed in ASTM:E1820-15 (2015) for metals

Therefore, a precise standard for tensile testing in soils does not exist.

The methods frequently used to test soils in tensile conditions can be divided in two main groups: direct and indirect tests. The first category is represented by the direct tensile test which is usually preferred to the indirect methods. In case of soils the direct tensile test is usually preferred for its consistency of results (Divya et al., 2014).

### 2.4.1 Direct tensile test

The principle of the direct tensile test is to pull apart a sample by applying a tensile force on one side of the specimen having the opposite side fixed. In this manner, the sample is subjected to a tensile force along its entire length. In the direct tensile test, the tensile stress and strength can be directly obtained during the test.

Different setups for the direct tensile test have been adopted in the past. One of the first direct tensile tests on soils reported in literature was performed by Tschebotarioff et al. (1953) (data listed in Tables 2.2 and 2.3). They used very large samples shaped like a hourglass prepared using various clay types. The soil was compacted into a mould which had one end fixed and one end standing on rollers which allowed the mould to move (Figure 2.19). Then the sample was loaded in the horizontal direction (gravity perpendicular to the loading direction). More recently a very

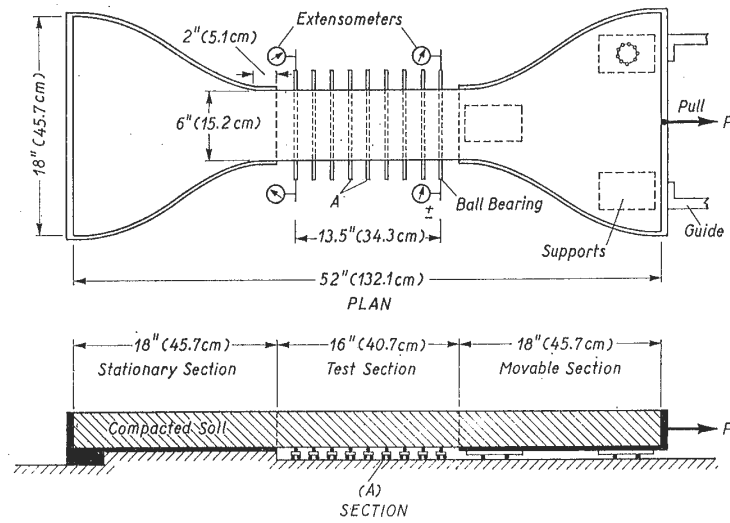


Figure 2.19: Direct tensile test setup adopted by Tschebotarioff et al. (1953)

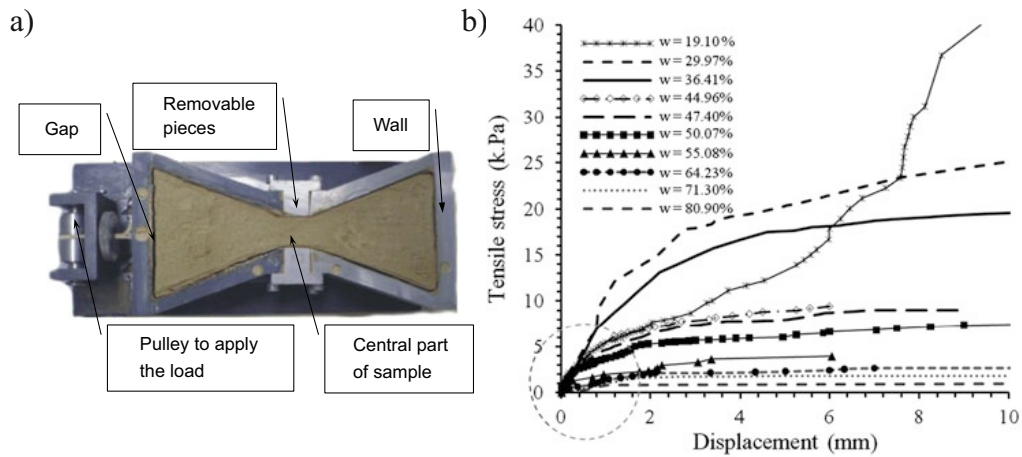


Figure 2.20: Direct tensile test setup and example of the loading curve of Trabelsi et al. (2012) tests

similar system (Figure 2.20), but smaller in dimension, was used by Lakshmikantha et al. (2008) and Trabelsi et al. (2012) (data listed in Tables 2.2 and 2.3). Divya et al. (2014) and Stirling et al. (2015) modified the direct shear equipment to test fine grained soils in tension (Figure 2.21, data listed in Tables 2.2 and 2.3). The principle adopted in all the cases was the same of that used in Tschebotarioff et al. (1953) tests: half of the sample mould was fixed to the system while the other half was allowed to move horizontally.

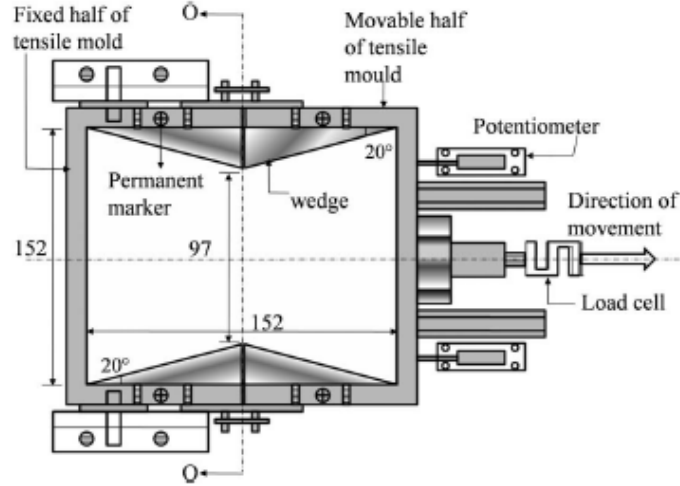


Figure 2.21: Direct tensile test setup used by Divya et al. (2014)

Farrell et al. (1967) and Wang et al. (2007b) conducted tensile tests loading a vertical cylindrical soil column until failure was reached (data listed in Tables 2.2 and 2.3). The soil was fixed to the loading frame using two clamps while a loading pole applied the force (Wang et al., 2007b). Deformation and load were measured using two sensors (Figure 2.22). In the Farrell et al. (1967) experiments, the clay was glued to the loading plate using araldite epoxy resin on the end face of the sample.

The tensile strength for the cylindrical specimens was calculated by dividing the force applied by the cross sectional area. The weights of the upper part of the loading apparatus were subtracted from the applied tensile forces as this was acting in the opposite direction of the applied force.

$$\sigma_t = \frac{P_{max} - w_{frame}}{A} \quad (2.14)$$

where  $P_{max}$  is the maximum load measured during the experiment,  $w_{frame}$  is the weight of the upper part of the loading frame and  $A$  is the cross sectional area of the cylindrical specimen.

Zeh and Witt (2007) used a hollow cylinder to test the clay in tension. The inner hole was filled with a filter textile and epoxy resin was used to glue a modified dowel

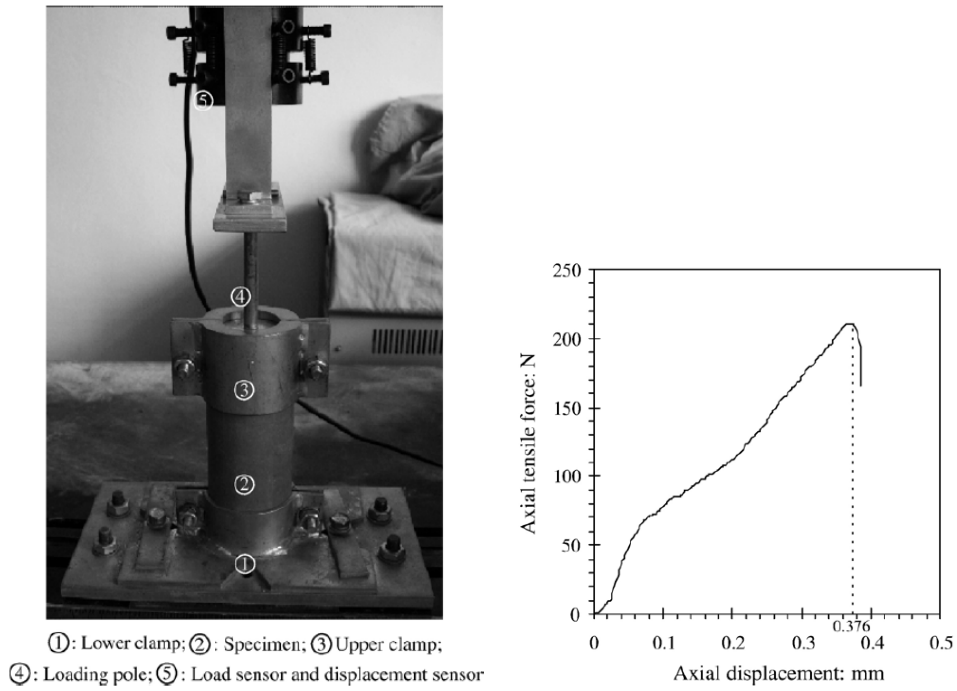


Figure 2.22: Direct tensile test setup and example of the loading curve of Wang et al. (2007b) tests

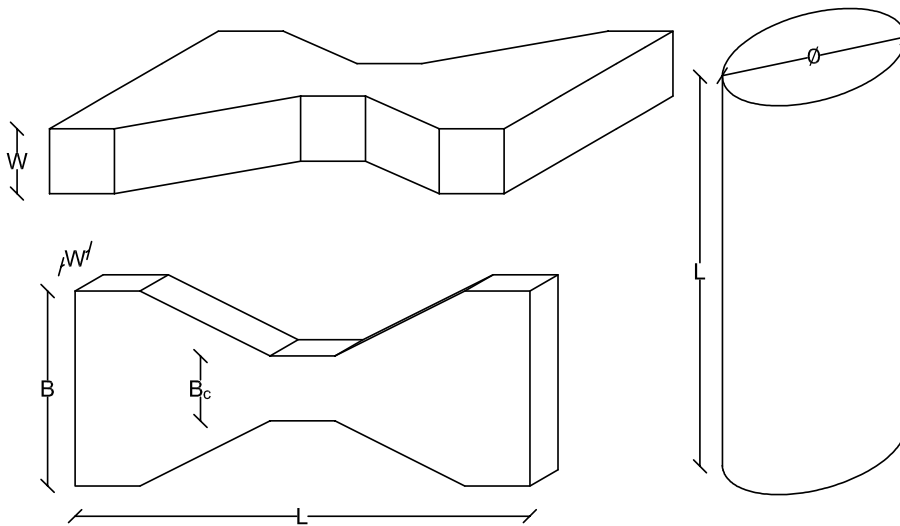


Figure 2.23: Symbols used in Table 2.2

Author	Hourglass shape				Cylindrical shape	
	$L$ (mm)	$W$ (mm)	$B$ (mm)	$B_c$ (mm)	$\varnothing$ (mm)	$L$ (mm)
Tschebotarioff et al. (1953)	457	1321	-	152	-	-
Farrell et al. (1967)	-	-	-	-	38	76
Wang et al. (2007b)	-	-	-	-	62	150
Zeh and Witt (2007)	-	-	-	-	24	90
Lakshmikantha et al. (2008)	-	-	30	24	-	-
Trabelsi et al. (2012)	223	-	-	-	-	-
Divya et al. (2014)	152	-	152	97	-	-
Tang et al. (2015)	80	40	10	20	-	-
Stirling et al. (2015)	100	-	54	38	-	-

Table 2.2: Dimensions of the samples tested in direct tensile tests found in the literature. The geometry symbols are shown in Figure 2.23

to both the sample ends. Two hooks were then drilled into the dowels allowing the application of tensile forces (Figure 2.24, data listed in Tables 2.2 and 2.3). More

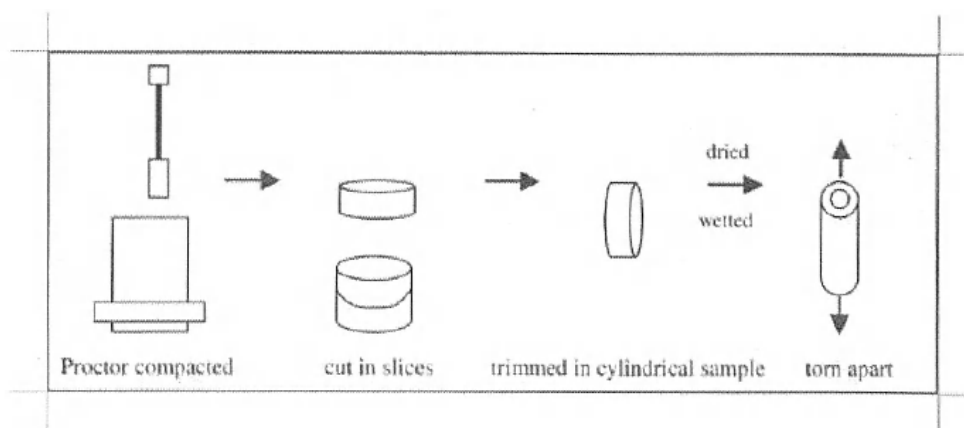


Figure 2.24: Direct tensile test setup adopted by Zeh and Witt (2007)

recently a variation in the shape of the sample was introduced by Tang et al. (2015),

<b>Author</b>	<b>Material</b>	<i>LL</i> (%)	<i>PL</i> (%)	<i>PI</i> (%)	$\Delta\sigma_t$ (kPa)
Tschebotarioff et al. (1953)	Natural clay	30	23	7	7.35 ( $\omega = 19.8\%$ ),
	Montmorillonite	540	53	487	20.64 ( $\omega = 101\%$ ),
	Illite	60	26	34	39.23 ( $\omega = 31.5\%$ ),
	Kaolinite	70	32	38	8.58 ( $\omega = 37.6\%$ )
Farrell et al. (1967)	Red-Brown loam	-	-	-	9.81 – 166.71 ( $\omega = 1.5 – 13.5\%$ )
Wang et al. (2007b)	Clay with gravels	29.1	20.2	8.9	32 – 84 ( $\omega =$ 16.4 – 19.4 %, $\rho =$ 1600 – 1760 kg/m <sup>3</sup> )
Zeh and Witt (2007)	Plessa clay	49.7	21.3	28.4	0-1000 kPa ( $\omega = 0 – 35\%$ )
Lakshmikantha et al. (2008)	Barcelona silty clay	32	16	16	0.38 – 3.38 ( $\omega = 2.5 – 30\%$ , $\gamma =$ 16 – 19 kN/m <sup>3</sup> )
Trabelsi et al. (2012)	Natural deposit	48	16	32	0.79 – 61.43 ( $\omega = 19.1 – 80.9\%$ )
Divya et al. (2014)	Natural soil (soil A)	36	25	11	-
	+15 % bentonite (soil B)	52	30	22	-
Tang et al. (2015)	Clay	37	20	17	40 – 80 ( $\omega = 4 – 27\%$ , $\rho =$ 1500 – 1700 kg/m <sup>3</sup> )
Stirling et al. (2015)	Kaolin-bentonite-sand	34	16	18	15-70 ( $\omega = 5 – 23\%$ )
	Glacial till	45	24	21	0-550 ( $\omega = 0 – 23\%$ )
	Silty sand	23	11	12	-

Table 2.3: Physical properties of the clays tested in direct tensile tests used in literature.  $\Delta\sigma_t$  is the tensile strength range of values in relation to the moisture content at which the samples were tested

who tested a clayey soil collected from the Nanjing area of China. A loading frame pulled apart an hourglass-shaped sample contained in a mould formed by two parts. The bottom part of the mould was then clamped to the rig while the top part was displaced upwards. Due to the shape adopted, a crack formed in the central section where the area was smaller compared to the ends (Figure 2.25). The calculation of the tensile strength was identical to that used by Wang et al. (2007b) shown in Equation 2.14. In this case,  $A$  in the equation refers to the cross-sectional area of the hourglass specimen.

The general behaviour was represented by a load-displacement curve with a linear relationship until failure. An exception to this behaviour was represented by the curves found by Trabelsi et al. (2012) tests. The natural deposit behaved in a nonlinear manner for every moisture content tested.

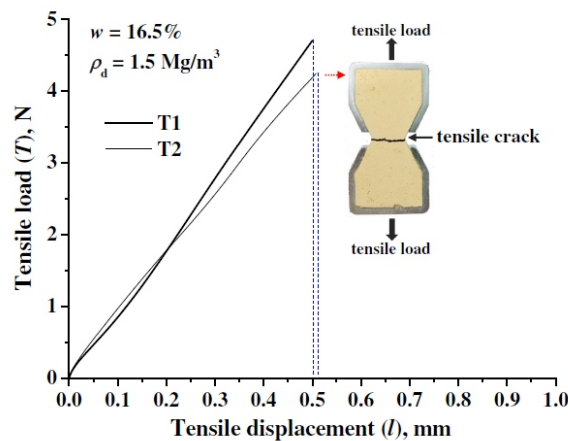


Figure 2.25: Loading curve obtained for the direct tensile tests of Tang et al. (2015)

### 2.4.2 Indirect tensile tests

Indirect methods are straightforward to perform on soils and consist of a wide range of different tests: bending beam test, split test on cylindrical sample, prismatic or cubic samples, unconfined penetration and double punch tests.

In this category, the tensile strength is calculated in an indirect manner using a series of correlations between the measured parameters. The importance of choosing the right test is given by the fact that indirect tests usually provide higher values

of tensile strength compared to those calculated with the direct tests. In particular beam tests give the highest values due to a statistical reason: a smaller volume is subjected to tension and consequently fewer flaws or elements that promote the initiation of the crack undergo tensile stress (similar to the findings of Weibull (1951) for ceramics).

The most frequent indirect tensile method is the bending test. Square or rectangular cross sectional beams are put into bending applying one or two point loads along the beam length (3-point or 4-point bending). Moreover, the beam adopted can be plain or have an initial notch in the centre.

The setup found in the literature was similar in all cases: a beam was simply supported by two rollers close to the beam ends and was loaded in the middle section or every one third of the length (Figure 2.26). Data regarding the soil properties and the beam dimensions adopted for bending tests are reported in Table 2.4 and Table 2.5. Standards for the dimensions of the beams are usually derived from metals testing (ASTM:E1820-15, 2015). For tensile tests, the span  $S_p$  is equal to four times the height  $W$ . In previous literature the standard practice for soils bending was to use beams with a span  $S_p$  4-5 times the height  $W$ . In addition, the initial crack length  $a$  was usually adopted as half or one third of the sample height.

Differently from the tensile tests in which most of the clays studied showed a linear-elastic behaviour, the bending tests reviewed presented a nonlinear behaviour in wet samples and a more linear-elastic response in dry beams.

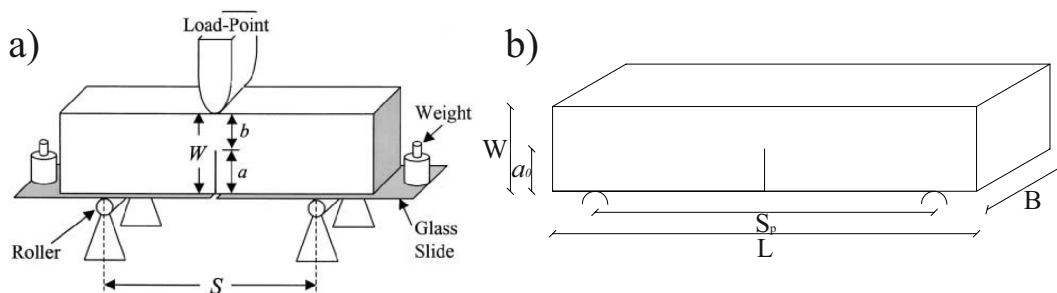


Figure 2.26: 3-point bending configuration a) adopted by Hallett and Newson (2001) and b) the symbols used to describe the geometry of the specimen

Author	Beam Dimensions					Ratios	
	$L$ (mm)	$B$ (mm)	$W$ (mm)	$S_p$ (mm)	$a_0$ (mm)	$S_p/W$	$a_0/W$
Farrell et al. (1967)	76	25	25	60	0	2.4	0
Ajaz and Parry (1975)	254	50.8	50.8	228.6	0	4.6	0
Indraratna and Lasek (1996)	500	100	100	-	0	-	0
Nichols and Grismer (1997)	-	15	30	-	15	-	1/2
Hallett and Newson (2001)	90	20	20	-	10	-	1/2
Hallett and Newson (2005)	140	25	25	-	12.5	-	1/2
Wang et al. (2007a)	-	23	46	185	21~25.	4.0	~1/2
Thusyanthan et al. (2007)	320	80	80	240	0	3	0
Viswanadham et al. (2010)	250	50	50	200	0	4	0
Amarasiri et al. (2011)	140	30	30	100	10	3.3	1/3
Plé et al. (2012)	400	100	100	300	0	3	0

Table 2.4: Dimensions of the samples tested in bending tests used in literature

<b>Author</b>	<b>Material</b>	<i>LL</i> (%)	<i>PL</i> (%)	<i>PI</i> (%)
Farrell et al. (1967)	Red-Brown Earth, Parafield loam	-	-	-
Ajaz and Parry (1975)	Cambridge Gault clay	73	34	39
	Balderhead clay	34	20	14
Indraratna and Lasek (1996)	Silty clay	51.8	21.25	30.55
Nichols and Grismer (1997)	Imperial silty clay	-	-	-
Hallett and Newson (2001)	Silica sand:kaolinite (75:25)	-	-	-
	Silica sand:kaolinite (50:50)	-	-	-
Hallett and Newson (2005)	Kaolinite	63.5	31.8	31.7
	Silica sand:kaolinite (20:80)	52.0	25.4	26.6
	Silica sand:kaolinite (40:60)	40.5	20.3	20.2
Wang et al. (2007a)	Clay with gravels	29.1	20.2	8.9
Thusyanthan et al. (2007)	E-grade kaolin	51	30	21
Viswanadham et al. (2010)	Mixture kaolin sand	35(A)	20(A)	15(A)
		26(B)	17(B)	9(B)
		19(C)	13(C)	6(C)
Amarasiri et al. (2011)	Werribee clay	127	26	101
Plé et al. (2012)	Lower Aptien silty-clay	44	22	22

Table 2.5: Physical properties of the clays tested in bending tests used in literature

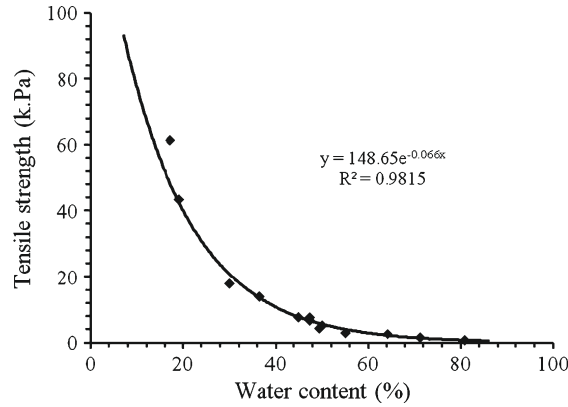
### 2.4.3 Results from the literature

Clay behaviour is particularly affected by the amount of water contained in the soil. Tensile strength, strain and Young's modulus are affected by the moisture content. Previous observations on the tensile strength showed different trends of values in relation to the moisture content (Towner, 1987; Lakshmikantha et al., 2008; Trabelsi et al., 2012; Tang et al., 2015; Stirling et al., 2015). In some cases the tensile strength decreased exponentially (Figure 2.27.a)) with the increase of the moisture content, in other cases it followed a polynomial (Figure 2.27.b)) or a bell-shaped curve (Figure 2.27.c)). Although differences in the tensile strength trends were recorded, these points could represent the same curve in different ranges of moisture contents. In fact, the range of moisture content used for the test was usually quite narrow, so it is possible that only a limited number of tensile strength values were recorded. However, in all the studies the tensile strength of the clay sample decreased for high moisture content. Tensile strength values increased quickly when the moisture content was lower than a critical value  $\omega_c$ , as is shown in Figure 2.27(c). Once this value was passed, the reduction of tensile strength was slow and seemed to reach an asymptote which indicated that the clay was no more affected by any increment of moisture content. The value of tensile strength reached at this stage was constant and it is defined residual tensile strength  $\sigma_{t,r}$ .

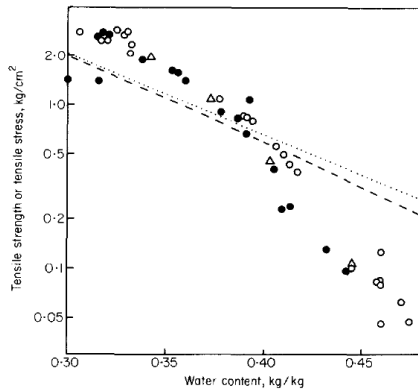
Except the cases in which the tensile strength was following an exponential curve which was easy to approximate with a line, only Tang et al. (2015) proposed a method to calculate a curve for the tensile strength points. They suggested the use of a system of two equations which was derived by the analysis of unsaturated sands in tensile conditions conducted by Lu et al. (2009). For a moisture content  $\omega$  smaller than the critical value of moisture content  $\omega_c$  ( $\omega \leq \omega_c$ ), the clay behaved like a granular soil so the equation found by Lu et al. (2009) could be used to calculate the tensile strength. For  $\omega > \omega_c$ , the clay was close to saturation so the term  $\sigma_{t,r}$  was added to the equation (Equation 2.15, Figure 2.28. Equations and Figure were modified in terms of moisture content). However, the clay used in the study was composed of 76 % silt and 22 % sand, so the equations could not be considered completely accurate for pure clay soil.

$$\sigma_t = \begin{cases} 2 \tan \phi \tan(\frac{\pi}{4} - \frac{\phi}{2}) \frac{\omega_e}{\alpha} [\omega_e^{\frac{n}{1-n}} - 1]^{1/n} & 0 \leq \omega \leq \omega_c \\ \sigma_{t,r} + 2 \tan \phi \tan(\frac{\pi}{4} - \frac{\phi}{2}) \frac{\omega_e}{\alpha} [\omega_e^{\frac{n}{1-n}} - 1]^{1/n} & \omega_c \leq \omega \leq 100 \% \end{cases} \quad (2.15)$$

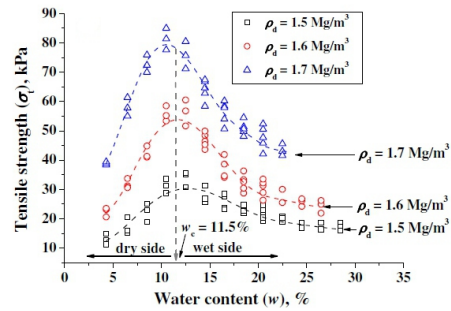
in which  $\phi$  is the angle of internal friction,  $\alpha$  is the inverse value of the air-entry pressure,  $n$  is the pore size spectrum number,  $\omega_e = \frac{\omega - \omega_r}{n - \omega_r}$  is the equivalent degree of saturation,  $\omega$  is the moisture content,  $\omega_r$  is the residual moisture content (see



(a)



(b)



(c)

Figure 2.27: Exponential, polynomial and bell-shaped trends of tensile strength  $\sigma_t$  taken from Traibelsi et al. (2012), Towner (1987) and Tang et al. (2015).  $\rho_d$  indicates the dry density at which the samples were tested

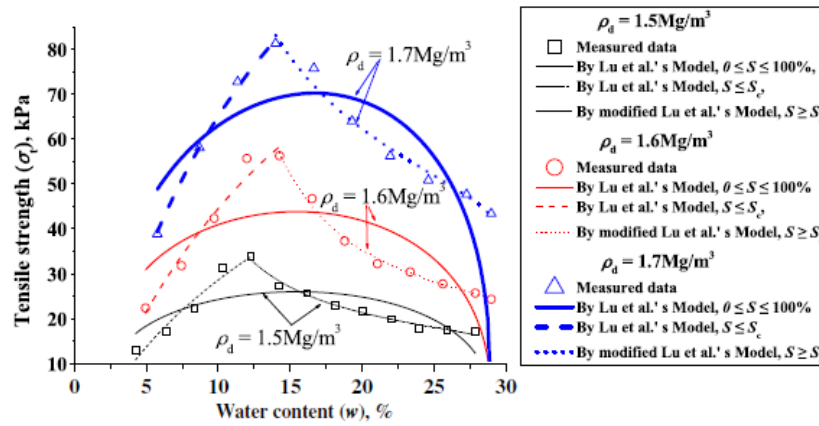


Figure 2.28: Approximation of the direct tensile results determined by Tang et al. (2015) (x-axis modified substituting the degree of saturation with the moisture content).  $\rho_d$  indicates the dry density at which the samples were tested

Lu et al. (2009), Lu et al. (2010) for more details, expressed in terms of degree of saturation).

Another parameter affected by the amount of water in the sample was the strain developed during tensile tests. Increasing the moisture content, samples were able to deform more before failure (Figure 2.29). The strain always increased even if the optimum moisture content was exceeded. A critical value was not identified, so clays with a high degree of saturation were able to sustain large deformations but they underwent cracking at low values of tensile stresses. This demonstrated that wet samples could sustain large deformations also when tensile cracks formed. The moisture content influence was also observed in the Young's modulus behaviour, as shown in Figure 2.30.

Also the plasticity index is related to the tensile strength of a soil. Using clays compacted at the optimum moisture content the relationship found by Fang and Hirst (1973) is shown in Figure 2.31. A wave curve approximated the data obtained in the double punch test (indirect test). This test is similar to a compression test in which two punches penetrate into a cylindrical sample. The tensile strength depends on the tensile test used to determine it because the area and the flaws involved vary from test to test depending on the volume under tensile conditions.

Plasticity index represents the range of moisture contents in which clays are able to deform without breaking. Figure 2.31 shows for low values of plasticity index, the tensile strength is low and therefore the clay cannot undergo large deformations before reaching failure. Instead, high tensile strengths were recorded in plastic clays where the soil could sustain deformations before failing.

## 2.5 Fracture mechanics in soils

The application of fracture mechanics to soils for studying tensile cracks has been used in the past by many authors (Farrell et al., 1967; Chandler, 1984; Nichols and Grismer, 1997; Hallett and Newson, 2001, 2005; Wang et al., 2007*a*; Viswanadham et al., 2010; Amarasiri et al., 2011). However a definitive understanding of the soil behaviour is far from being reached. The complexity of clay behaviour affects the formation of cracks and consequently their initiation and growth. Moisture content, plasticity index and clay mineralogy are the main parameters that change the soil's response.

Bending tests were usually used to characterise mode I fracture (Farrell et al., 1967; Chandler, 1984; Nichols and Grismer, 1997; Hallett and Newson, 2001, 2005; Wang

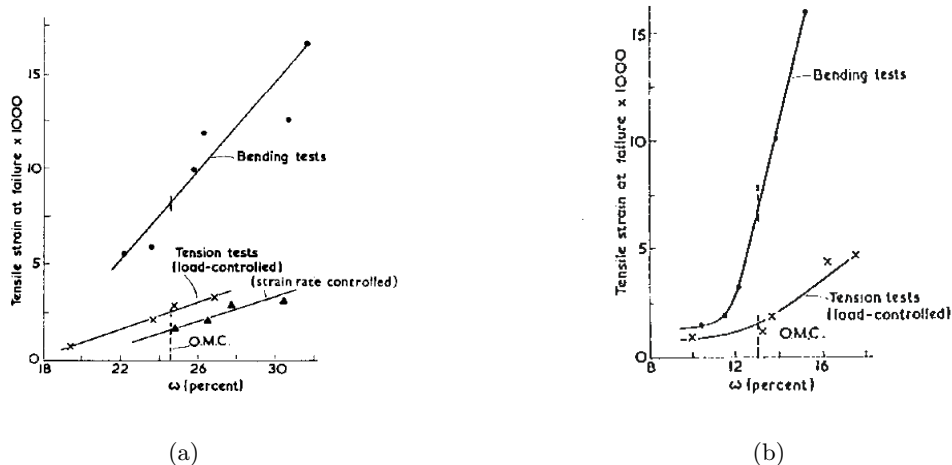


Figure 2.29: Variation of tensile strain at failure in relation with the moisture content for a) Gault clay and b) Balderhead clay (from Ajaz and Parry (1975))



### 2.5.1 Linear elastic fracture mechanics in soils

Under the linear-elastic assumptions, plasticity was assumed to take place only near the crack tip while all the rest of the element behaved elastically, allowing the fracture toughness to be calculated in a simple manner. Amarasiri et al. (2011) suggested an equation to calculate the fracture toughness  $K_{IC}$  for notched clay beams under bending load (Equations 2.16 and 2.17). The equation was modified from the ASTM:E1820-15 (2015) standard for the case in which the beams have a width  $B$  equal to the height  $W$ .

$$K_{IC} = \sigma_N \sqrt{D} k_{S_p/D}(\beta) \quad (2.16)$$

$$\sigma_N = \frac{3PS_p}{2bD^2} \quad \text{and} \quad \beta = \frac{a}{D} \quad (2.17)$$

in which  $\sigma_N$  is the nominal stress,  $D$  is a characteristic dimension (in this case equal to the height  $W$ ),  $\beta$  is a shape factor calculated as the ratio between the length of the initial crack to the specimen height,  $P$  is the maximum load,  $S_p$  is the span between the supports,  $b = W - a$  is the remaining ligament length.  $k_{S_p/D}(\beta)$  is a function of the factor  $\beta$  (see Amarasiri et al. (2011) for equations). The  $K_{IC}$  found assesses the amount of material resistance to crack propagation.

The fracture toughness is also affected by the moisture content. In Amarasiri et al. (2011), brittle failures with high values of  $K_{app}$  were observed for dry samples, while low  $K_{app}$  values were observed for wet samples. The variation was similar to that seen for the elastic modulus, as Figure 2.32 shows. Fracture toughness was called “apparent” because further numerical checks were needed in order to define the values as  $K_{app}$ . The data labelled “not modelled” stand for beams that were not numerically modelled due to their unsatisfactory post-peak response. Beams labelled “modelled” were modelled using the distinct element program UDEC.

Wang et al. (2007a) used the formula reported in ASTM:E1820-15 (2015) to calculate fracture toughness. They did not modify the width of the beam which remained  $B = 0.5W$ . They found a variation in the magnitude of  $K_{IC}$  different from that determined by Amarasiri et al. (2011) (Figure 2.33). They supposed the unsaturated soil studied could have changed the interaction force among the soil particles and

the specimen suction potential with the increment of moisture content from 15.4 to 19.6 %. Plotting the fracture toughness against the moisture content, it was possible to notice that an optimal moisture content exists in order to have a maximum  $K_{IC}$  value. The results found by Wang et al. (2007a) were in disagreement with the exponential curve determined from the tests performed by Amarasiri et al. (2011). The fracture energy  $G_f$  required to propagate a unit area of crack was calculated by Amarasiri et al. (2011) dividing the energy used to conduct the test by the area of fracture surface developed. The test energy was represented by the area under the load-displacement graph while the area of fracture surface was calculated multiplying the ligament length  $b$  by the sample height  $W$ . This energy was considered a material property, like  $K_I$ , and it varied with the moisture content, following a similar exponential fitting curve to that of the fracture toughness (Figure 2.34).

Amarasiri et al. (2011) also applied fracture mechanics theory to calculate the dimension of the crack tip plastic zone. From theory, the plastic zone is proportional to the ratio  $(K_{IC}/\sigma_{YS})^2$  and has the dimension of length. However, the Authors related the fracture toughness to the tensile strength  $(K_{IC}/\sigma_t)^2$  to estimate the dimension of the plastic zone. This ratio was calculated and plotted against the moisture content, but the results did not show a precise trend: the values seemed to be constant with the variation of moisture content (Figure 2.35).

Another relationship between fracture toughness and tensile strength was found by Wang et al. (2007b). They obtained a proportional value of 0.3546 between the two

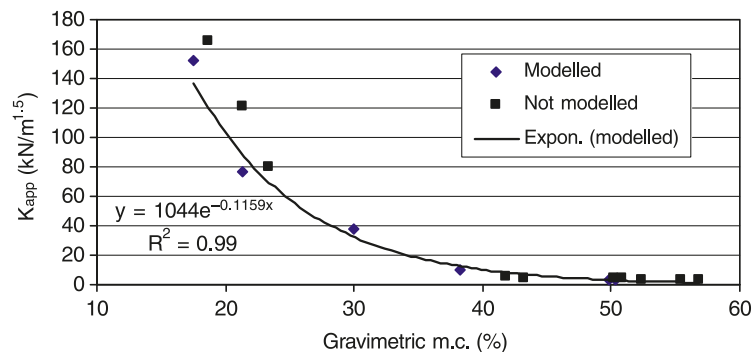


Figure 2.32: Variation of the fracture toughness with the moisture content from Amarasiri et al. (2011).

parameters:

$$K_{IC} = 0.3546\sigma_t \quad (2.18)$$

with a coefficient of determination  $R^2 = 0.88$  (Figure 2.36).

However, the standard ASTM:E399-12 (2013) for the LEFM analysis limits the dimension of the ligament length  $b = W - a$ . It must be greater than  $2.5(K_{IC}/\sigma_{YS})^2$ . In this manner the size of the fracture process zone is small enough compared to the dimensions of the specimen and LEFM can be used. But, it is very difficult to satisfy this geometry requirement because large samples are required. Amarasiri et al. (2011) concluded that the results found applying the LEFM had to be considered “uncertain”.

### 2.5.2 Elasto plastic fracture mechanics in soils

Although many authors (Nichols and Grismer, 1997; Viswanadham et al., 2010; Amarasiri et al., 2011) studied the bending problem assuming Linear Elastic Fracture Mechanics (LEFM), the soil behaviour was not linear elastic (Figure 2.37). The linearity was usually satisfied by dry samples or silty materials, while wet samples and clays behaved in a nonlinear manner. This different response was noticed by Amarasiri et al. (2011). Another indication of the nonlinear behaviour of the clay in tensile conditions was also noticed by Thusyanthan et al. (2007) and Ajaz and Parry

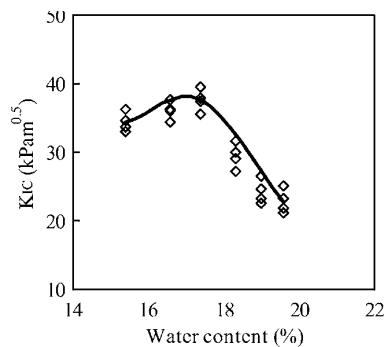


Figure 2.33: Relationship between the fracture toughness  $K_{IC}$  and the moisture content taken from Wang et al. (2007a)

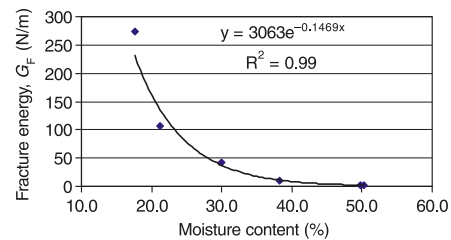


Figure 2.34: Fracture energy  $G_F$  variation with the moisture content (taken from Amarasiri et al. (2011))

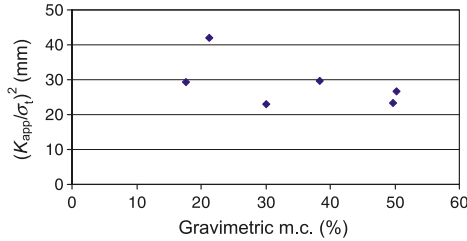


Figure 2.35: Crack tip plastic zone extension in dependence with the moisture content (taken from Amarasiri et al. (2011))

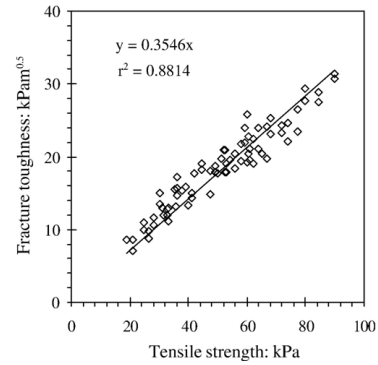


Figure 2.36: Linear variation between the fracture toughness  $K_{IC}$  and the tensile strength  $\sigma_t$  taken from Wang et al. (2007b)

(1975). Both studies calculated the stress along the beam central section proving that it was not linear after the crack formation. u;l;y

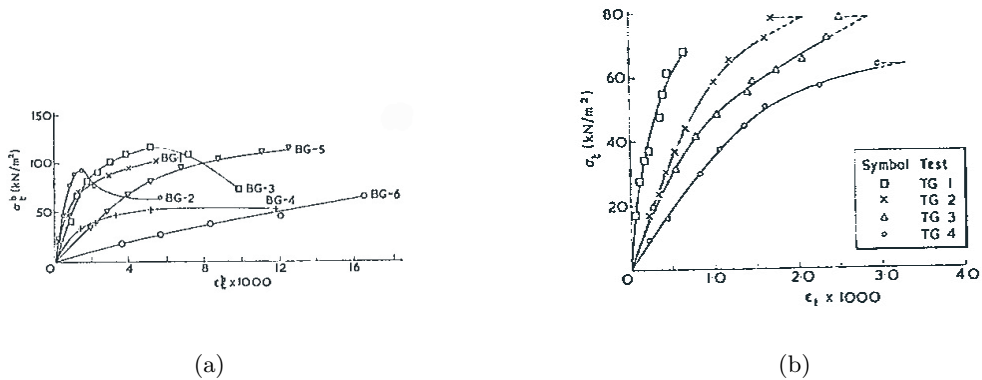


Figure 2.37: Stress-strain curves (a) for bending tests and (b) direct tensile tests on Gault clay (Ajaz and Parry, 1975)

For this reason, Elasto Plastic Fracture Mechanics (EPFM) started to be applied to soils, first by Chandler (1984) and Hallett and Newson (2001, 2005). Chandler (1984) applied the nonlinear fracture mechanics to determine the resistance of a soil to crack propagation. Using the J-integral, a crack will propagate when  $J > J_R$ , where  $J_R$  is the crack growth resistance. He tested clay samples in bending conditions to determine the crack growth resistance. From the results reported in Figure 2.38, clay soils with different moisture contents had a  $J_R$  that increased with the crack

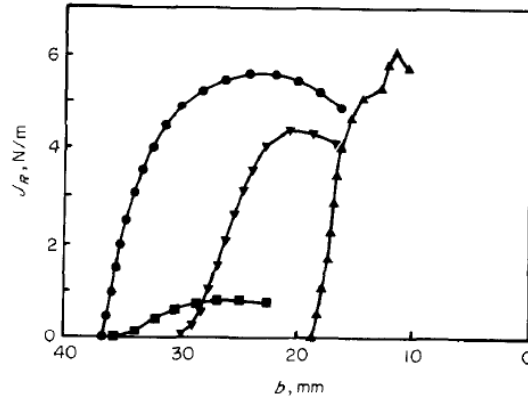


Figure 2.38:  $J_R$  curves versus the resistant ligament length found by Chandler (1984)

growth until a plateau was reached. This increase of  $J_R$  was related to the ability of ductile materials to take a permanent set. During the crack growth, previous deformation, not directly ahead of the crack ‘shields’ the crack tip (Chandler, 1984). So, an increase of  $J$  is needed to propagate the crack.

Hallett and Newson (2001, 2005) tested mixtures of kaolin clay and sand in 3-point bending tests and the loading graph obtained clearly showed the non-linear response of the beams. As it is possible to see from Figure 2.39, the initial response was linear (elastic region). After reaching a yielding point the transition between the elastic and plastic behaviour took place. Once the yield point was exceeded, the load

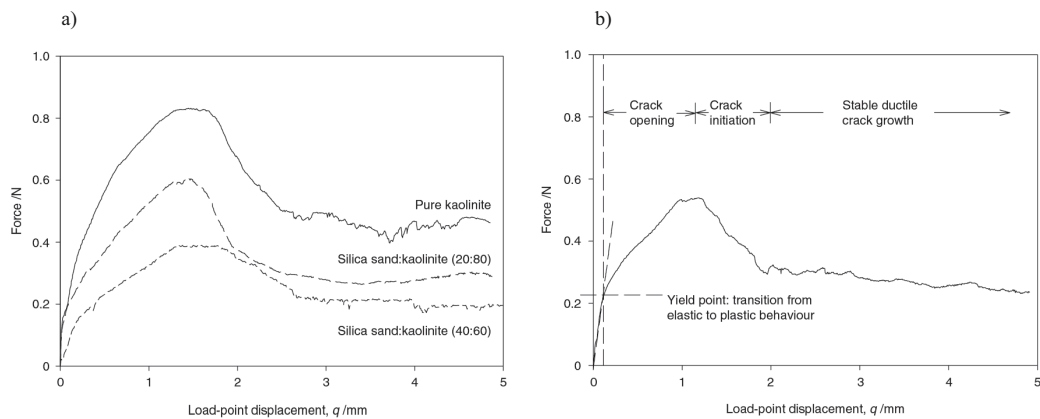


Figure 2.39: Loading diagrams obtained by Hallett and Newson (2005) and stages of the crack development in a kaolin beam wetted with saline

increased less steeply with a further development of displacements. At the crack tip the particles underwent re-orientation, breaking the inter-particle bonds and the matric suction became more negative. A sudden decrease of applied load suggested the beginning of the crack propagation. Then, the crack continued to grow until the energy stored in the system was completely dissipated. At this point an equilibrium was reached at a value similar to that of the yielding point. The crack was then able to grow in a stable ductile manner.

Hallett and Newson (2001) revised the use of the crack opening displacement (COD) to understand the development of cracks in wet clay beams. With the proceeding of the bending test, the initial notch opened before the propagation of the crack. The COD was the measure of the opening between the two faces of the initial notch caused by the plasticity. However, for very ductile tests where the crack was growing slowly, the calculation of COD at the moment of crack initiation was difficult due to the amount of bending strain. Therefore, Hallett and Newson (2001) proposed to use another similar factor called crack opening angle (COA) as a more reliable parameter to describe the ductile crack growth in wet clay beams. It provided a description of the behaviour of the entire crack and was defined as the ratio between the plastic crack mouth opening  $V_{pl}$  and the crack length  $a$  (Equation 2.19).

$$COA = \frac{dV_{pl}}{da} \quad (2.19)$$

Because the crack growth is localised at the crack tip, the COA was modified in order to account for only the plastic strain at the tip which was required to extend the crack. This new parameter was called crack tip opening angle CTOA (or  $\alpha_{g,pl}$ ). Describing the bending beam as a full plastic hinge and considering its geometry, the dimensionless ratio  $\alpha_{g,pl}/r_{pl}b$  could be determined as:

$$\frac{dq_{pl}}{da} = \frac{S_p \alpha_{g,pl}}{4r_{pl}b} \quad (2.20)$$

where  $S_p$  was the span of the beam,  $b$  was the thickness of the beam,  $q$  the point displacement, 'pl' indicated the plasticity field and  $r_{pl}$  was the instantaneous centre of rotation of the tested beam (dimensionless) calculated using Equation 2.21

$$r_{pl} = \{(S_p/4)(dV_{pl}/dq_{pl}) - a_0\}/b_0 \quad (2.21)$$

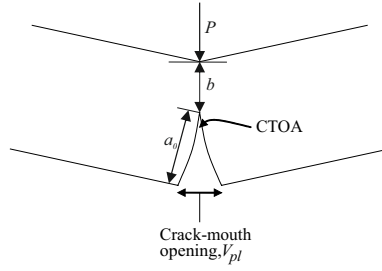


Figure 2.40: Symbols adopted by Hallett and Newson (2005) to describe the ductile crack growth

in which  $a_0$  was the length of the initial notch and  $b_0$  was the length of the initial resistant ligament (Figure 2.40).

The Hallett and Newson (2001) results showed that CTOA was influenced by the plasticity index of the soil. The crack tip opening angle reduced for low levels of clay contents as the samples sustained less bending and were more susceptible to sudden cracking.

Moreover, in the same study the energy dissipation rate  $D$  was used to describe the crack growth resistance instead of using the J-integral theory. For wet soils, which usually have a high ductility, the elastic energy dissipation was considered negligible, so

$$D \approx D_{pl} \quad (2.22)$$

where  $D_{pl}$  was the plastic energy dissipation rate, determined as:

$$D_{pl} = \frac{L\sigma_{YS}b\alpha_{g,pl}}{4r_{pl}} \quad (2.23)$$

in which  $\sigma_{YS}$  was the uniaxial yield stress and  $L$  was the plastic constraint factor equal to 1.57 for  $a/W \approx 0.5$ . Dry soils behaved in a more elastic manner, so the energy dissipation rate was calculated as:

$$D = D_{pl} + D_{el} = \frac{L\sigma_{YS}b\alpha_{g,pl}}{4r_{pl}} + G \quad (2.24)$$

in which  $D_{el}$  was equal to the energy release rate  $G$  found in the LEFM (Table 2.6). From the literature reported, the usual method to analyse the tensile behaviour of soil is to adapt the fracture mechanics theory found for metals to fit the clay behaviour. A different approach was followed by Thusyanthan et al. (2007). They tried to fit the bending problem and the fracture mechanism in a geotechnical point

of view. The tensile behaviour was related to the Cam-Clay yield surface, in which the initial effective stress was determined by the initial negative pore pressure. From the stress paths, two different lines of failure were identified in the tension area: a tension cut-off line or an ‘apparent failure line’ similar to the Hvorslev line of failure state. Thusyanthan et al. (2007) found that beams with an initial low negative pore pressure were failing touching the zero effective tension line while beams with a higher suction failed touching the ‘apparent failure line’. The difference in failure was also reflected in the crack inclination: low initial suction produced a mode I crack, meanwhile higher suction produced a mixed mode crack (Figure 2.41).

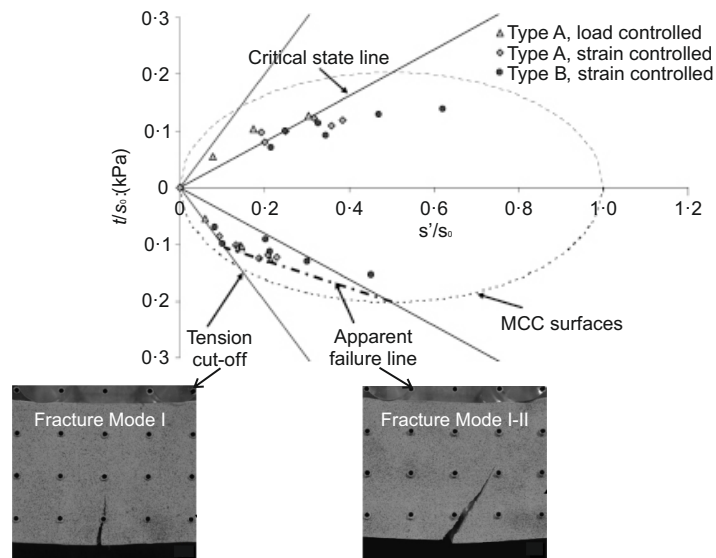


Figure 2.41: Difference in the crack formation in relation to the initial negative pore pressure (Thusyanthan et al., 2007)

Sample	$\sigma_{YS}$ (kPa)	$E$ (kPa)	COA	$\alpha_{g,pl}/r_{pl}$	$D_{pl}$ ( $\text{Jm}^{-2}$ )
75:25 Sand:Clay	165	14500	$0.523 \pm 0.066$	$0.223 \pm 0.051$	$173 \pm 40$
50:50 Sand:Clay	28	2400	$0.600 \pm 0.018$	$0.147 \pm 0.011$	$18.3 \pm 1.4$

Table 2.6: Parameters obtained by Hallett and Newson (2001) after studying soil beams in 3-point bending tests

## 2.6 Summary

The literature review demonstrates that sinkholes usually occurred in layers of clay mixed with sand and silt. The main triggering factor that determined the sink-hole initiation was related to the lowering of the ground water table. In general, the clayey layer was located at a shallow depth and its height was limited to a maximum of 15 m. On the surface, the hole in the ground reached at maximum of 10 m both in diameter and in depth. Other geotechnical properties were usually not reported in the literature. Only few data regarding the plasticity index, the moisture content and the specific weight were reported to characterise the clayey layer over the cavity. Clay therefore represents a valid material to study crack formation in tensile conditions using both direct tensile and bending tests.

The most straightforward approach that can be used to describe the crack growth is linear elastic fracture mechanics (LEFM), however clays usually do not behave linearly. Under linear-elastic conditions, the significant influence of the moisture content on the tensile response was highlighted, however different relationships were found in every study. The same disagreement was also found in terms of fracture toughness and its relationship with tensile strengths.

Nonlinear theory for tensile behaviour was more suitable to describe the load / displacement and fracture response. Chandler (1984) used the nonlinear fracture mechanics theory to determine the crack growth resistance. Hallett and Newson (2001, 2005) suggested the use of the crack tip opening angle (CTOA) as the main parameter to study the nonlinear fracture formation after having performed bending tests on clays. From their results elasto-plastic fracture mechanics (EPFM) appeared to be more appropriate to study clays behaviour in tension.

In general, the literature proves that moisture content and plasticity index play an important role in the determination of the clay behaviour. Wet beams presented a lower capacity to resist cracking but sustained more deformations. For this reason, moisture content of clay layers determined the fracture resistance of soils.

## Chapter 3

# Experimental methodology

The chapter focuses on the equipment and procedures adopted during the laboratory experiments and subsequent analysis. The chapter ends with a list of factors that affected the experiments and consequently the results.

### 3.1 Material selection

The data collection from the historical cases of sinkholes (Section 2.1.2) has highlighted that catastrophic collapses can take place in clay dominant behaviour. Therefore the research focused only on clays. From further research in the past literature, it was possible to see that mixture of clays with sand were usually preferred to study in tensile conditions. Just a few studies were done on the tensile behaviour of pure clays. Only four types of clays were studied: E-grade kaolin by Thusyanthan et al. (2007), Werribee clay by Amarasiri et al. (2011), montmorillonite by Nichols and Grismer (1997) and Gault clay by Ajaz and Parry (1975).

In this research, three clays were chosen to be investigated in tensile conditions: Speswhite kaolin, London clay and Durham clay. The choice of those three materials was related to the possibility of studying clays with varied plasticity index, from a clay that behaves in a very plastic manner (London clay) to a mixture of clay with sand with a low plasticity (Durham clay).

The first clay that has been studied was Speswhite kaolin clay. It is an artificial clay used for producing china. Even though it was not representative of a natural

clay it was used to study the tensile characteristics of a pure clay. Kaolin has been widely studied in the literature, so its properties and characteristics are well known. In addition, it was quickly available in the Engineering building.

The second clay chosen was a boulder clay coming from Durham University. It was used in previous research on the effects of climate changes on embankment stability (Hughes et al., 2009). The Durham clay is a boulder clay made by a glacial till. The clay matrix of illite, smectite, chlorite, kaolinite was mixed with coarse particles including gravels and sand.

The last clay used in the research was London clay. The choice of London clay was due to its known behaviour and high plasticity index  $PI$ . The material was available in the Engineering Department as it was used in previous studies. The clay has been extracted from the ground and stored as soil cores in plastic tubes. So tests were performed both on undisturbed samples taken from the in situ soil core and on reconstituted samples.

Table 3.1 reports the liquid limit  $LL$ , plastic limit  $PL$ , plasticity index  $PI$  and optimum moisture content  $\omega_{OMC}$  of the soils used during the laboratory experiments. The Atterberg limits for kaolin, Durham and London clays were calculated as part of the investigation. The optimum moisture content was calculated for kaolin clay while the values regarding Durham and London clays were determined from literature (Glendinning et al., 2014; Sivakumar et al., 2015; Mavroulidou et al., 2013). Figure 3.1 reports typical particle size distributions found by Ahmad et al. (2015), Toll et al. (2012) and Mavroulidou et al. (2011) for Speswhite kaolin, Durham and London clays.

Soil name	LL (%)	PL (%)	PI (%)	$\omega_{OMC}$ (%)
Speswhite kaolin	65.0	34.0	31.0	34.0
Durham clay	41.7	23.3	18.4	15.5 <sup>a</sup>
London clay	75.3	33.5	41.8	24.5 <sup>b</sup>

Table 3.1: Geotechnical properties of the clays used for the laboratory experiments

<sup>a</sup> indicates a value found in Glendinning et al. (2014)

<sup>b</sup> average of the values found by Sivakumar et al. (2015), Mavroulidou et al. (2013)

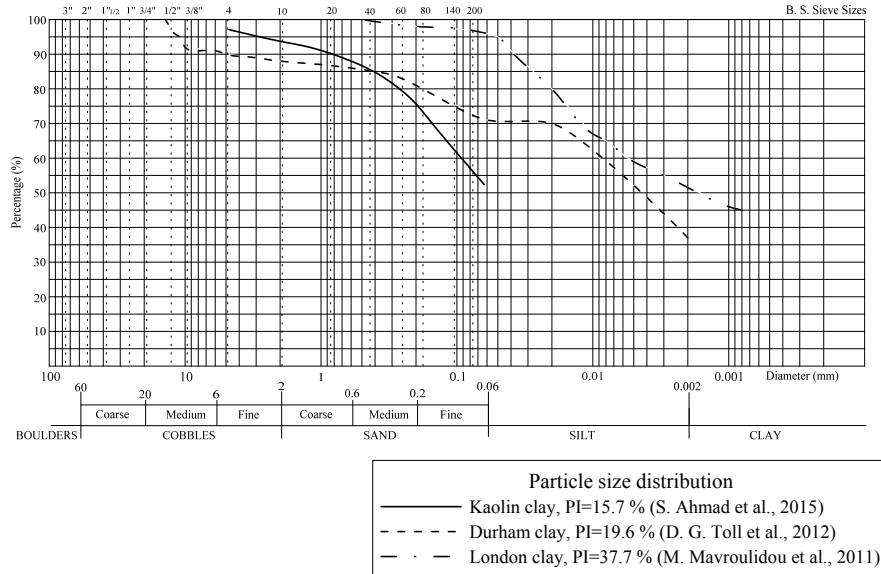


Figure 3.1: Particle size distribution of the kaolin, Durham and London clays

### 3.1.1 Sample preparation

Kaolin and Durham clay were stored in powder form. So, testing samples needed to be prepared in order to obtain solid beams.

To obtain samples that could be cut into different shapes the soil needed to be consolidated in hard blocks. The kaolin clay was bought in powder form and it was mixed with water in a ratio equal to 1.1 times the liquid limit,  $LL$  to create a slurry. A slightly longer procedure was adopted for the Durham clay. As it contained sand and gravels, a sieving procedure was adopted. Only the particles passing the  $600 \mu m$  sieve were used for the tests in order to eliminate the largest soil particles represented by coarse sand and gravels. In this manner large particles did not influence the crack formation in samples with a maximum width of 20 mm. The soil passing the  $600 \mu m$  sieve was then mixed with water in a ratio equal to 1.0 times the  $LL$  to create a slurry. The same procedure was adopted by Stirling et al. (2015) who tested only the natural soil passing through the 5 mm sieve. They stated that tests were impractical when the large grains were greater than 2 % of the total volume of

the specimen.

London clay stored in the University was extracted from the core tubes and then tested. Then it was dried, reduced to powder and mixed with water in a ratio 1.2-1.3 times the  $LL$  to obtain a slurry.

The soil and water were mixed for 15 minutes using a Kenwood kitchen mixer to obtain an almost homogeneous slurry. Some small lumps of agglomerated powder remained into the mixtures and they could be considered as flaws for the experiments. The mixtures were then left to rest overnight to let the water fully hydrate the clay particles. The slurry prepared was then poured into the Rowe cell (25 cm diameter) and consolidated to a pressure of 200 kPa in stages. The pressure stages were 0, 10, 25, 50, 100 and 200 kPa. The final pressure was chosen in order to have a soil that could sustain its own weight without losing a high quantity of water. Single and double height Rowe cells were used in relation to the amount of material available to test. Kaolin and Durham clays were consolidated using a double height Rowe cell. The London clay was consolidated with a single height Rowe cell using the same pressure stages. This choice was justified by the small amount of material available for the tests.

Once the consolidation was finished the sample was extracted from the Rowe cell ring applying a pressure on the top and leaving the bottom of the cell open. In this manner round shaped blocks of clays were obtained (Figure 3.2). This mode of extraction caused some soil disturbance to the clay which underwent differential loading and deformations. The cylindrical samples extracted from the Rowe cell were initially cut in quarters using a large wire cutter (Figure 3.3). Every single quarter was then cut using a smaller wire cutter and knives in the shape used for the tests. The required shape was obtained using moulds shaped with the final geometry. The moulds were placed on the clay and the extra soil was cut out with a wire cutter until the desired geometry was obtained.

In agreement to what was found by Hallett and Newson (2005), no particular attention was paid to the platelet orientation during the cutting process. It was proven that there is not a significant correspondence between applied load and the soil fabric. Principal stress directions do not affect the average platelet orientation. Also

Chenu and Guérif (1998) did not find an influence between the platelet orientation and the rupture stress of soil.

At the end of the consolidation the clays were considered saturated but they became unsaturated when they were extracted from the Rowe cell. To prevent the complete desaturation of the clay due to the air-cooling system of the laboratory, the samples and the unused soil were wrapped in cling film and stored in plastic containers. The time passed between the specimen preparation and the test was less than 24 h.



(a)



(b)

Figure 3.2: Kaolin sample extracted from a single height Rowe cell (a) and a Durham clay sample extracted from a double height Rowe cell (b)



Figure 3.3: Specimens preparation from a Rowe cell sample

## 3.2 Tensile test samples

A series of direct tensile tests was performed to determine the tensile strength of the different clays. The direct tensile test for metals is standardised by ASTM:E8/E8M-15a (2015): procedure, setup and sample dimensions are listed in the regulations. Usually metals are cut in long specimens with a small width, in order to create a nearly bidimensional specimen. The extremities of the samples are made slightly bigger compared to the central part. In this manner the crack formed by tension is forced to form in the middle section of the specimen length, where the area is smaller. The samples are then gripped to a loading frame by the extremities and subjected to tension pulling apart the two ends.

In the soil case, the procedure was the same of that used for metals but the setup and specimens' geometry were different. Soil cannot be gripped to the loading frame as in the case of metals because clays are less stiff and resistant. A grip fixed on the sample base would have broken the specimen base causing cracks and loss of contact with the frame. In addition, to let the sample crack in the middle section, the dimensions adopted for the metal specimen needed to be modified as per other studies on clays (Amarasiri et al., 2011). The presence of sand and the consequently lower plasticity did not allow the adoption of the same geometry of that used for metals.

In Farrell et al. (1967) the problem of the grips at the extremities was solved using epoxy resin. The extremities of the samples were glued to the loading frame supports. The same method was adopted here to test clays in tension. Due to the use of glue the geometry had to avoid the breakage at the base where the resin was used. The geometry was then modified with the increase of the cross section at the base and the reduction of the cross section in the central part of the sample. Different geometries were tried in order to obtain a crack in the desired place in the central section with a constant area. The final geometry adopted is shown in Figure 3.4. The two extremities of the samples had a squared shape measuring  $25 \times 20$  mm and 2 mm high. The central section had dimensions  $5 \times 20$  mm. Elliptical connectors were used to link the base with the central part.

A slightly different geometry was adopted for the Durham clay due to the higher content of sand compared to the other two clays. Due to the presence of the sand, it was difficult to cut samples with a thin middle section as done for the kaolin and London clay. Therefore, the cross section in the middle part was kept with a width of approximately three times that used for the other two types of clays (Figure 3.5). In this case, the geometry of the extremities was kept equal to that adopted for kaolin and London clay. Instead in the central part the dimensions were  $15 \times 20$  mm. After having cut the samples, coarse sand was pressed into the base surfaces of the samples and glued with super glue to increase the base roughness. This increase of friction at the bases guaranteed a better bond between the specimens and the epoxy resin, creating a strong contact between the soil and the loading rig. The samples were then glued using araldite epoxy resin to two thin aluminum plates which successively fixed to the frame (Figure 3.6).

### 3.3 Bending test samples

The beams used in the bending test were cut directly from the rounded samples extracted from the Rowe cell. At the end of the consolidation both kaolin and London clay had a moisture content equal to 49-50 %, while the Durham clay had a lower moisture content of 26 %. The choice of the beam geometry was based on the usual dimensions adopted for concrete bending tests in order to have a long beam and neglect the displacement caused by shear. In addition, on the basis of the clay beam geometries found in the literature (see Table 2.4), beams were cut using the ratio span  $Sp$  equal to 4 times the height  $W$  ( $Sp = 4W$ ), height  $W$  equal to the width  $B$  ( $W = B$ ), initial notch length  $a$  equal to half of the height  $W$  ( $a = 0.5W$ ). The total length  $L$  of the beams was chosen to be equal to five times the height  $W$ .

For bending beams, it was decided to maintain a span equal to four times the height. The clay beams with  $Sp = 5W$  underwent significant deformations when placed over rollers. Beams with an increased span underwent large deformations before the load application.

Beams of dimensions  $20 \times 20 \times 100$  mm were cut from the rounded samples taken

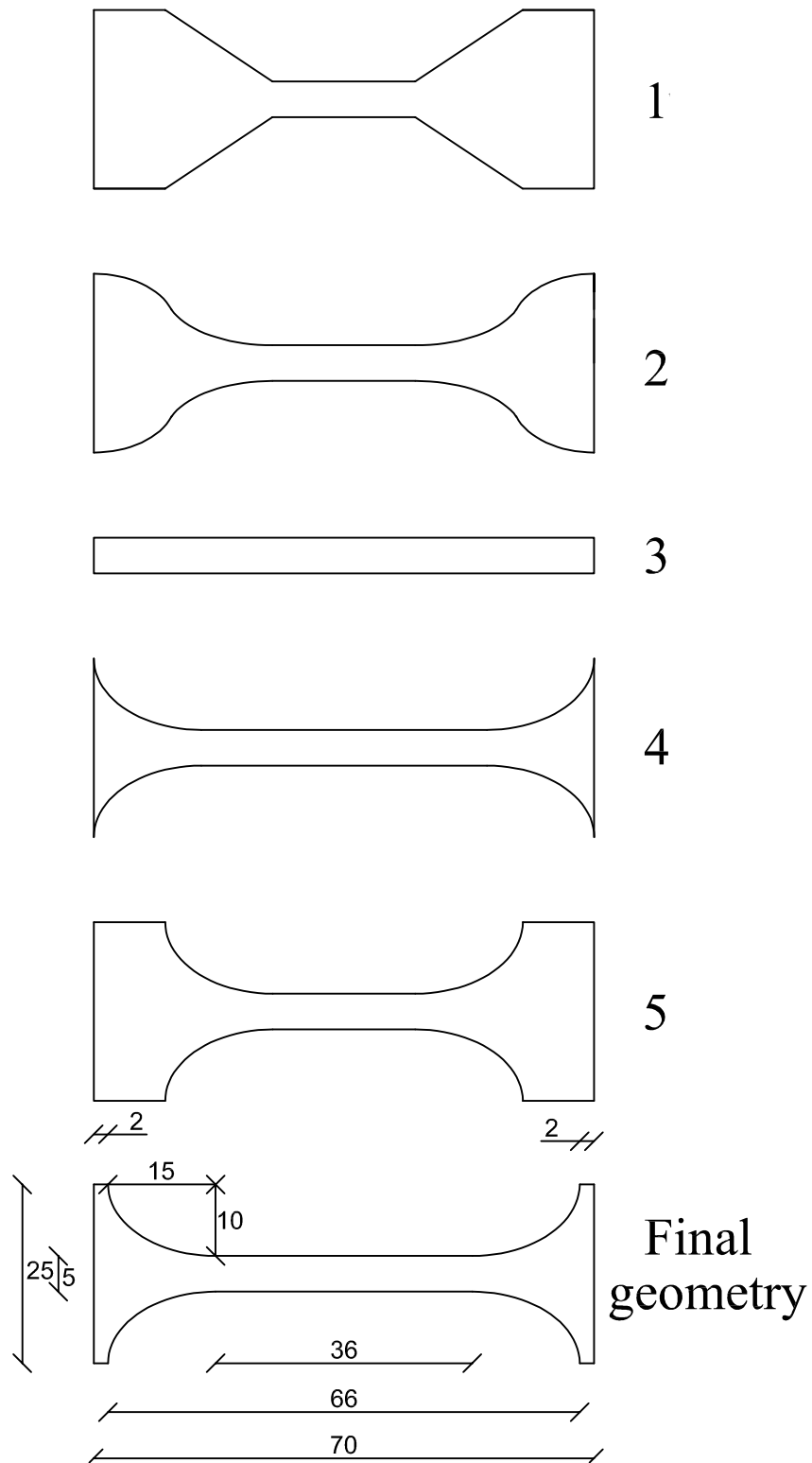


Figure 3.4: Trial and final geometries tested during the direct tensile tests (dimensions in mm)

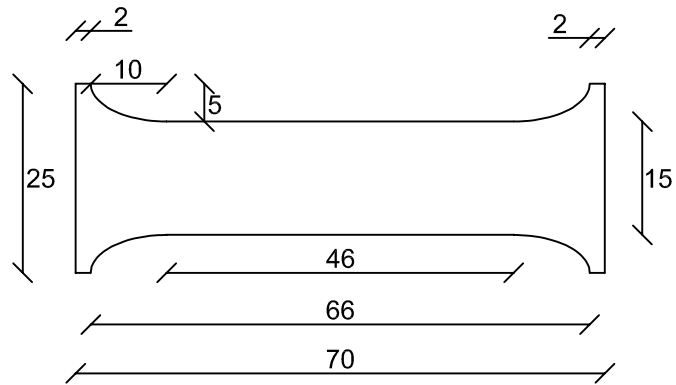


Figure 3.5: Modified geometry adopted for samples made with Durham clay (dimensions in mm)



Figure 3.6: Tensile sample fixed to the loading frame

out from the Rowe cell. In the central section of each beam a notch of a length equal to half of the thickness was cut using a wire cutter (Figures 2.26.b)).

Hallett and Newson (2005) placed two rigid supports under the two specimen's halves. These supports were attached to the load cell, but they were free to move on the rollers. A similar setup was also used in previous tests made by Hallett and Newson (2001), as Figure 2.26.a) shows. Two glass slides supported the beam and they were counterbalanced by two weights. Beam supports were not used in the investigation because they were considered elements of resistance to the load application. Without them, the specimens were affected by the gravity force. However, this situation is believed to be more similar to a possible real situation in which the supports are not present.

A wide range of moisture contents was tested in order to cover different clay responses. To simulate the water variation bending beams were oven dried at  $40^\circ$  for 0, 90, 150 minutes for kaolin, 0, 30, 90 minutes for Durham clay and 0, 45, 90 minutes for London clay.



Figure 3.7: Preparation of samples in London clay to use in bending tests

### 3.4 Drying analysis

The main objective of the research was to study the influence of the moisture content on the tensile behaviour of the clays. For this reason, samples ranging from a dry to a wet condition were tested. Consequently the moisture content of every sample studied was different.

To obtain a wide range of values, a drying process was used. Once extracted from the Rowe Cell, the round shaped samples were relatively wet and soft, so the specimens cut from the round samples were then dried in a oven at 40° C for 30, 90 or 150 minutes. However, before applying this technique to the samples, a drying analysis was done on trial specimens. The aim was to understand if the variation of moisture content could be considered insignificant and if the drying process was causing strong water variations throughout the length of the sample.

This process was applied only on samples with the same geometry of that adopted for the bending tests: in the geometry chosen for the direct tensile test the central section of the beam was so thin that the moisture content was considered constant. The 100 mm-long beams were cut in 5 parts along the length. Each part was a cube of dimensions equal to 20 × 20 × 20 mm and in that the moisture content was considered constant throughout the volume. The moisture content was initially

measured on beams not dried in the oven, so it represents the moisture content of the soil extracted from the Rowe Cell.

The values of moisture contents found after the oven drying are shown in Figure 3.8. As expected the maximum drying took place at the ends of the beams where three sides were subjected to the hot air of the oven. In the central part the moisture contents remained usually higher than the extremities and almost constant. The variation of moisture content in the parts numbered 2-3-4 was usually small (0.5 % as average). For this reason, moisture content in the central part was considered constant. This uniformity was mostly appreciable in beams not dried in the oven and for beams dried less than 150 minutes.

During longer drying process (150 min) beams lost more water: the lowest moisture content was recorded at the extremities and the highest in the central section. Kaolin showed a high variability after 150 minutes drying: the highest value of  $\omega$  was recorded in the middle section while the moisture content decreased more than 0.5 % in the remaining parts.

### 3.5 Test procedure

Both experiments were carried out using the same AGS-X Shimadzu loading frame. The main difference between the two experiments was the direction of the applied displacement and consequently the direction of the motion of the mobile brace. In the first type of tests clay beams were studied under tensile conditions: the mobile brace of the loading rig moved upwards applying a tensile force on a specimen. In the second type of experiments the loading rig worked in compression and the top part of the frame moved downwards.

A 10 kN load cell was attached to the moving brace. Even if the samples tested were very small, the loading cell was able to record the load variations (from 1 N to 50 N). The choice of a high capacity load cell can be explained in two points. Firstly, it was the only loading cell quickly available for testing as it was already part of the loading rig. Secondly, the load cell was tested in tension under small loads to check

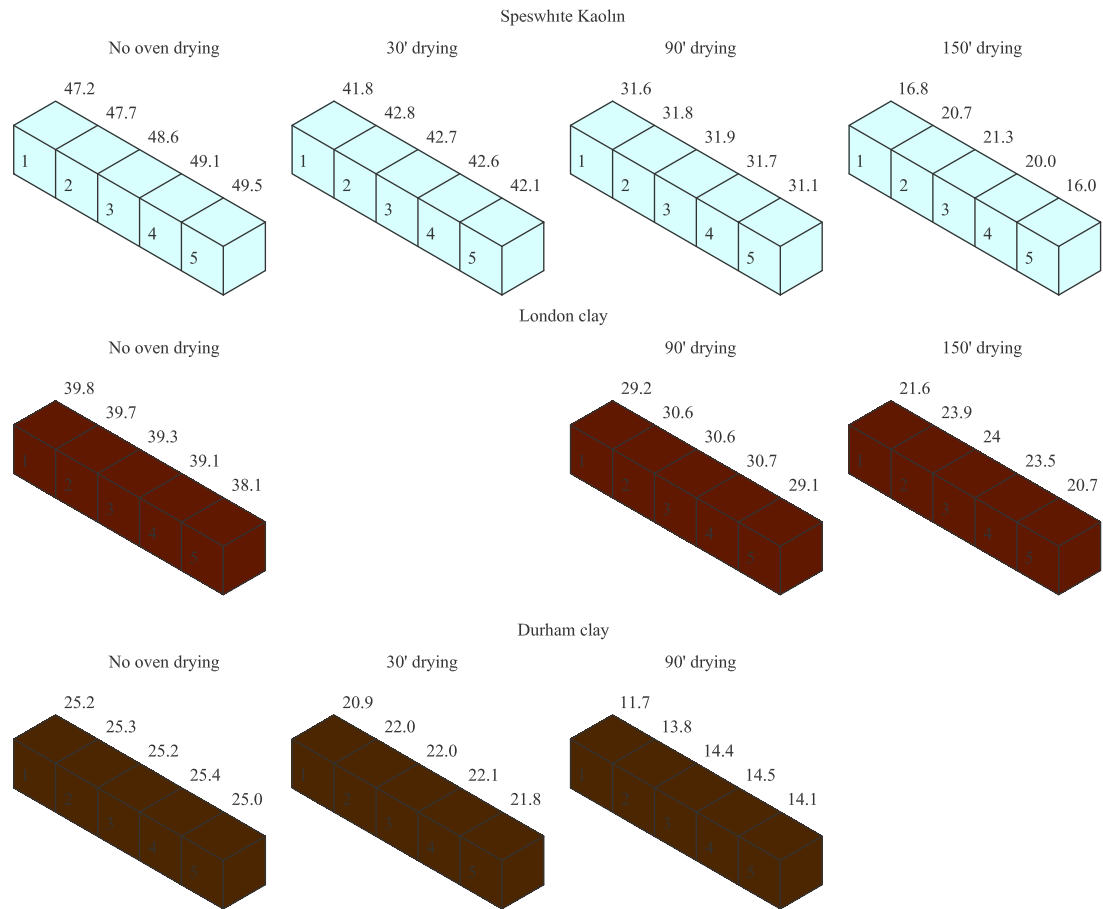


Figure 3.8: Drying analysis on the clayey beams used during the laboratory tests

its accuracy. A set of known weights were attached to the load cell and the tensile load measured by the cell was recorded (Figure 3.9). The data collected showed the relationship between the known weights and the data recorded by the load cell (Figure 3.10). When the weights were small the load cell was unable to record the correct magnitude of force. As a result the percent error was very high. However, with the increase of the weights the error decreased exponentially reaching a value equal to 2% for a weight of 2 kg. Figure 3.11 shows the results of the relationship between the tensile force and the related percent error derived from the simple load cell calibration in tensile condition. A similar behaviour of the loading cell was supposed in the case of compression, i.e. for the bending tests.

Both the bending and the direct tensile tests were performed in a displacement mode applying a rate of displacement of 1 mm/min (strain controlled mode). This ratio

was chosen on the basis of the strain rates found in literature (Hallett and Newson, 2001, 2005).

Different base supports were prepared in order to use the same loading rig in both tests. For the 3-point bending test a bottom support made by aluminum was made to allow the placement of two rollers. Two semicircular holes were made at a distance of 70 mm from each other. Aluminum rollers were then placed in those two holes to support the beam. Rollers had a diameter of 6 mm and a length of 70 mm. They were left free to rotate as they were working as simple supports. At the top, an aluminum piece was screwed into the loading cell. It had a reverse triangular shape with a semicircular hole at the tip. The cavity allowed the placement of a roller for a better distribution of the force on the sample (Figure 3.12).

For the tensile tests a support able to prevent the upward movement of the specimen was made. Aluminum bases with two threaded rods were used. The two pieces were attached to the loading rig, one to the fixed part of the loading rig and one to the mobile brace. Samples were then glued on small aluminum plates, which were then screwed to the threaded rods of the supports (Figure 3.6).

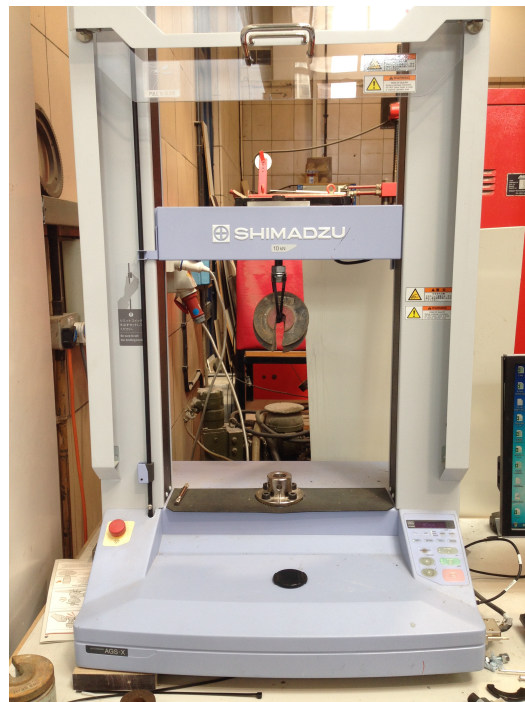


Figure 3.9: Simple load cell calibration in tensile conditions

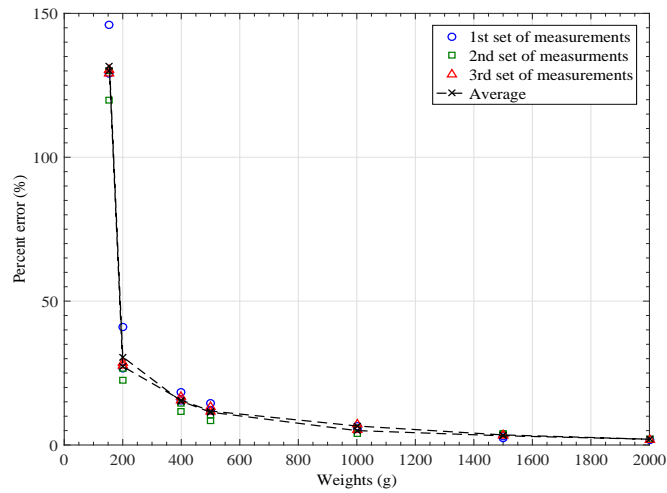


Figure 3.10: Load cell percent error under tension loads

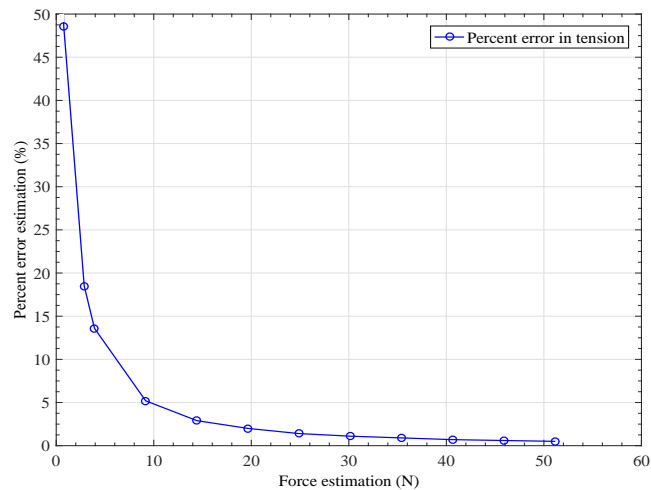


Figure 3.11: Relationship between the percent error and the tensile force calculated from the load cell calibration in tension

Samples were tested using different moisture contents. However, practical limits were encountered during the tests at the two extremes of the water range adopted during the tests. Very wet beams had difficulties to sustain their own weight, so they underwent bending of the central section before the load application. On the other hand, dry specimens were so fragile that any impact caused their breakage. The moisture content was measured immediately after the tests weighing the central

part of the sample.

In some tests, wetter samples than those obtained with the Rowe cell were studied. To increase the moisture content clay beams were stored in sealed box with a wet cloth under and above the sample surfaces. The cloth was kept on the sample for 12-24 hours.

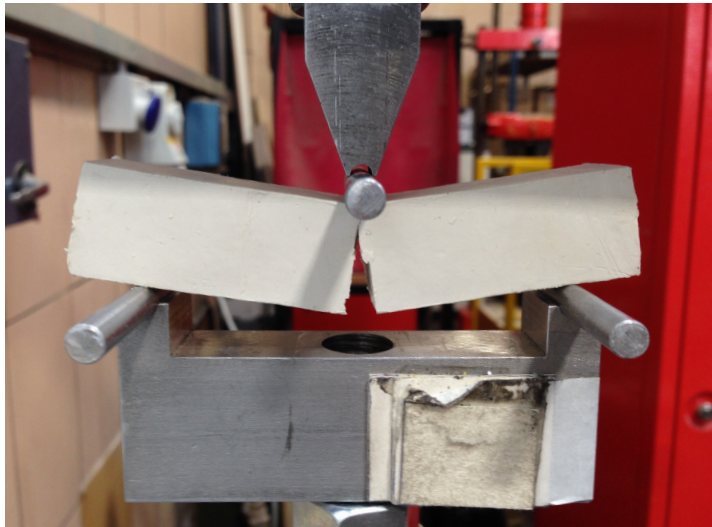


Figure 3.12: Setup adopted during the 3-point bending tests

### 3.6 GeoPIV

GeoPIV is a Matlab algorithm developed by White (2002) which is used to analyse displacements and strain paths during geotechnical testing. The module is based on the use of Particle Image Velocimetry (PIV): sequences of digital images are compared to each other due to the differences in the pixels texture. Thanks to the ability of the software to track the movement of the pixels from one image to another, displacements and strain paths are identified.

In order to use GeoPIV the experiments were recorded using a digital camera. The camera used was a Pentax K10D with a lens of focal length varying from 18 to 55 mm. The characteristics of the camera are listed in Table 3.2.

The camera was fixed on a tripod and placed in front of the loading frame. Using

a wire remote the camera was used in continuous mode throughout the test (3 fps). The camera was set on manual focus mode and the lens was used at the maximum of its focal length (55 mm). The aperture chosen was  $f/8$  and the exposure time was  $1/125$ . The ISO sensitivity to the light was set to 100.

The parameters manually set on the camera and the corner position of the loading frame gave underexposed photos as result. To enhance the quality of the pictures a pair of halogen lamps were used on the side of the camera providing photos of good quality for the PIV analysis.

With the images recorded by the cameras, PIV analysis was performed on a selection of beam specimens. Although GeoPIV represents a powerful tool for the understanding of the displacements and strain fields, it suffers from various problems. First of all, as the module works on digital images, a good texture is necessary to perform the analysis. Differences in brightness and colour scale are required by GeoPIV to track the movements of the pixels from image to image. Coarse-grained soils (i. e. sand) present a good natural texture for the digital images as colours and shades produced by the grains create a varied texture. Fine-grained soils as clay, cannot provide a good texture as the colour intensity is more uniform compared to that of sand. Consequently, an artificial texture was created on the samples' surface using coloured modeling flock which was spread on the sample surface (Figure 3.13). Two different colours, yellow and brown, were chosen to create better contrast and shades.

To increase the efficiency of the PIV analysis the photos were edited using the Matlab Image Processing Toolbox, which uses a series of algorithms, functions and options to process, modify and visualise images. The photos taken during the experiments were first converted into grey scale intensity images. The change of colormap can be explained using the upper bound curve found by White (2002) in his assessment of PIV precision. He performed the PIV on a series of photos capturing a rigid-body movement of a planar body placed below a fixed camera. Images of the body before and after the movement were recorded. From the analysis, it was possible to measure the precision of the PIV technique looking at the variation of the displacement vectors. The experiments showed a close relationship between the chosen dimension

<i>Image Sensor</i>	
Type	CCD
Maximum resolution	3872 × 2592 px
Effective pixels	Approx. 10.2M
Aspect ratio (W:H)	3:2 (23.7 × 15.6 mm)
<i>Lens</i>	
Focal length range	18.0-55.0 mm
Aperture range	$f/3.5 - 22$ (wide angle - W), $f/3.5 - 38$ (telephoto - T)
<i>Exposure Control</i>	
Shutter speed range	30-1/4000
Exposure Compensation	+/- 3.0 EV in 0.3 EV
ISO sensitivity	Auto, 100, 200, 400, 800, 1600, ISO priority AE
<i>Capture Rate</i>	
Maximum Rate	3 fps

Table 3.2: Pentax K10D specifications

of the element of the mesh (patchsize  $L$ ) and the image content. The upper bound error curve obtained by White (2002) was:

$$\rho_{pixel} = \frac{0.6}{L} + \frac{150000}{L^8} \quad (3.1)$$

The same process was applied to the images recorded during each test. PIV analysis was done on an original image and an image digitally translated of 10 px. The displacement data found in this manner allowed the calculation of the standard deviation error in the horizontal and vertical direction in relation to the variation of the patch size dimension.

Comparing the standard deviation found for the original images recorded during the tests and the images converted in greyscale it was possible to see that PIV worked better on images in greyscale. The standard deviation was lower both for the vertical and horizontal displacements (Figures 3.14, 3.15).

Photos were then modified using two transformation functions to improve the inten-

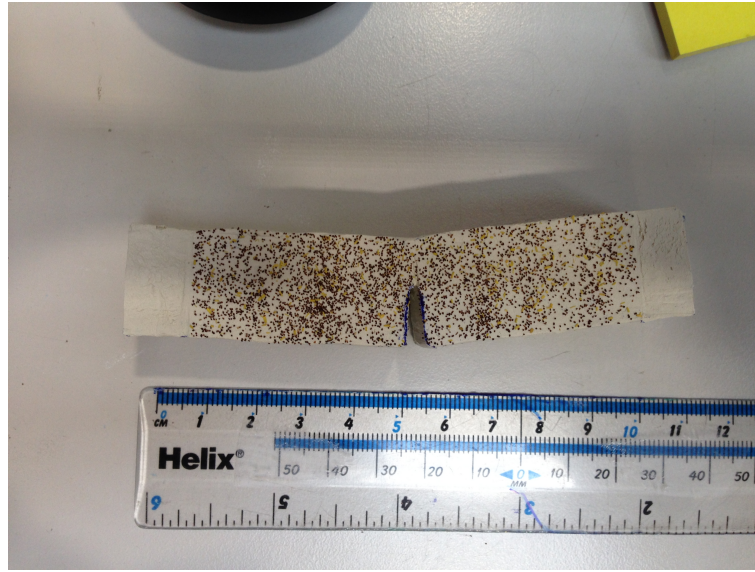


Figure 3.13: Modeling flock on a kaolin clay beam

sity and brightness. The intensity and brightness were enhanced using the default settings of the Matlab Image Processing Toolbox. The precision increase can be seen in Figure 3.16.

The second factor that affects PIV is represented by the camera lens distortion. Images taken by the camera suffer from the fish eye effect due to the curvature of the lens. Pixels at the edges of the photos or close to the corners resulted deformed and not squared. Only the pixels in the centre of the field of view kept their squared shape. And so, photos were focused in a manner in order to have the main sample feature (the crack) in the centre of the field of view. The placement of the crack in the center of the photo was also proved by measuring the pixels which corresponded to the crack location. The crack was placed in the centre of the photo and close to the point of intersection of the two diagonals.

### 3.7 Visual analysis

Clay beams were also analysed on the computer screen to detect the crack propagation. The analysis ‘by eye’ on the screen allowed the determination of various parameters regarding the cracking process. Using software such as AutoCAD or CorelDraw, it was possible to measure different lengths in pixels. The lengths so

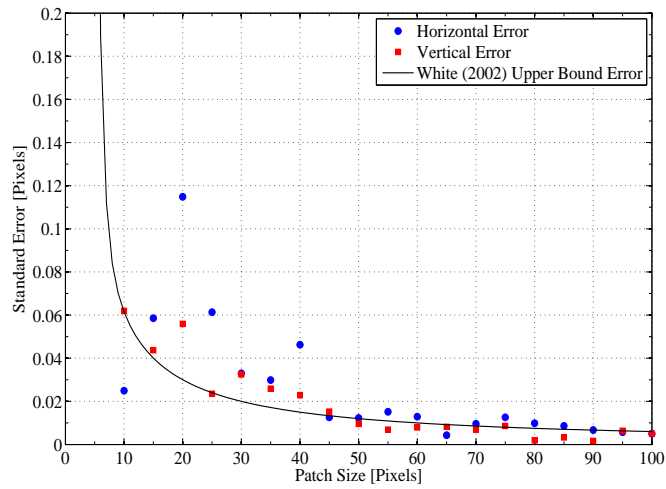


Figure 3.14: Standard deviation calculated on the original images captured during the tests

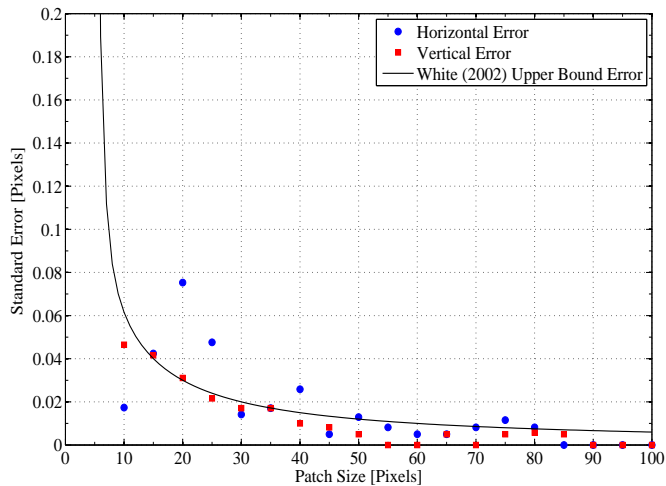


Figure 3.15: Standard deviation calculated on the greyscale images captured during the tests

measured were then converted into geometrical measurements.

In the case of bending tests, the conversion between the lengths measured in pixels and those expressed in millimetres was done using the known length between the bottom rollers of the bending support. For construction, that distance was equal to 80 mm. So, the interpolation between this known distance and the length measured in pixels allowed the determination of the length in millimetres.

This method is similar to that used in GeoPIV in which the displacements measured

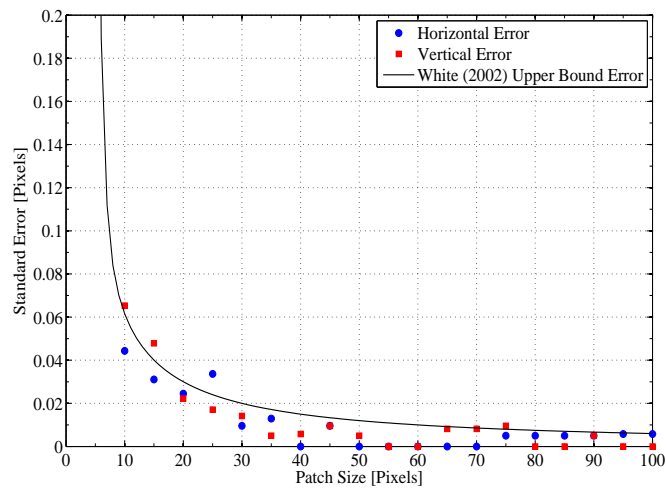


Figure 3.16: Standard deviation calculated on the enhanced grayscale images

in pixel space are converted into measurements in the geometry space interpolating the known distance between the control points.

### 3.8 Test limitations

Despite the simplicity of the tests, a series of limitations should be taken into account. For that, the results should be considered affected by some random errors that cannot be measured. These errors are divided into different categories and explained in turn.

#### Errors related to the geometry

- Sample preparation:

All the samples were manually cut using moulds and a wire cutter, so every specimen was slightly different. In addition, the clays used were soft and difficult to cut without squeezing the samples.

In the direct tensile test the main difference between the beams was related to the width of the central section. This part was cut removing the soil first from one side and then from the other. It was challenging to obtain all the specimens with a width of exactly 5 mm. In some cases, the width was not

the same in the front and back of the samples. Some examples of different geometries in the central section are reported in Table 3.3.

In the 3-point bending beams not perfectly squared were prepared. Due to the softness of the clay, the removal of the mould from one side of the beams caused a variation in geometry. Beams were not perfectly squared in their cross-sectional area. For example, LC0d\_0116\_b5 had dimensions  $18 \times 20 \times 99.5$  mm.

Test	Central section dimensions (mm)	
	Front	Back
LC_060616_b4	4.93	4.39
K_080316_b1	5.21	5.43
K_210316_b3	5.28	6.35

Table 3.3: Geometry differences measured in the central section of the samples used in the direct tensile tests

- Drying:

When a clay is left to dry, it changes its dimensions. The loss of water caused shrinkage and specimens varied their original dimensions. Table 3.4 reports some examples of beam geometries before and after the drying process in the oven.

### Errors related to the loading frame

- Incorrect position of the bottom rollers:

In the 3-point bending tests the bottom rollers were supposed to be at the same distance on the left and the right side of the specimen. Due to the variation in geometry the distance between the middle notch to the left support was different from the distance on the right, and vice versa. This caused a mixed mode crack which was characterised by inclined faces (Figure 3.17).

- Top roller not perpendicular to the beam length:

In the 3-point bending tests the top roller was manually placed perpendicularly

Test	Beam dimensions (mm)	
	Original	90' drying
LC0d_0116_b2	20×20×99.5	19×19×94
LC0d_0116_b6	(18 – 20)×20×99.5	18×19×94
LC0d_0116_b4	20×20×100	19×19×96
LC0d_0116_b8	(19 – 21)×20×99.5	19.5×19×94
LC0d_0116_b3	20×20×99.5	19×19.5×94
LC0d_0116_b9	(19.5 – 20)×20×100	20×19×96

Table 3.4: Variations in the beam geometry caused by the oven drying

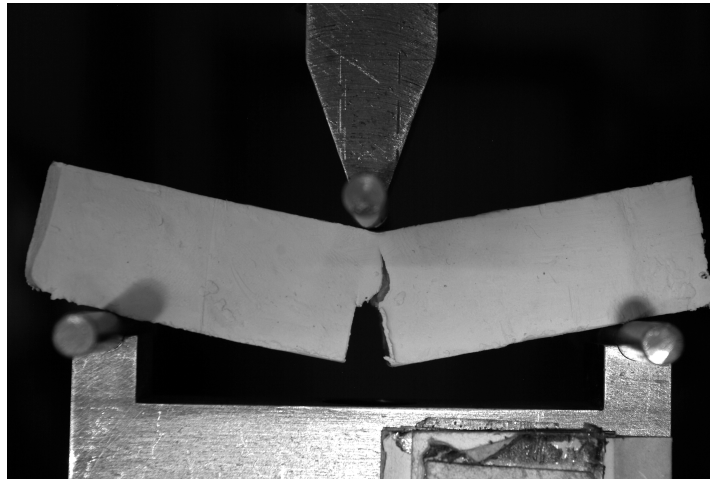


Figure 3.17: K0d\_2403\_b1 not centred on the bending support and development of a mixed mode crack

to the length of the specimen. However, test results showed that sometimes the roller was initially inclined with respect to the midsection. A bad alignment of the top roller caused its movement towards the corrected position during the test or a bad performed test due to the eccentricity of the load applied. The top roller misplacement was recorded by the load cell which showed a jump in the load diagram when the top roller moved to the right alignment. Similar tests were discarded from the analysis.

- Extra deformation of the beam:

In in the 3-point bending tests, the displacements recorded resulted affected by the time in which the beam was left on the supports. The clay beams standing on the supports deformed under their own weight with time (no load applied). This phenomenon was seen especially during the tests of wet beams. Examples of the displacements supported by the beams before the load application are reported in Table 3.5.

Test	Displacement at 0 N load (mm)
K0d_0916_b6	0.50
LC0d_0116_b10	0.48
DC0d_1115_b7	0.71

Table 3.5: Displacements supported by the beams before the load was applied

- Tensile test gluing process:

The glue did not allow to have a specimen with the central part completely parallel to the direction of the force. Some specimens underwent twists and rotations, bending or inclinations of the central section. All these factors affected the tensile behaviour of the kaolin and London clays decreasing the maximum stress that the samples sustained. Durham clay was less affected by this type of error because the central section of the specimen was larger than that adopted for the other two clays. The samples with the central part that was very deflected from the vertical axis were discarded.

### Errors related to the camera and PIV measurement

- Confined place for the camera placement:

The loading rig used in the Heavy Structures Lab had only a confined space in front of it and the placement of the camera was difficult. Images were often taken with the camera too far from the samples in order to have a good resolution with the lenses owned by the department. This affected the PIV analysis as less pixels were involved in the process of displacements tracking.

The sample occupied a small central part of the photo while the surrounding area was occupied by black background pixels.

- PIV ‘built-in’ error:

The PIV is an efficient tool to analyse the displacement/strain fields but it is based on the analysis of photos which represent only the surface of the tested beams. For that, it was assumed that the beams behaved in a similar manner to that of the surface also along the width. However, the tensile behaviour inside the beams could have been completely different.



## Chapter 4

# Direct tensile test results

The chapter describes the results found in direct tensile tests. Clay samples were pulled apart applying a tensile force until a crack formed in the centre.

At first, the load-displacement graphs are presented for the three clays studied. The data recorded showed a nonlinear behaviour. However, the response of the clays moved towards a linear behaviour with drier samples. Values of tensile strength were then calculated and plotted against the moisture contents to verify if the trends found in the literature were also followed by the three clays adopted in the study. Then the initial Young's modulus and the yield strength were calculated and related to the moisture content. Finally, the tensile strengths were plotted in relation to the plasticity index.

### 4.1 Test results

As reported in Section 3.2, the test was modified from the standards used for metals and adopted to study the tensile behaviour of clays. Specimens with the geometry shown in Figure 4.1(a) were glued to the loading rig and loaded in tension until a crack developed in the central section (Figure 4.1(b)).

Typical results are shown in Figure 4.2 for Speswhite kaolin, London and Durham clays. For a clearer understanding, the load-displacement curves were reported without error bars. The error was determined by loading the load cell with weights as explained in Section 3.5. The error bar for small loads was too large and completely

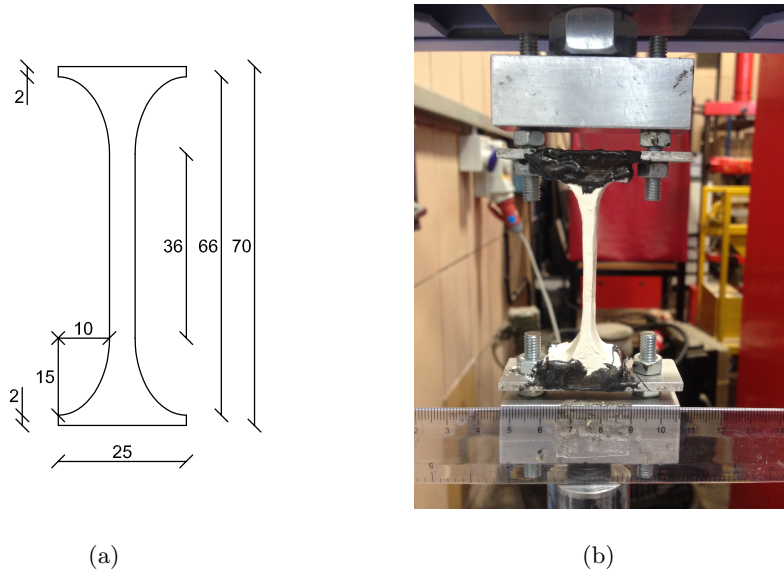


Figure 4.1: Specimen geometry and setup of the direct tensile test (dimensions in mm)

covered the tensile load curve.

From the load-displacement curves it is possible to notice that the force sustained by the specimens increased monotonically until a maximum value was reached. Once the maximum value was passed, the force suddenly dropped to zero because the sample underwent cracking. An example of an intact and cracked specimen is shown in Figures 4.3.a) and 4.3.b) respectively.

For a comprehensive understanding of the tensile behaviour the three clays were tested at various moisture contents (Table 4.1). The number of samples studied for each moisture content is reported in Table 4.2.

The moisture content ranges studied for the three clays was:

- Speswhite kaolin:  $\omega = 15.3 - 41.7 \%$  ( $\omega/\omega_{OMC,K} = 0.45 - 1.23$ )
- Durham clay:  $\omega = 13.6 - 40.6 \%$  ( $\omega/\omega_{OMC,DC} = 0.88 - 2.62$ )
- London clay:  $\omega = 8.8 - 29.5 \%$  ( $\omega/\omega_{OMC,LC} = 0.36 - 1.20$ ).

The subscript ‘*K*’ means kaolin clay, ‘*DC*’ Durham clay and ‘*LC*’ London clay.

The range of moisture contents studied was similar to those adopted in literature for the direct tensile tests:

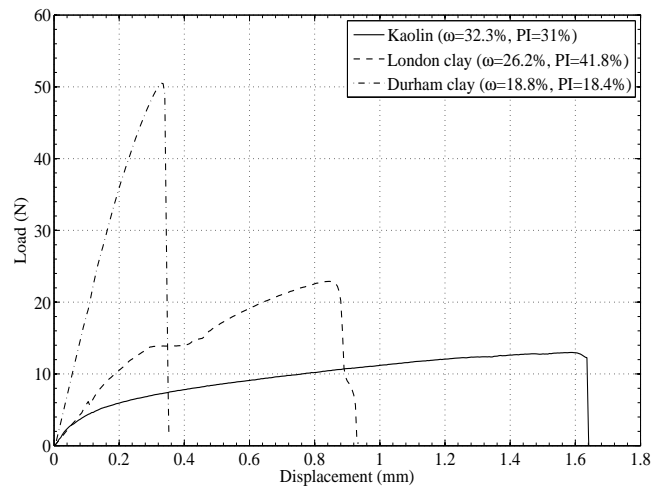


Figure 4.2: Typical tensile load-displacement curves for Speswhite kaolin, London and Durham clay samples

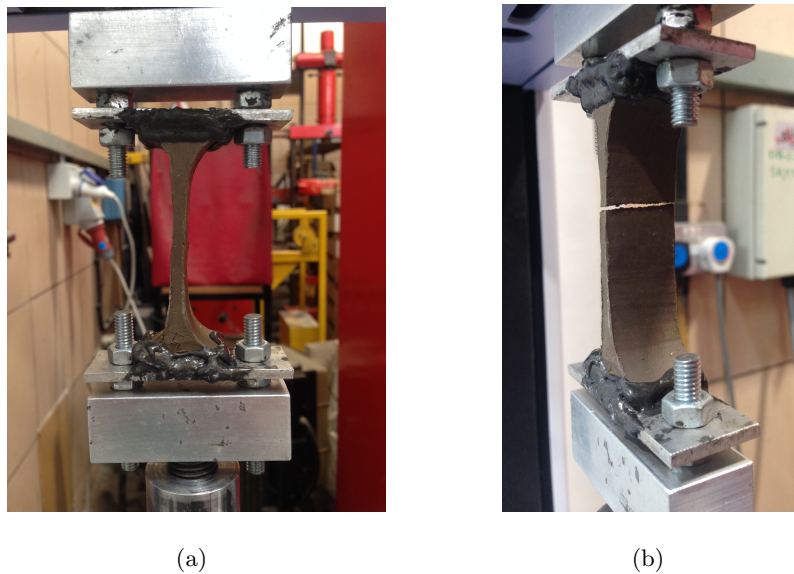


Figure 4.3: Example of London clay sample used in the direct tensile test: (a) at the end of the setup before the beginning of the test, (b) cracked at the end of the test

- Ajaz and Parry (1975): Gault clay  $\omega/\omega_{OMC} = 0.79 - 1.09$ , Balderhead clay  $\omega/\omega_{OMC} = 0.76 - 1.35$
- Lakshmikantha et al. (2008): Barcelona silty clay  $\omega/\omega_{OMC} = 0.89 - 2.19$
- Tang et al. (2015): clayey soil  $\omega/\omega_{OMC} = 0.55 - 1.64$

Clay	$LL$	$PL$	$\omega_{min}$	$\omega_{max}$	$\Delta\omega$	$\omega_{OMC}$
Kaolin	65	34	15.3	41.7	26.4	34.0
Durham clay	41.7	23.3	13.6	40.6	27.0	15.5
London clay	75.3	33.5	8.8	29.5	20.7	24.5

Table 4.1: Summary of the moisture contents studied in the tensile tests.  $\Delta\omega = \omega_{max} - \omega_{min}$ 

Soil	$\omega_{OMC}$ (%)	$PI$ (%)	$\omega$ (%)								
			<b>8 - 12</b>	<b>12 - 16</b>	<b>16 - 20</b>	<b>20 - 24</b>	<b>24 - 28</b>	<b>28 - 32</b>	<b>32 - 36</b>	<b>36 - 40</b>	<b>&gt;40</b>
Kaolin	34	31	0	1	0	2	0	6	2	1	1
London clay	24.5	41.8	1	0	0	1	7	0	0	0	0
Durham clay	15.5	18.4	0	2	2	5	2	0	0	0	1

Table 4.2: Number of tensile tests performed for different moisture contents

- Zeh and Witt (2007): Plessa clay  $\omega/\omega_{OMC} = 0.25 - 1.27$
- Stirling et al. (2015): glacial till  $\omega/\omega_{OMC} = 0.13 - 1.53$

The moisture contents found in literature were usually smaller than two times the optimum moisture content, except in the case of Lakshmikantha et al. (2008). For the Durham clay, a specimen with a moisture content equal to twice the moisture content was tested. But it was used to validate the wet behaviour of the soil. The majority of the wet tests were performed with an average moisture content of  $\omega = 24.7\%$  ( $\omega/\omega_{OMC} = 1.59$ ), which was in agreement with the maximum moisture content found in literature.

When the moisture content was high, beams underwent large displacements. At the beginning of the tests where the force was directly proportional to the displacement, which meant a linear-elastic behaviour. After that, the bend in the loading curve determined the passage to a plastic behaviour which was followed until the maxi-

mum force was reached. Then, the forces dropped to zero representing the complete failure of the specimens due to crack propagation (Figure 4.2).

The sample response moved towards a brittle behaviour with reducing moisture content. The linear-elastic straight line increased while the plastic displacement became smaller. In addition, the strain required to obtain failure diminished. The response of the clays under tension loading was related to the moisture content.

Some of the samples tested using Speswhite kaolin, Durham and London clays presented a peculiar force-displacement graph (Figure 4.4). After an almost linear initial part, the force reached a constant value and the displacements continued to increase. This behaviour was captured in all the three clays. For kaolin beams the force plateau appeared in specimens having a moisture content in the range 29-30 %, 23-25 % for London clay beams and 13-16 % for the Durham clay. From these data, it seemed that the force plateau was reached for specimens with a moisture content approximately equal to the optimum moisture content. This behaviour was considered an error given by the equipment. A damage to the glue used to connect the samples to the aluminum plates could be the cause of the load curve plateau. However, a possible partial detachment of the sample from the aluminum plate was impossible to see because the specimen's base was covered by the glue. The load anomaly was corrected eliminating the load plateau and connecting the two parts of the curve which had the same slope.

## 4.2 Tensile strength calculation

Nominal stress-nominal strain graphs were used for simplicity because they do not count the variation of the specimens dimensions during the tests. These parameters were calculated dividing the tensile force  $P$ , by the initial cross-sectional area  $A_0$  and dividing the elongation,  $\Delta l$ , by the original length  $l_0$  of the specimen respectively (Equations 4.1-4.2 ).

$$\sigma_n = \frac{P}{A_0} \quad (4.1)$$

$$\varepsilon_n = \frac{\Delta l}{l_0} \quad (4.2)$$

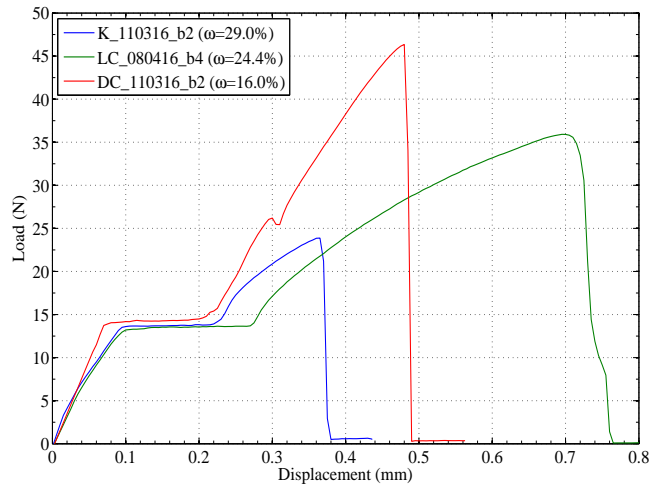


Figure 4.4: Tensile force plateau for Speswhite kaolin, London and Durham clay samples

The new curves are plotted in Figures 4.5, 4.6, 4.7. Due to the capillary forces the tensile strength depends on the suction within to the clay samples. Soil suction is then related to the moisture content (or degree of saturation) through the Soil Water Retention Curve (SWRC). However, in this analysis results were chosen to be expressed in terms of moisture contents. Thus, suction was not directly considered. The tensile strength  $\sigma_t$  was defined as the highest nominal stress that the specimen supported before reaching failure and was calculated from the stress-strain graph.

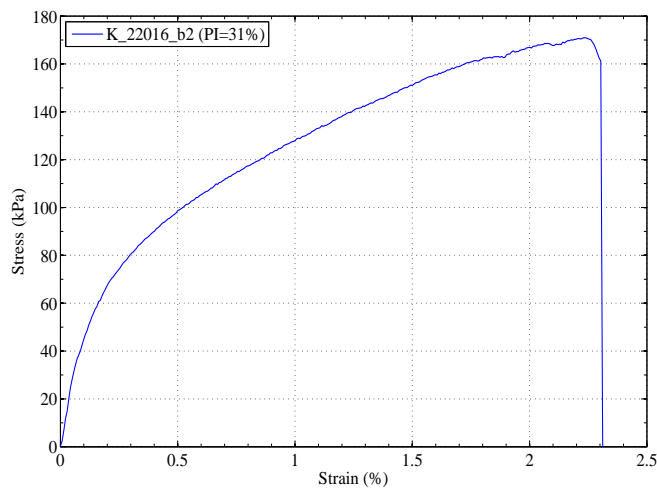


Figure 4.5: Stress-strain graph for a Speswhite kaolin sample at  $\omega = 32.3\%$

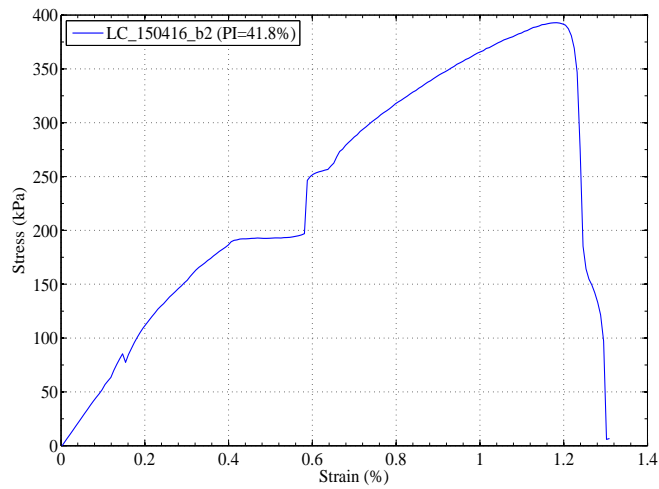


Figure 4.6: Stress-strain graph for a London clay sample at  $\omega = 26.2\%$

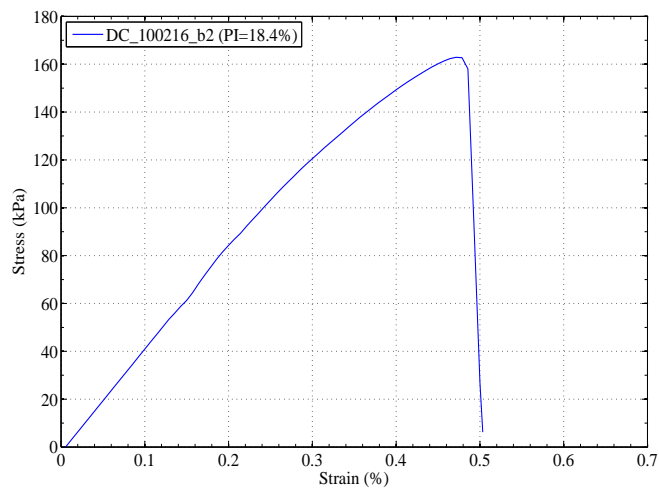


Figure 4.7: Stress-strain graph for a Durham clay sample at  $\omega = 18.8\%$

Tables B.1, B.2, B.3 in Appendix B report the tensile strengths found for all the specimens analysed. A summary of the results is reported in Table 4.3.

### 4.3 Results discussion

An important role was played by the moisture content at which the clays were tested: variations in moisture content determined different tensile responses.

Clay	Tensile strength $\sigma_t$ (kPa)		Moisture content $\omega$ (%) for this $\sigma_t$	Strain at max stress (%) for this $\sigma_t$
	$\sigma_{t,max}$	$\sigma_{t,min}$		
Kaolin	$\sigma_{t,max}$	341.9	23.5	0.9
	$\sigma_{t,min}$	15.9	41.7	5.0
Durham clay	$\sigma_{t,max}$	190.6	14.0	0.7
	$\sigma_{t,min}$	9.9	24.1	1.1
London clay	$\sigma_{t,max}$	618.8	22.3	1.0
	$\sigma_{t,min}$	55.5	29.5	0.8

Table 4.3: Summary of the direct tensile test results

### 4.3.1 Kaolin

The values of the tensile strength for kaolin specimens covered a moisture content range from 15 % to 42 % ( $\omega/\omega_{OMC,K} = 0.44 - 1.24$ ,  $\omega_{OMC,K} = 34$  %). In these limits, tensile strengths varied in a nonlinear manner (Figure 4.8). The point of maximum strength was seen at the dry side of the OMC for a moisture content of 24 % ( $\omega/\omega_{OMC,K} = 0.71$ ). Moving towards the dry side, the tensile strength diminished till reaching a minimum value of 141.4 kPa for a moisture content equal to 15.3 % ( $\omega/\omega_{OMC,K} = 0.45$ ). A similar reduction was also seen by increasing the moisture content in the soil mass. For wet samples the tensile strength decreased, reaching a minimum value of 15.9 kPa at a moisture content of 41.7 % ( $\omega/\omega_{OMC,K} = 1.23$ ).

The relationship between the tensile strength and the moisture content showed a decreasing tendency moving towards the dry side. A similar behaviour was caught by Lakshmikantha et al. (2008) and Tang et al. (2015) in their tests (Figure 4.9). In their results, the tensile strength followed a bell-shaped curve with the variation of moisture content. The values found in Speswhite kaolin were higher than those found in literature. This difference is explained by the presence of coarser soil particles. The soil tested by Lakshmikantha et al. (2008) was a silty clay while the soil tested by Tang et al. (2015) was composed by silt (76 %) and clay (22 %).

The strain recorded at the moment of maximum strength showed a different be-

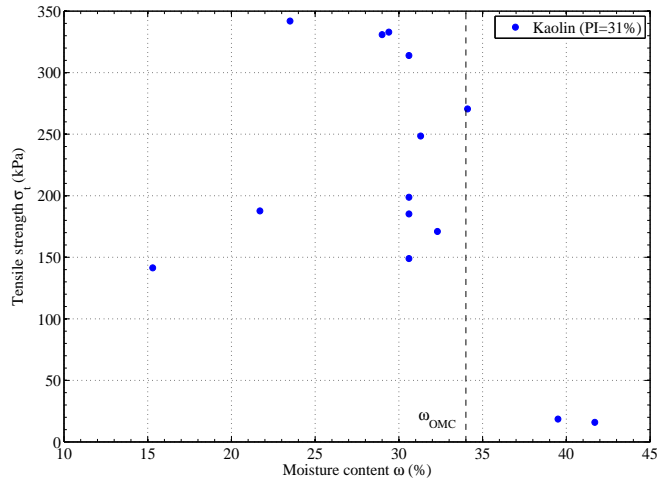


Figure 4.8: Tensile strength variation in kaolin samples related to the moisture content

haviour and followed the same tendency seen for the displacements. For dry samples the tensile strength was reached at very small values of strain. With the increase of the moisture content, the strain increased monotonically. From the data, the strain seemed to increase in a steeper manner once the moisture content of 30.0 % ( $\omega/\omega_{OMC,K} = 0.88$ ) was passed (Figure 4.10).

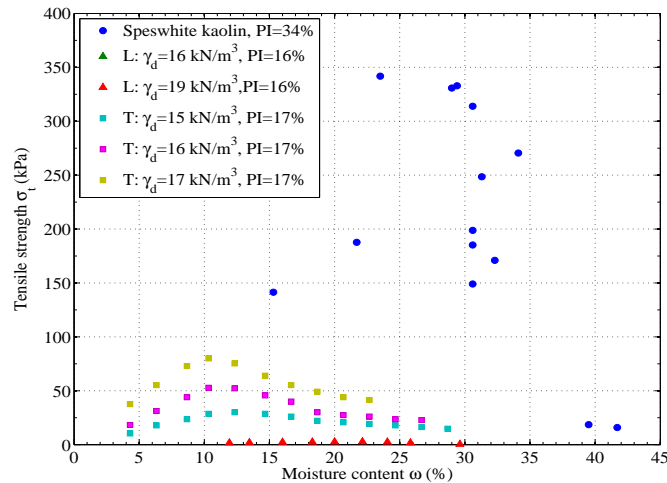


Figure 4.9: Tensile strength comparison between the Speswhite kaolin and the literature results taken from Lakshmikantha et al. (2008) (symbol L in the legend), Tang et al. (2015) (symbol T in the legend)

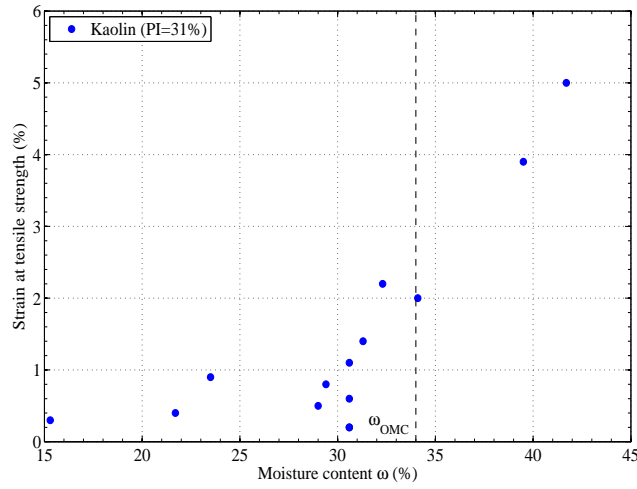


Figure 4.10: Strain variation in kaolin samples related to the moisture content

### 4.3.2 Durham clay

A nonlinear trend was also followed by the data collected from the tensile tests performed on the Durham clay (Figure 4.11). In this case, a maximum strength of 190.6 kPa was recorded at a moisture content of 14.0 % ( $\omega/\omega_{OMC,DC} = 0.90$ ). Similarly to the kaolin beams, the maximum tensile strength corresponded to a moisture content slightly smaller than the OMC ( $\omega_{OMC,DC} = 15.5$  % for Durham clay). However, even if the tensile strength peak was assumed to be recorded at 190.6 kPa, very dry samples could not be tested as they were too fragile and they were often damaged during the installation on the loading rig. On the other side, increasing the amount of water the tensile strength values were decreasing to a minimum of 13.2 kPa at 40.6 % ( $\omega/\omega_{OMC,DC} = 2.62$ ) with a steep drop in magnitude for a moisture content higher than 20.0 % ( $\omega/\omega_{OMC,DC} = 1.29$ ).

The strain did not follow an increasing trend (Figure 4.12). It showed a peak at  $\omega = 23.8$  % ( $\omega/\omega_{OMC,DC} = 1.54$ ) and then decreased to 0.4 % in wetter beams ( $\omega = 26.9$  %,  $\omega/\omega_{OMC,DC} = 1.74$ ).

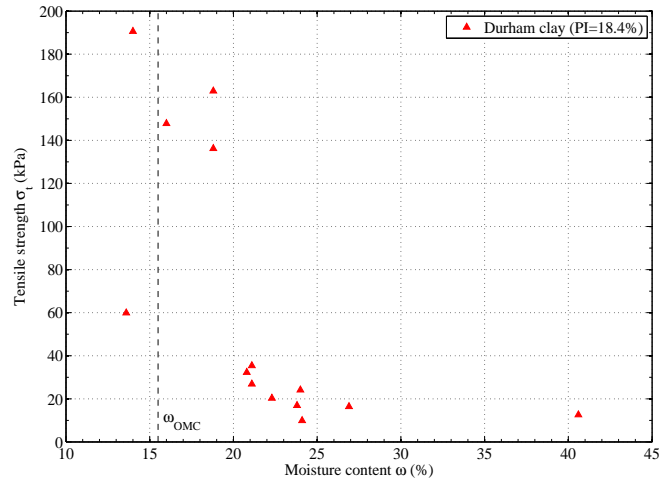


Figure 4.11: Tensile strength variation in Durham clay samples related to the moisture content

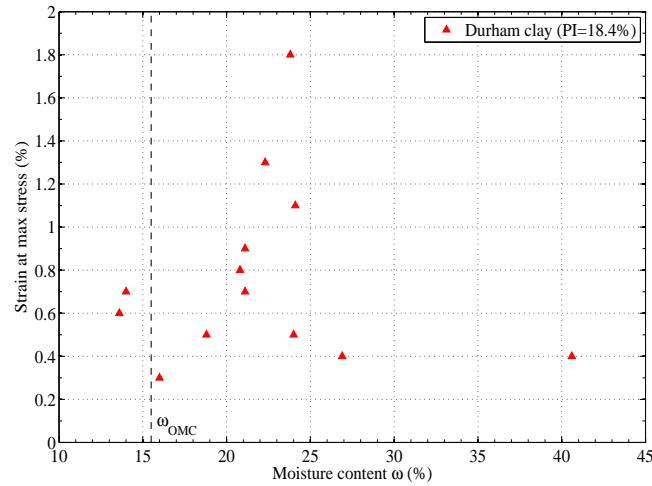


Figure 4.12: Strain variation in Durham clay samples related to the moisture content

### 4.3.3 London clay

Similarly to the kaolin behaviour, the London clay tensile strength followed a nonlinear trend (Figure 4.13). The maximum tensile strength could be seen for a moisture content equal to 22.3 % ( $\omega/\omega_{OMC,LC} = 0.91$ ) and it was equal to 618.8 kPa. This maximum strength was recorded for values of moisture contents equal to the optimum moisture content ( $\omega_{OMC,LC} = 24.5$  %). The high value of tensile strength is related to the stiffness and strength of the London clay. Higher values of yield

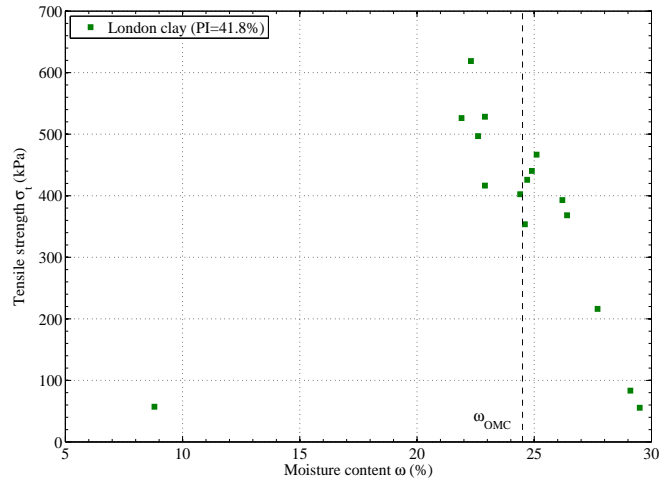


Figure 4.13: Tensile strength variation in London clay samples related to the moisture content

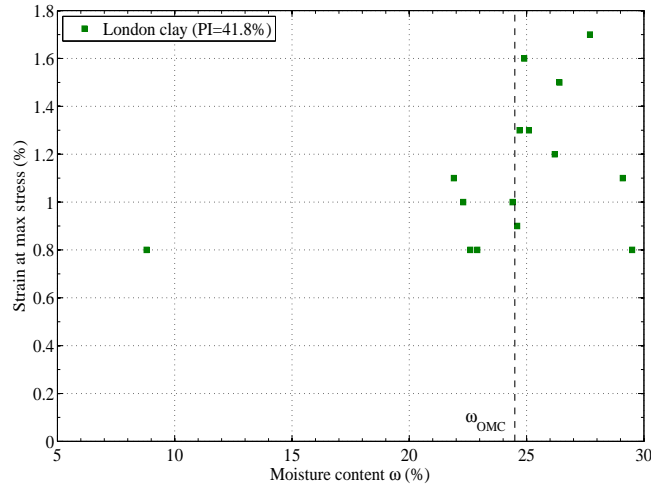


Figure 4.14: Strain variation in London clay samples related to the moisture content

strength and tensile strength were recorded during the London clay tests. The stiffness also determined an increase of the force needed to crack the samples.

Also the strain corresponding to the tensile strength followed a similar behaviour to that of kaolin increasing from dry to wet samples (Figure 4.14). However the results were scattered and did not suggest any approximate trend.

#### 4.3.4 Discussion

Comparing the results between the three types of clays it is clear that the London clay developed the highest tensile strength, which exceeded 600 kPa for a strain equal to 1.0 % (Figure 4.15-4.16). Such a high value was explained by the fact that London clay was a stiffer clay compared to the other two. Instead the lowest value of maximum strength was recorded for the Durham clay ( $\approx 200$  kPa). This difference in magnitude was linked to the plasticity index of the clays studied. London clay presented the highest  $PI$ , so it was able to deform more and sustain more load before reaching the rupture point for crack formation. On the other hand, the Durham clay had a percentage of sand and silt in its mass which affected the plasticity index and consequently the results.

Figures 4.8, 4.11, 4.13 show that values of tensile strengths followed a nonlinear curve. Considering only the values falling on the right side of the curve, an exponential line was used to approximate the data. The left side of the nonlinear curve was neglected because just a couple of samples were studied on the dry side. More data were required to find an approximate curve that fit the data.

The tensile strength was calculated for every value of moisture content falling on the right side of the strength (Figure 4.17). In the case of kaolin, the peak tensile

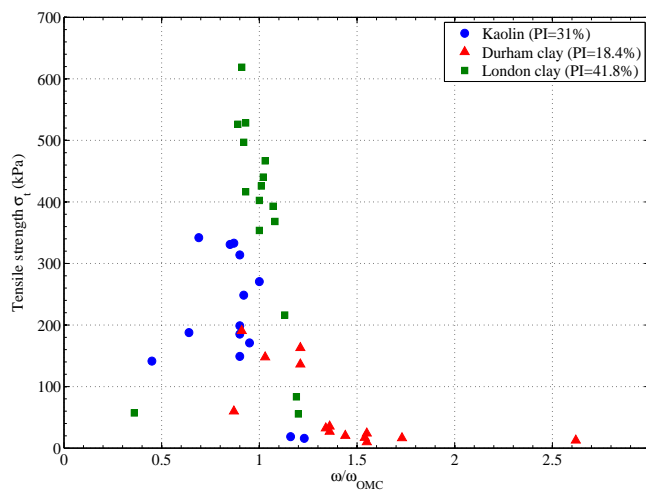


Figure 4.15: Relationship between the tensile strength and moisture content for the samples prepared with the three different clays

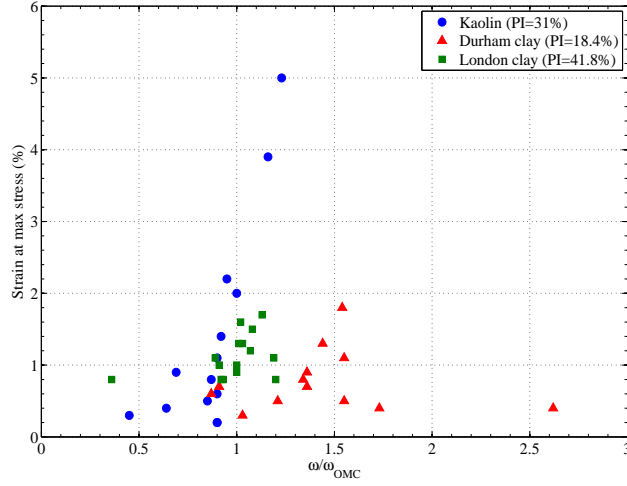


Figure 4.16: Relationship between the strain at the tensile strength and moisture content for the samples prepared with the three different clays

strength was measured at  $\omega = 23.5\%$  ( $\omega/\omega_{OMC,K} = 0.69$ ), while the Durham clay had a maximum tensile strength at  $\omega = 14\%$  ( $\omega/\omega_{OMC,DC} = 0.90$ ) and the London clay at  $\omega = 22.3\%$  ( $\omega/\omega_{OMC,LC} = 0.91$ ). The equations of the fitted curves are reported in Table 4.4.

Similar approximations were found also in literature. Farrell et al. (1967), Trabelsi

Clay	$\omega_{\sigma_t, max}$ (%)	Exponential curve equation	$R^2$
Kaolin	23.5	$\sigma_t = 817.48 \times 10^3 e^{-0.26\omega}$	0.90
Durham clay	14.0	$\sigma_t = 537.46 e^{-0.12\omega}$	0.52
London clay	22.3	$\sigma_t = 281.74 \times 10^3 e^{-0.27\omega}$	0.78
Glacial till (Stirling et al., 2015)	-	$\sigma_t = 484.07 e^{-0.14\omega}$	0.90
Natural deposit (Trabelsi et al., 2012)	-	$\sigma_t = 148.65 e^{-0.06\omega}$	0.98
Loam (Farrell et al., 1967)	-	$\sigma_t = 248.03 e^{-0.227\omega}$	0.99

Table 4.4: Approximation parameters for tensile strength values

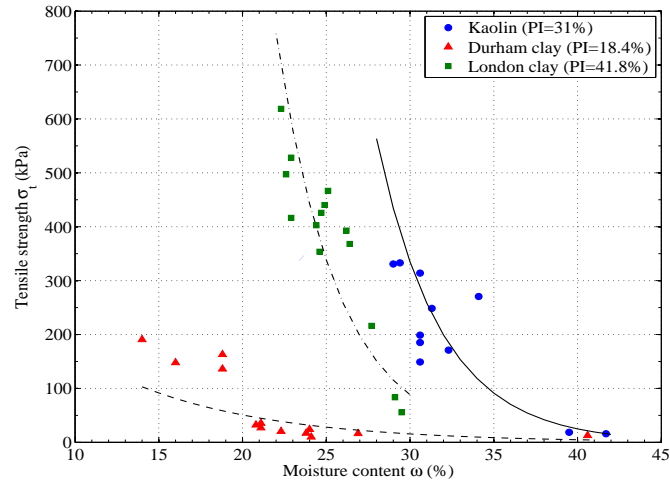


Figure 4.17: Kaolin, Durham and London clay approximation of the tensile strength

et al. (2012) and Stirling et al. (2015) used an exponential fitting curve to approximate their results, as shown in Figure 4.18. Despite the similar behaviour of the results found in this investigation and the results found in the literature, no correlations between the various clayey soils and the tensile strength curves is shown in the graph. The majority of the exponential lines had a steep slope. A small decrease of moisture content determines a large reduction of tensile strength. Durham clay and the natural deposit tested by Trabelsi et al. (2012) had gentler slope in comparison to the other results.

Lakshmikantha et al. (2008), Wang et al. (2007b) and Tang et al. (2015) also showed that there was a relationship between the tensile strength and the dry density at which the clays were compacted (i.e. Figure 2.27(c)). In these tests, clay soils were consolidated instead of being compacted. And therefore, fewer flaws were expected in the clay specimens compared to those prepared by compaction. Higher results of tensile strength were expected in comparison to those obtained for compacted clays. Due to the sample preparation technique, diverse dry densities were not considered. The data collected from the tests also allowed the calculation of the variation in the tensile strength values. For every type of clay used, two or more tests were carried out on soils having the same moisture content. Those tests allowed the assessment of the variation in the results as reported in Table 4.5.

Four of the kaolin samples used in the tests had a moisture content equal to 30.6 %, but the tensile strengths were different in all four cases. The variation between the maximum and the minimum values was equal to 165 kPa. Such a high variation was caused by the direct tensile test setup and the soil flaws which determined the location of the fractured section. A similar high difference was recorded also for the strain, with a variation of 0.9 % in magnitude. Despite the high difference, the values of the four tensile strengths have been considered in the following analysis because data were studied as a family and not in relation to a single moisture content.

Similar observations were also done for the London clay and the Durham clay. The London clay tests showed two samples at approximately the same moisture content of 24.7 %. Although they have the same amount of water, the tensile strengths varied by 72 kPa and the strain by 0.4 %. The Durham clay had two samples with  $\omega = 18.8$  % and two with similar moisture contents  $\omega = 24.1$  %. They both had diverse tensile strengths with a respective variation of 27 kPa and 14 kPa, while the strain values were equal in the first two and varied by 0.6 % in the second two. The Durham clay had the lowest plasticity index and for that it showed less variability in the results compared to the other two clays.

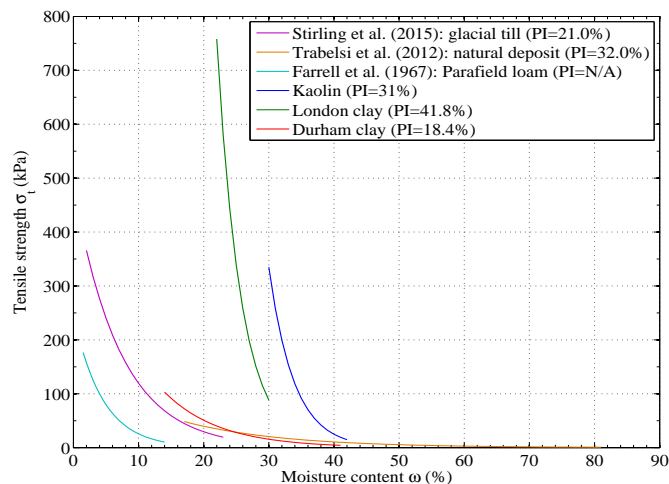


Figure 4.18: Comparison between the exponential trendline found for kaolin, London, Durham clay and the trendline found in literature. The equations of the approximated lines are reported in Table 4.4

In conclusion, the table shows that this direct tensile test setup provided a poor test repeatability, as shown by the kaolin clay results.

Clay	No.	$\omega$ (%)	$\sigma_{t,min}$ (kPa)	$\sigma_{t,max}$ (kPa)	$\sigma_{t,mean}$ (kPa)	$\Delta\sigma/\sigma_{t,mean}$ (%)
Kaolin	4	30.6	149.0	313.9	211.7	78
Durham clay	2	18.8	136.2	162.9	149.6	18
	2	24.1	9.9	24.1	17.0	80
London clay	2	24.7	353.7	425.9	389.9	19
Clay	No.	$\omega$ (%)	$\varepsilon_{min}$ (%)	$\varepsilon_{max}$ (%)	$\varepsilon_{mean}$ (%)	$\Delta\varepsilon/\varepsilon_{mean}$ (%)
Kaolin	4	30.6	0.2	1.1	0.5	1.8
Durham clay	2	18.8	0.5	0.5	0.5	0
	2	24.1	0.5	1.1	0.8	0.8
London clay	2	24.7	0.9	1.3	1.1	0.4

Table 4.5: Variation of the tensile strength in specimens with the same moisture content

$$\Delta\sigma = \sigma_{t,max} - \sigma_{t,min}, \Delta\varepsilon = \varepsilon_{max} - \varepsilon_{min}$$

#### 4.3.5 Yield strength and initial Young's modulus

The tensile test data collected from the tests on the three clays also allowed the calculation of the yield stress  $\sigma_{YS}$  and the initial Young's modulus  $E_0$ . The latter was defined as the slope of the initial elastic part of the curve, where Hooke's law could be assumed. As seen for the values of the tensile strength, these two parameters were affected by the moisture content. Tables B.4, B.5, B.6 in Appendix B report  $E_0$  and  $\sigma_{YS}$  while Figures 4.19 and 4.20 show the relationship with the moisture content.

The data in Figure 4.19 show that London clay has the highest yield stress for the same moisture content than the other two clays. E.g. for  $\omega = \omega_{OMC}$ , the London clay has a  $\sigma_{YS}$  approximately equal to 125 kPa, while kaolin has a  $\sigma_{YS} \approx 30$  kPa

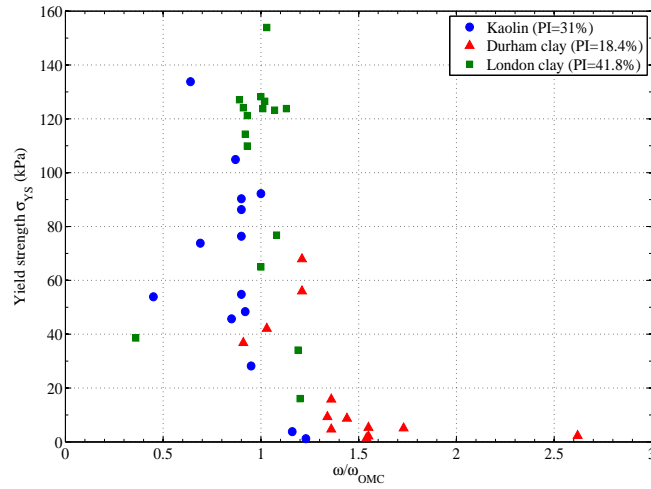


Figure 4.19: Relationship between the tensile yield strength  $\sigma_{Y_S}$  and moisture content for the specimens prepared with the three different clays

Clay	$\omega_{\sigma_t, max}$ (%)	Exponential curve equation	$R^2$
Kaolin	23.5	$\sigma_{Y_S} = 116.82 \times 10^4 e^{-0.32\omega}$	0.84

Table 4.6: Approximation parameters for yield strength values

and Durham clay a  $\sigma_{Y_S}$  equal to approximately 40 kPa.

Similarly to the trend line of tensile strength results, approximations of the yield stress and the initial Young's modulus were calculated for the data falling on the wet side of the peak value (or critical moisture content  $\omega_c$ ). The dry side was neglected for the lack of results.

In this case the Durham clay data and the London clay yield strength were not well approximated by a power law regression line. Thus, the fitting curve was calculated only for the results found in kaolin and for the London clay's Young's modulus. Figures 4.21-4.22 and Tables 4.6-4.7 report the approximation curve equation and the  $R^2$  value.

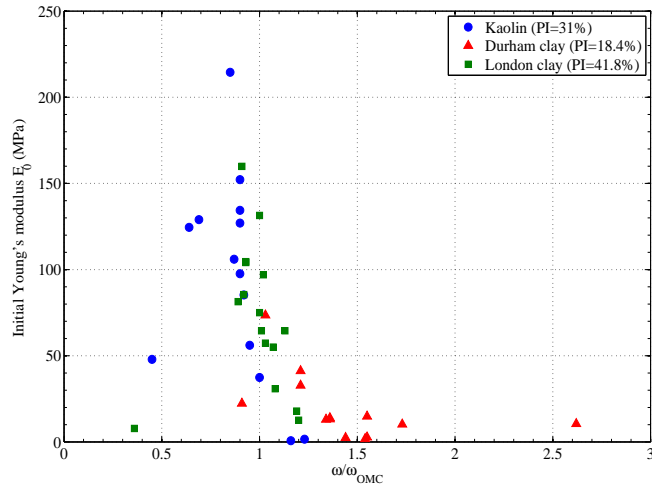


Figure 4.20: Relationship between the Young's modulus  $E_0$  and moisture content for the specimens prepared with the three different clays

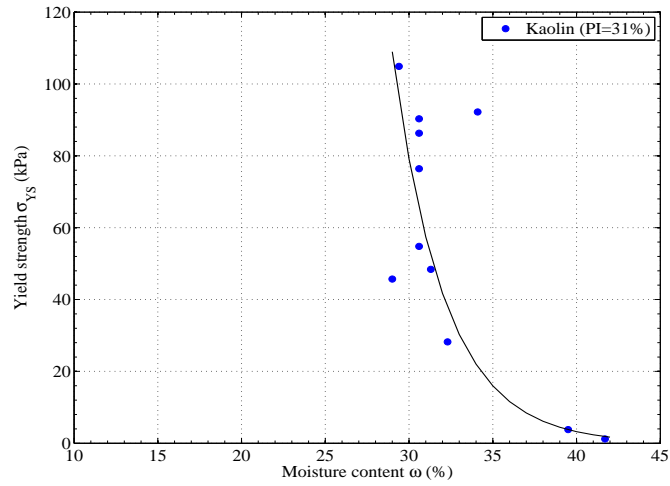


Figure 4.21: Approximation of the kaolin yield strength

Clay	$\omega_{\sigma_t, max}$ (%)	Exponential curve equation	$R^2$
Kaolin	23.5	$E_0 = 865.88 \times 10^5 e^{-0.44\omega}$	0.93
London clay	22.3	$E_0 = 710.53 e^{-0.27\omega}$	0.77

Table 4.7: Approximation parameters for initial Young's module values

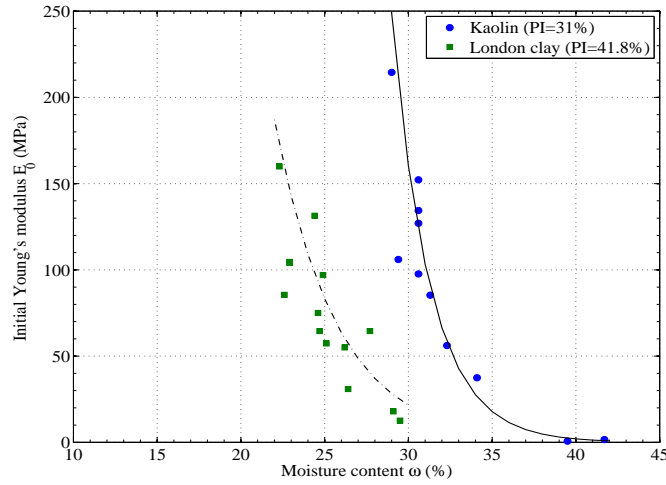


Figure 4.22: Approximation of the kaolin and London clay initial Young's modulus

#### 4.3.6 Plasticity index

The tensile strength  $\sigma_t$  could also be related to the plasticity index  $PI$  of the clays used. Figure 4.23 shows the relationship between the  $PI$  and the  $\sigma_t$  for the three clays and selected values of tensile strengths found in literature by Ajaz and Parry (1975), Lakshmikantha et al. (2008) and Tang et al. (2015) for tensile tests on hour-glass samples. In the graph, two different values of the tensile strength were plotted, the peak tensile strength  $\sigma_{t,peak}$  and the tensile strength calculated at the optimum moisture content  $\omega_{OMC}$ . From the plot it is possible to see that in both cases the magnitude of the maximum strength sustained by the clay beams increased with the increase of the plasticity index. Reducing the plasticity index the tensile strength decreased following a linear relationship until the value of  $PI = 16\%$  was reached. The plasticity index is the measure of the moisture content range in which the soil behaved plastically. For that, an increase of tensile strength with the increase of  $PI$  indicated that clays at high plasticity index were able to deform more before failing for crack propagation. More deformations implied the development of higher tensile strengths.

A direct comparison between the plot showed in Figures 4.23 and 2.31 found by Fang and Hirst (1973) was not possible. The magnitude of the tensile strength depends on the type of test used to determine the tensile parameters. However, in both tests

there was an increase of tensile strength with the increase of plasticity.

Dry densities are not reported in the graph in Figure 4.23. However, clays had different tensile strengths varying their densities and maintaining the same plasticity index.

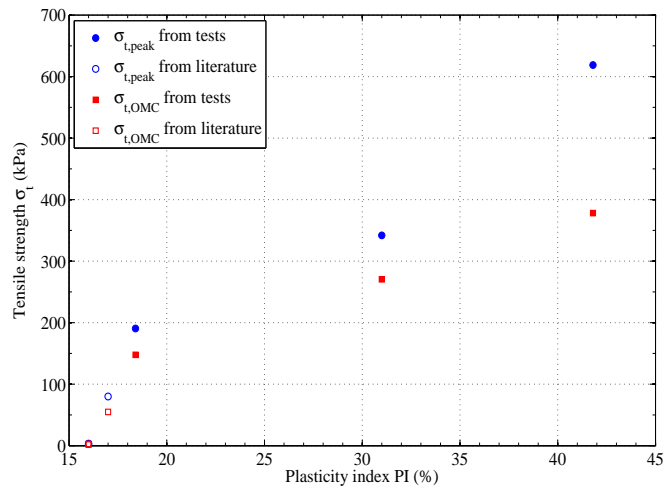


Figure 4.23: Relationship between the plasticity index and the tensile strengths recorded at the peak and at the OMC

## 4.4 Summary

Samples with different moisture contents were studied using direct tensile tests. Speswhite kaolin, Durham and London clay showed a nonlinear behaviour for wet beams while a more linear-elastic response was found moving towards the dry side. The tensile strengths were then related to the moisture content variation. The relationship had a nonlinear curve with a strength peak close to the optimum moisture content  $\omega_{OMC}$ . The peak tensile strength was equal to 300 kPa in the case of kaolin, 600 kPa in London clay and 190 kPa in Durham clay. Those values were found for ratios  $\omega/\omega_{OMC}$  equal respectively to 0.7, 0.9, 0.9.

Tensile strengths were also related to the plasticity index PI variation showing an increasing strength with increasing plasticity.



## Chapter 5

# Bending test results

The clay layer that overlies a cavity can be sketched as a fixed ended beam, as explained in section 2.1.1. To study the tensile stresses in the middle section of the beam, a simpler mechanical model was adopted. A simply supported beam was studied in bending conditions. The beam deforms until the ultimate tensile strength is exceeded in the central section and the beam fails due to crack propagation.

This chapter reviews the results found adopting the simplified model, a simply supported beam undergoing 3-point bending. Load-displacement graphs were plotted for the three clays studied. Results were then related to the variation of moisture content.

### 5.1 Test results

Speswhite kaolin, London and Durham clays were studied under bending conditions to understand the relationship between the load and moisture content.

Squared beams were studied in 3-point bending tests, as described in the methodology chapter. During the test, a crack propagated from the initial notch through the beam height. Similarly to the direct tensile tests, beams with different moisture contents were obtained drying the samples in the oven. The moisture content range for the three clays studied was:

- Speswhite kaolin

- No drying:  $\omega = 44.8 - 47.8 \%$  ( $\omega/\omega_{OMC} = 1.32 - 1.41$ )
- 90 minutes of drying:  $\omega = 36.4 - 39.1 \%$  ( $\omega/\omega_{OMC} = 1.07 - 1.15$ )
- 150 minutes of drying:  $\omega = 32.4 - 34 \%$  ( $\omega/\omega_{OMC} = 0.95 - 1.00$ )
- Durham clay
  - No drying:  $\omega = 25.8 - 26.6 \%$  ( $\omega/\omega_{OMC} = 1.66 - 1.72$ )
  - 30 minutes of drying:  $\omega = 20.8 - 22.8 \%$  ( $\omega/\omega_{OMC} = 1.34 - 1.47$ )
  - 90 minutes of drying:  $\omega = 17.0 - 19.3 \%$  ( $\omega/\omega_{OMC} = 1.10 - 1.25$ )(Table).
- London clay
  - No drying:  $\omega = 34.4 - 37.7 \%$  ( $\omega/\omega_{OMC} = 1.40 - 1.54$ ) for undisturbed clay samples,  $49.5 - 50.6 \%$  ( $\omega/\omega_{OMC} = 2.02 - 2.07$ ) for reconstituted samples
  - 45 minutes of drying:  $\omega = 34.9 - 36.2 \%$  ( $\omega/\omega_{OMC} = 1.42 - 1.48$ )
  - 90 minutes of drying:  $\omega = 30.1 - 32.5 \%$  ( $\omega/\omega_{OMC} = 1.23 - 1.33$ )

Table 5.1 summarises the moisture contents studied. The undisturbed London clay was defined in the table as ‘real’. The reconstituted London clay was reported in the table as ‘lab’.

The maximum moisture content used during the experiments could be seen as a limit. After that, beams were not able to sustain themselves and collapsed under their own weight. For kaolin the maximum moisture content studied was equal to 47.8 %, 50.6 % for London clay and 26.6 % for Durham clay.

Ranges of moisture contents adopted in literature for the bending tests are:

- Indraratna and Lasek (1996): silty clay  $\omega/\omega_{OMC} = 0.93 - 1.28$
- Viswanadham et al. (2010): three kaolin+sand mixtures  $\omega/\omega_{OMC} = 0.88 - 1.17/1.03 - 1.26/0.99 - 1.35$
- Amarasiri et al. (2011): Werribee clay  $\omega/\omega_{OMC} = 0.64 - 1.83$
- Plé et al. (2012): Aptien clay  $\omega/\omega_{OMC} = 0.91 - 1.26$

Clay	LL (%)	PL (%)	$\omega_{min}$	$\omega_{max}$	$\Delta\omega$	$\omega_{OMC}$
Kaolin	65	34	32.4	47.8	15.4	34.0
Durham clay	41.7	23.3	17.0	26.6	9.6	15.5
London clay real	75.3	33.5	34.4	37.4	3.0	24.5
London clay lab	75.3	33.5	30.1	50.6	20.5	24.5

Table 5.1: Summary of the moisture contents studied in the 3-point bending tests.  $\Delta\omega = \omega_{max} - \omega_{min}$

- Wang et al. (2007b): clay+gravels  $\omega = 16.3 - 19.3$  %

The moisture contents found in literature were usually smaller than those used in this investigation. The choice of studying wet beams was explained by the results found from previous sinkhole events: the sinkhole triggering factor was a lowering of the water table. So, at the beginning of the sinkhole formation the clayey soil is in a wet condition.

Typical curves obtained from the bending tests are shown in Figures 5.1, 5.2 and 5.3 respectively for the Speswhite kaolin, London and Durham clay.

As discussed in the drying analysis (Section 3.4), the moisture content in the central section of the beams was considered constant. After the test, a selection of kaolin specimens were chopped into small parts around the initial notch to validate the assumption of constant moisture content. The results are shown in Figure 5.4. Similar to the findings of Murdoch (1992), water in the clay was attracted towards the tip of the initial notch from the volume immediately adjacent. In this manner the fracture tip prevented being dried by the air coming in contact with the soil. For this reason the regions slightly below the notch had a lower moisture content, while at the level of the notch tip the highest moisture content was recorded. Despite these moisture content variations, it was possible to see that the average moisture content was equal to 43.4 % for the beams not dried in the oven, 33.8 % for the beams dried for 90 minutes and 30.5 % for the beams dried in the oven for 150 minutes. Similar results were assumed for the London and Durham clay beams.

## 5.2 Flexural strength calculation

In this case, the calculation of the stress-strain curves was not straightforward due to the nonlinearity between the load and displacements. Moreover, the cross-sectional area was unknown because it was changing with the growth of the crack.

A first calculation of the flexural strength was done hypothesising the linear elastic conditions. The Navier formula was used to calculate the tensile stress at the moment of maximum load:

$$f_t = \frac{M_{max}}{I}y, \quad I = \frac{1}{3}BW^3, \quad y = W - a_0 = \frac{W}{2}, \quad M_{max} = \frac{P_{max}S_p}{4} \quad (5.1)$$

where  $f_t$  is the flexural strength developed during the beam bending,  $M_{max}$  is the maximum moment generated from the bending,  $I$  is the moment of inertia of the cross-sectional area of the beam,  $B$  is the beam's width,  $W$  the beam's height,  $a_0$  the initial crack length,  $P_{max}$  the maximum load sustained by the beam and  $S_p$  the beam's span. In this manner, a first approximation of the flexural strength values was determined. The flexural strengths obtained are showed in Figure 5.5. Table C.1, C.2, C.3 in Appendix C reports the values of moisture content, flexural strength and strain calculated at the maximum load. Table 5.2 reports a summary of the results.

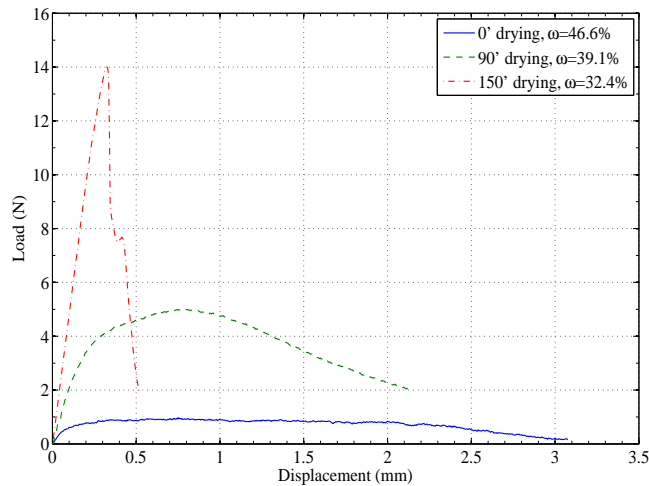


Figure 5.1: Load-displacement graph for Speswhite kaolin (PI=31.0 %) beams at different moisture contents

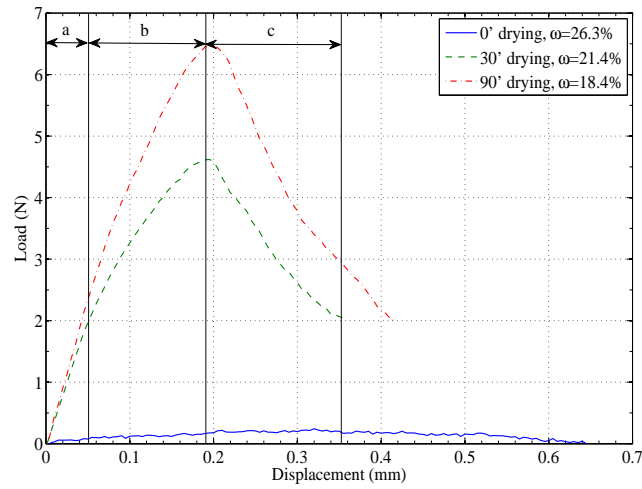


Figure 5.2: Load-displacement graph for Durham clay (PI=18.4 %) beams at different moisture contents

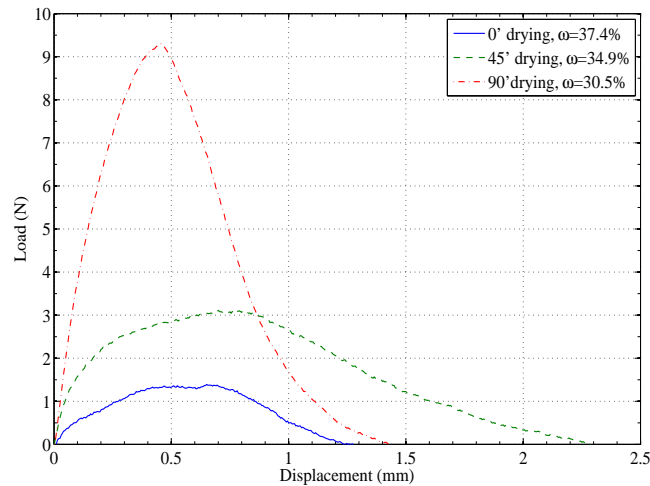


Figure 5.3: Load-displacement graph for London clay (PI=41.8 %) beams at different moisture contents

Indraratna and Lasek (1996) used a slightly different method to determine the flexural strength. They used the 50 % of the peak load to guarantee a linear load-deflection response. In this investigation, the peak load was used. It represents the moment of crack initiation for beams with low moisture contents while it allows a calculation of a conservative value of flexural strength for the beams with a high moisture content. In beams with a high moisture content, the crack initiated after

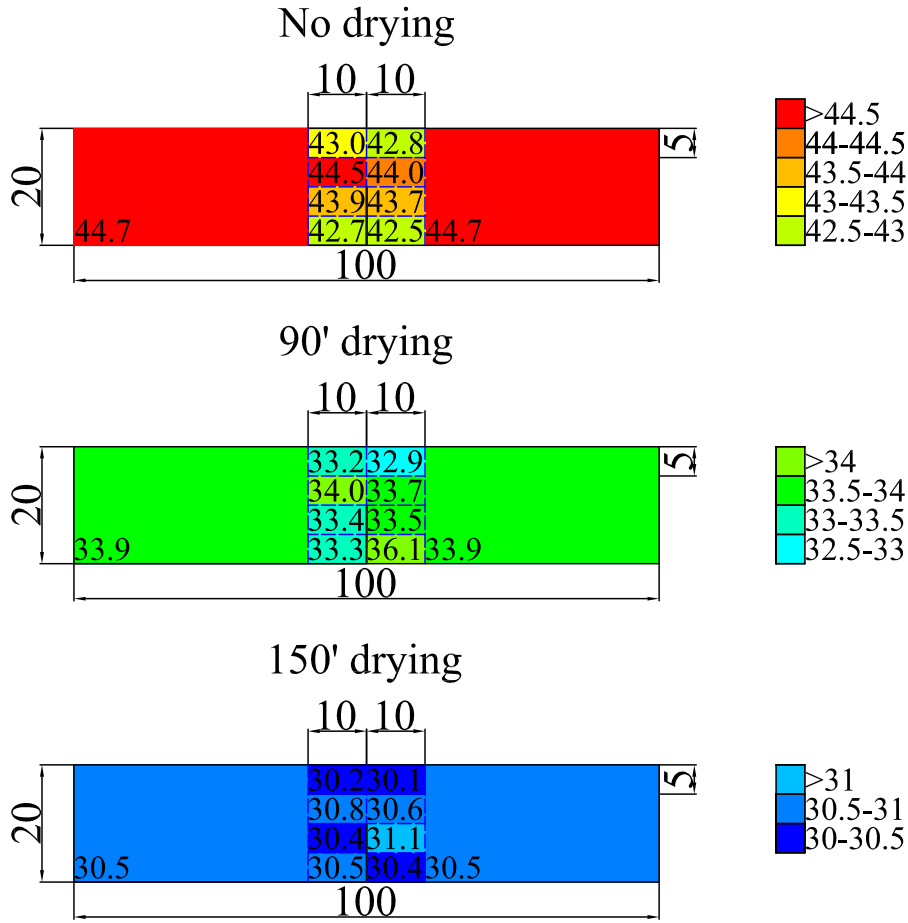


Figure 5.4: Average moisture contents around the central section of kaolin beams

reaching peak load.

The strain was calculated using the formulas presented by Viswanadham et al. (2010). They determined the tensile strain as:

$$\varepsilon = R_{0f}kd \quad (5.2)$$

where  $R_{0f}$  is the neutral layer coefficient, defined as the ratio of vertical distance of the neutral layer from the top surface of the beam to the depth of the soil beam,  $k = 1/R$  is the curvature of the beam along the centreline and  $d$  is the height of the beam (Figure 5.6).  $R$  is the radius of maximum curvature and is computed using:

$$R = \left( \frac{\Delta}{2} + \frac{L^2}{8\Delta} \right) \quad (5.3)$$

where  $\Delta$  is the vertical displacement and  $L$  is half of the length of the sample. In this

Clay	Flexural strength $f_t$ (kPa)		Moisture content $\omega$ (%) for this $f_t$	Strain at max force (%) for this $f_t$
	$f_{t,max}$	$f_{t,min}$		
Kaolin	$f_{t,max}$	210.1	32.4	0.8
	$f_{t,min}$	14.7	46.6	1.9
Durham clay	$f_{t,max}$	97.5	17.0	0.5
	$f_{t,min}$	3.2	26.6	0.2
London clay	$f_{t,max}$	139.6	30.5	1.1
	$f_{t,min}$	13.4	50.2	1.2

Table 5.2: Summary table of the bending test results

investigation  $L$  was equal to half of the span  $L = S_p/2$ . So, the radius of curvature was calculated as:

$$R = \left( \frac{\Delta}{2} + \frac{S_p^2}{32\Delta} \right) \quad (5.4)$$

Figure 5.7 shows the values of strain determined for kaolin, Durham and London clays at the moment of maximum load. This corresponds also to the moment of

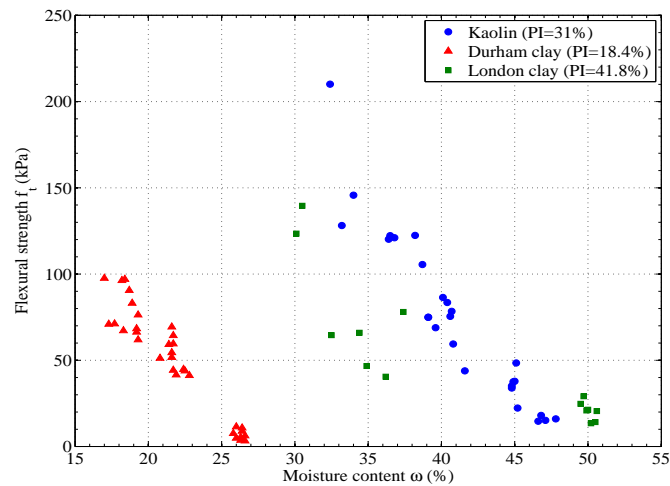


Figure 5.5: Tensile strength for kaolin, Durham and London clays calculated using the Navier formula

maximum flexural strength.

## 5.3 Results discussion

### 5.3.1 Kaolin

Kaolin beams were tested in 3-point bending conditions in a range of moisture content from 32.4 to 47.8 % ( $\omega/\omega_{OMC,K} = 0.95 - 1.41$ ). These values were obtained drying the kaolin beams in the 40°C oven for 0, 90 and 150 minutes.

Figure 5.5 shows that the flexural strength decreases with the increase of the moisture content in a nonlinear manner. The maximum flexural strength was recorded for a moisture content equal to 34.0 % ( $\omega/\omega_{OMC,K} = 1$ ) and was equal to 145.7 kPa. The minimum flexural strength of 16.0 kPa was calculated at a value of  $\omega = 47.8$  % ( $\omega/\omega_{OMC,K} = 1.41$ ).

The strain recorded at the moment of maximum load shows an increase of magnitude moving toward wet samples (Figure 5.7). More deformation is sustained by the beams when the moisture content is high.

### 5.3.2 Durham clay

The flexural strength of Durham clay shows a decreasing magnitude with an increase of moisture content (Figure 5.5). The minimum moisture content of 17.0 %

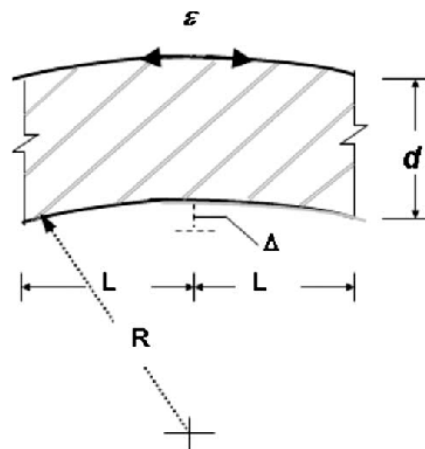


Figure 5.6: Bending symbols used by Indraratna and Lasek (1996) to calculate the tensile strain

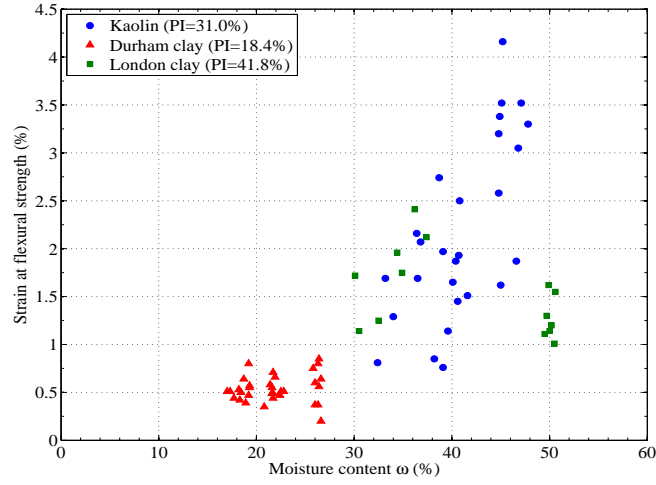


Figure 5.7: Kaolin, Durham and London clays strain recorded at the moment of maximum flexural strength

( $\omega/\omega_{OMC,DC} = 1.10$ ) gave a flexural strength of 97.5 kPa, while the maximum moisture content of 26.6 % ( $\omega/\omega_{OMC,DC} = 1.72$ ) a minimum flexural strength of 6.2 kPa was determined. A more linear tendency than that found for kaolin beams is seen in the data of flexural strength determined from the bending beams of Durham clay. The strain is almost constant for all the values of moisture contents tested. The average strain recorded for every moisture content is equal to 0.5 % (Figure 5.7).

### 5.3.3 London clay

Beams with a moisture content ranging from a moisture content  $\omega = 30.1$  % ( $\omega/\omega_{OMC,LC} = 1.23$ ) to  $\omega = 50.6$  % ( $\omega/\omega_{OMC,LC} = 2.07$ ) were tested in bending conditions. Similar to the data determined from the kaolin and Durham clays tests, the flexural strength of London clay decreases with the increase of the moisture content. A maximum flexural strength of 139.6 kPa was calculated for a moisture content of 30.5 % ( $\omega/\omega_{OMC,LC} = 1.24$ ). The minimum value of flexural strength was equal to 13.4 kPa and was recorded for a moisture content of 50.2 % ( $\omega/\omega_{OMC,LC} = 2.05$ ). The data follows a nonlinear tendency, decreasing moving towards wetter beams. The strain recorded at the point of maximum load shows a decreasing tendency (Figure 5.7). This response is different from the behaviours seen in kaolin and Durham

clays, showing a less capacity of the London clay to sustain bending deformation. Values of strain in a range from 1.0 to 2.5 % were recorded for low moisture contents  $\omega = 30.1 - 37.4$  % ( $\omega/\omega_{OMC,LC} = 1.23 - 1.53$ ). Lower percentage of strain (1.01-1.62 %) were calculated for  $\omega = 49.5 - 50.5$  % ( $\omega/\omega_{OMC,LC} = 2.02 - 2.06$ ). It has to be noticed that the moisture contents at which the London clay beams were studied were close to twice the value of the optimum moisture content. Kaolin and Durham clays beams were studied for lower values of moisture contents.

### 5.3.4 Discussion

Load-displacement curves display a nonlinear response to bending. In the initial part a linear-elastic behaviour was assumed and represented by a straight line (Figure 5.2, part (a) for the beam dried for 30 minutes). Dry samples show a larger linear-elastic response than wet beams. The load increases in a straight line until it reaches the yielding point, then the curve presents a distinct nonlinearity (Figure 5.2, part (b) for the beam dried for 30 minutes). At that stage, the load increased less steeply than before until the maximum was attained. After that, the load started to decrease gradually with the progressive opening of the crack (Figure 5.2, part (c) for the beam dried for 30 minutes). Depending on the moisture content, the reduction in the load magnitude was gentle or steep. Dry beams had a steeper and fast load reduction in comparison to wet beams in which the load diminished more gradually. The maximum loads and displacements sustained by the specimens were influenced by the moisture content. Low moisture contents caused a brittle behaviour of the beams with high loads and small displacements. On the other hand, wet beams sustained large deformations but small loads.

The relationship between the peak load and the moisture content was studied. Among all the bending tests performed on the three clay types, only the data of selected tests were used. The initial notch had to be perfectly aligned with the top roller and the developing crack had to follow a vertical direction. Samples in which the initial notch was not centred in the central section or in which the crack was growing following an inclined direction were discarded because they implied the presence of shear (mixed mode) cracks.

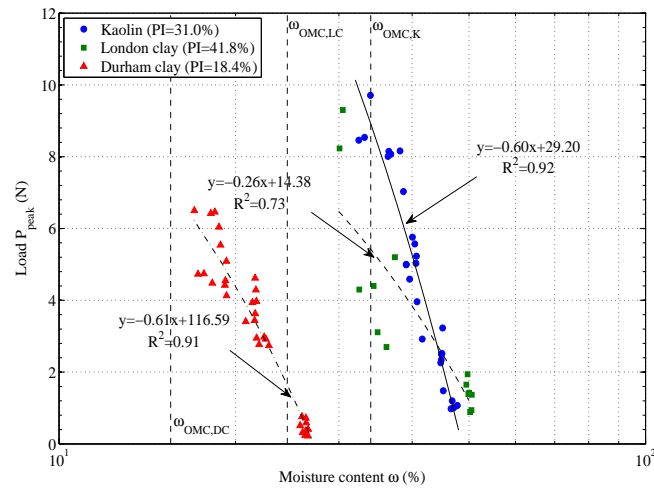


Figure 5.8: Relationship between the peak load and the moisture content for the three different clays

The peak loads are plotted against the moisture content in Figure 5.8. The data show that Durham and kaolin clays had a similar behaviour. Decreasing the moisture content the maximum load was increasing steeply following an almost straight line. The two data series were almost parallel. The data representing London clay followed a more gentle curve with more scattering. This was reflected also in the fitting curve which could not fit the data very well ( $R^2 = 0.73$ ).

The analysis of the flexural strength of Figure 5.5 shows that the three clays have a similar behaviour. A nonlinear decrease of the tensile strength with the increase of the moisture content was recorded for kaolin, Durham and London clays.

Figures 5.9, 5.10, 5.11 show the flexural and tensile strengths of the three clays determined in bending and direct tensile tests in relation to the ratio between the moisture content and the optimum moisture content. Comparing the results obtained from the direct tensile and bending tests, the two values of strengths had a similar behaviour. The two tests gave a clay response that can be seen an exponential decrease of tensile strength with the increase of moisture content. The flexural strength calculated from the bending tests resulted in lower magnitudes than those determined from the direct tensile tests. A low magnitude is explained by the moisture contents of the beams used for the bending tests. Wetter clay samples than the

clay samples tested under direct tensile conditions were used for the bending tests. The flexural strength calculated for kaolin, Durham and London clays was compared with the values found in literature by Indraratna and Lasek (1996), Viswanadham et al. (2010), Amarasiri et al. (2011) and Plé et al. (2012), as Figure 5.12 shows. Indraratna and Lasek (1996) found a polynomial behaviour with a maximum of flexural strength of 94.5 kPa in correspondence of the optimum moisture content. Amarasiri et al. (2011) found an exponential behaviour of the flexural strength in relation to the moisture content. Similar behaviours were determined by Viswanadham et al. (2010). From the graph, a decreasing trend of flexural strength with the increase of moisture content is noticed in all the mixtures of kaolin and sand determined by Plé et al. (2012).

The flexural strength calculated in this investigation follow a similar tendency to those found in literature, in which the strength diminishes with the increase of the moisture content. The results found from the analysis of Werribee clay (Amarasiri et al., 2011), kaolin and London clay show a similar behaviour with a nonlinear decrease moving towards wet beams. The flexural strength of Durham clay follows the results found by Viswanadham et al. (2010) for mixture of 80 % kaolin and 20 % sand compacted using standard and modified Proctor compaction processes. Both the soils studied had a similar plasticity index, included in the range

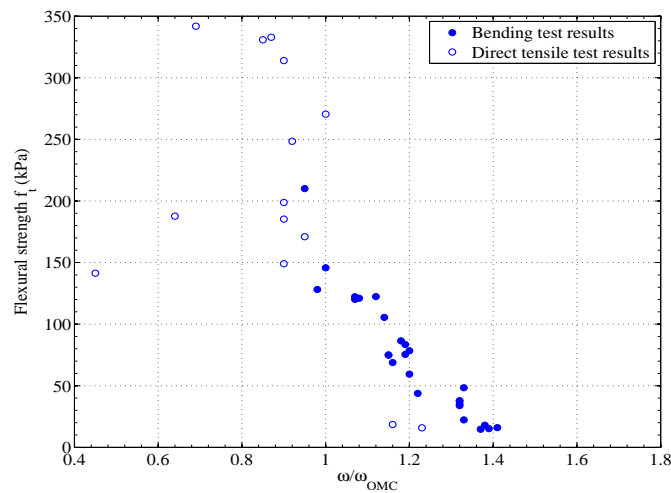


Figure 5.9: Kaolin tensile strengths calculated from bending and direct tensile tests

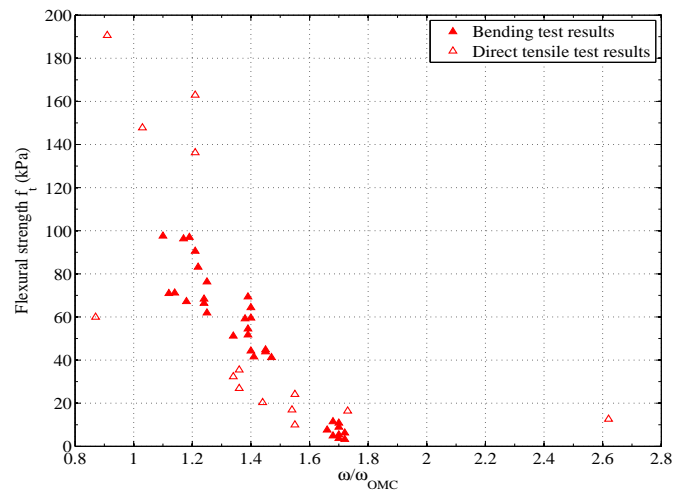


Figure 5.10: Durham clay tensile strengths calculated from bending and direct tensile tests

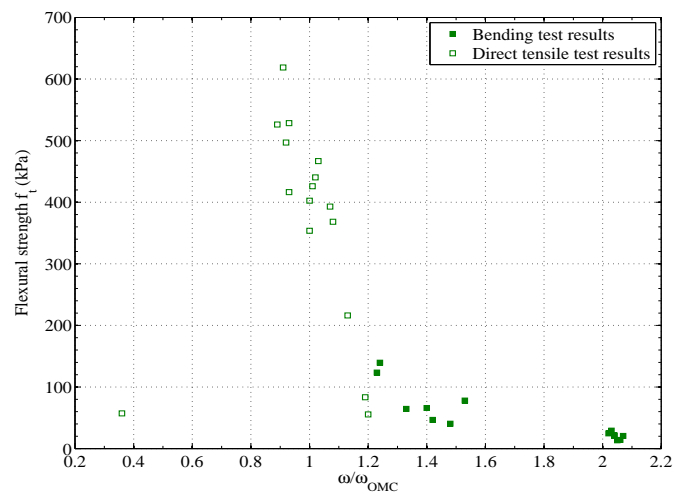


Figure 5.11: London clay tensile strengths calculated from bending and direct tensile tests

$PI = 15 - 18.4 \%$ .

### 5.3.5 Plasticity index

Figure 5.13 shows the tensile strength of the three clays calculated from the bending and direct tensile tests. From the plot, it is noticed that all the points follow the same behaviour despite their plasticity index. This suggests that the tensile behaviour is more affected by the moisture content than the plasticity index. The tensile strength

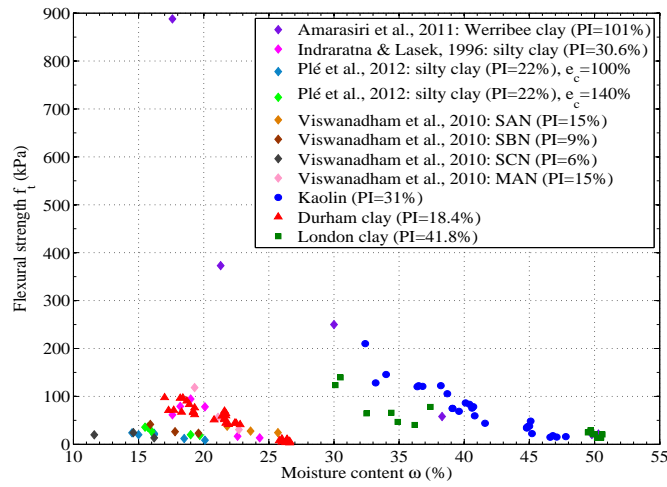


Figure 5.12: Comparison between flexural strength values found in literature and in this investigation

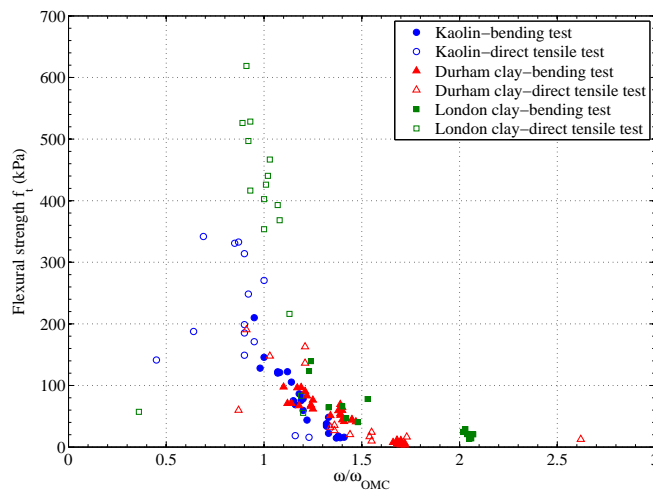


Figure 5.13: Tensile strengths of the three clays calculated from both the tensile tests

is governed by the moisture content and its relationship with the optimum moisture content. For all three clays, the highest values of tensile strength are recorded for moisture contents close to the optimum.

## 5.4 Summary

Beams with different moisture contents were loaded in 3-point bending conditions until they failed for crack propagation.

Speswhite kaolin, London and Durham clays showed a nonlinear behaviour. However, the response moved towards a more brittle behaviour in dry samples.

From the data, it was found that the peak load decreased almost linearly moving from dry to wet samples. No clear relationships were found between the displacements recorded at the peak load and the moisture contents.

The flexural strength and the strain at maximum load were calculated assuming linear-elastic conditions. The trend found was similar for all the data found from the samples of the three clays. The flexural strength decreased in a nonlinear manner with the increase of the moisture content. Only kaolin and Durham clays followed a similar trend to that found by Amarasiri et al. (2011) and Viswanadham et al. (2010). The strain recorded at maximum load had a different behaviour for every clay studied. Kaolin clay had a strain that increased moving towards wet samples. Durham clays had an almost constant strain for all the moisture contents studied. London clays, instead, showed a decreasing deformation when the moisture content was increased.



## Chapter 6

# Analysis of fracture in bending tests

The load-displacement curves found during the 3-point bending tests highlighted a clay behaviour that was markedly nonlinear. For that reason, the linear elastic theory of fracture mechanics cannot be applied to study the fracture behaviour. A more suitable approach was chosen to investigate cracking in these clay samples. Principles of Elasto-Plastic Fracture Mechanics were applied to calculate the crack tip opening angle (CTOA) and determine the J-integral. A similar approach was used by Hallett and Newson (2001, 2005), as reported in section 2.5.2.

Fracture analysis was performed only on kaolin samples. It was chosen as representative of the clay behaviour and its white colour allowed an easy detection of crack growth during the visual analysis. The images of the samples captured during the tests were analysed on the computer. Various parameters were determined measuring the pixels on the digital images and converting them into geometrical measurements. Durham and London clays were not used due to the difficulties encountered detecting the crack profile in the dark-coloured soil mass. This problem was caused by the modeling flock sprayed on the beams. The flock covered the crack front preventing the calculation of the crack length.

A selection of wet kaolin beams not sprayed with the modeling flock was used in the analysis. They behaved in a more ductile manner developing plastic deformations

before failure. Investigations on the crack initiation were conducted on samples with a moisture content ranging from 36 to 45 % ( $\omega/\omega_{OMC} = 1.06 - 1.32$ ) using the images recorded during the tests.

Dry samples were neglected because they failed in a less plastic manner. Their behaviour can be explained by the application of the Linear Elastic Fracture Mechanics, as in Nichols and Grismer (1997), Wang et al. (2007b) and Amarasiri et al. (2011). So, LEFM applications on fracturing beams have been well studied in literature. On the other hand, EPFM was usually not investigated on fracturing clays. On the selected beams an initial analysis of the crack initiation and growth was completed. This analysis was followed by the study of the notch opening and the related parameters. The notch opening was studied using the GeoPIV analysis. At the end EPFM was applied to determine a value of fracture toughness valid for kaolin.

## 6.1 Crack behaviour

During 3-point bending tests it was found that the moisture content influenced the maximum load that a clay beam could sustain and the crack behaviour. The crack initiation and growth changed in relation to the moisture content of the beam.

### 6.1.1 Crack initiation

The instant at which the crack started to propagate from the initial notch into the beam thickness was detected from a manual interrogation of the digital images taken during the tests. From those, it was possible to notice that the sample was undergoing large deflections before the initiation and growth of the crack. With the proceeding test, the initial notch that was cut in the sample started to open changing shape from sharp to blunted (Figures 6.1 and 6.2). The process of notch opening and change of shape from sharp to blunted is called 'blunting'. Beam bending produced rotations of the two beam halves and the rotation of the two notch faces around a centre of rotation located in the beam height. Once the notch reached a blunted

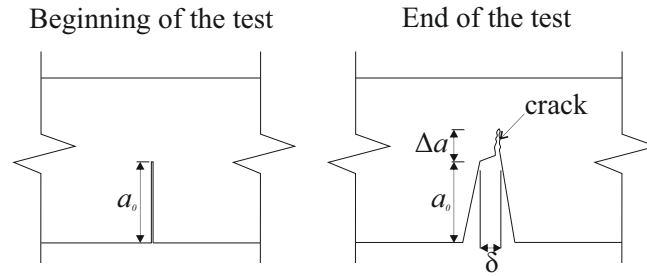


Figure 6.1: Notch geometry modification during the beam bending



Figure 6.2: Initial configuration of the beam notch (a) and the deformed (blunted) notch with a crack developed from the tip (b) in test K0d\_2403.b2

shape, a crack started to develop from the notch tip through the soil thickness. From the tests, it was seen that the moment at which the crack initiated varied with the moisture content. Most of the samples with  $\omega = 44 - 45\%$  ( $\omega/\omega_{OMC} = 1.29 - 1.32$ ) cracked after the sample had reached the peak load, when the displacements were high. Decreasing the moisture content, the moment at which the crack started to be visible through the images occurred before the peak load (Figure 6.3). Only one of the specimens analysed with a moisture content smaller than 44-45% presented a visible crack after the peak conditions (K90d\_1609\_b12:  $\omega = 36.4\%$ ). Decreasing the moisture content the displacements sustained before the crack appearance were smaller. Figure 6.3 shows a decrease in displacement magnitude moving from samples with a moisture content close to 45% to samples with a moisture content close to the optimum. Less deformation and smaller notch opening were seen reducing the amount of water inside the soil mass. This tendency seemed reasonable as the clay response moved toward a less plastic behaviour with the decrease of the

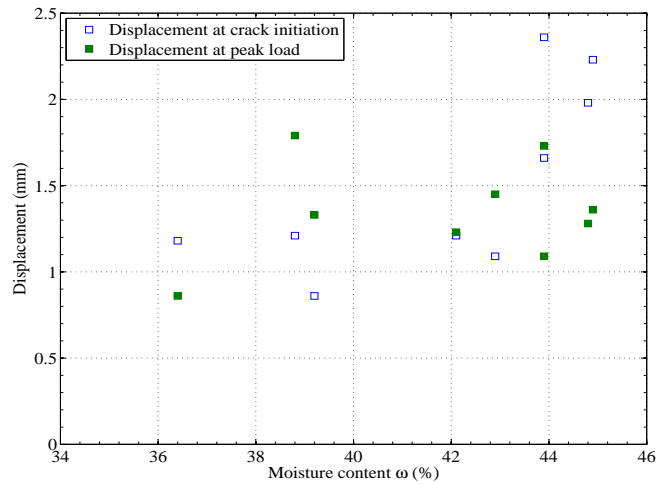


Figure 6.3: Relationship between the displacement at which the crack starts to be visible, the displacement at the peak load and the moisture content

moisture content. This variation of behaviour can be seen more clearly plotting the moment at which the crack started to be visible on the load-displacement graph (Figure 6.4).

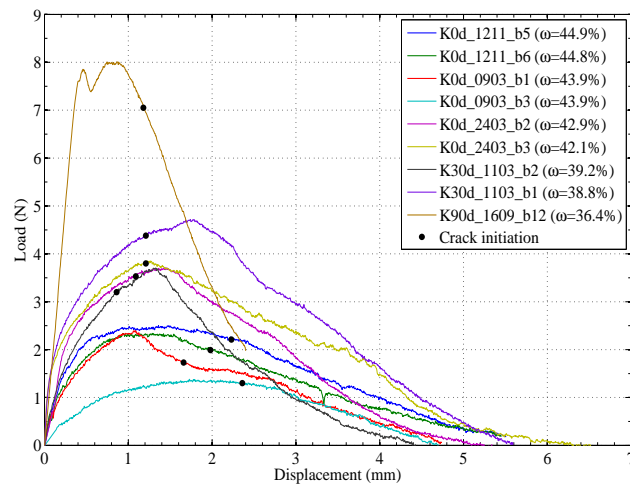


Figure 6.4: Crack initiation in relation to the load-displacement graph

### 6.1.2 Crack extension

The crack usually grew in the vertical direction starting from a corner of the blunted notch. Figure 6.2 shows the vertical crack developed through the beam thickness. Using the digital images recorded, the crack extension  $\Delta a$  was measured. Figure 6.5 shows the crack extension  $\Delta a$  measured from the initial notch and developed during the duration of the test. Initially the beams deformed without any presence of the crack: the notch rotated and opened with a gradual blunting of the tip ( $\Delta a = 0$  mm). At a vertical displacement of approximately 2.0 mm, 1.2 mm and 1.0 mm respectively for tests with a moisture content of 44 %,  $\approx 42$  % and  $\approx 39$  %, the crack started to appear and grow. The crack grew in an unsteady manner and seemed to proceed in steps. Once initiated, the crack developed in jumps suggesting a moment of growth and then stabilisation in the new configuration. This mode of propagation suggested a behaviour similar to that of sinkholes called raveling, in which part of the soil failed in turn until the beam element was unable to sustain the load applied.

Comparing the different crack developments (Figure 6.5) it is possible to see that they were almost similar, especially for  $\omega > 42$  %. However, the decrease of the moisture content caused a faster growth of the crack: e.g. the series of points of the test K90d\_1609\_b12 appears more inclined compared to that of K0d\_0903\_b1. This means that the crack length increased more rapidly. For the same amount of vertical displacement, in beam K90d\_1609\_b12 the crack was more extended through the height. But, in beam K90d\_1609\_b12 the crack started to develop at a lower vertical displacement compared to that of beam K0d\_0903\_b1.

### 6.1.3 GeoPIV

The visual interpretation of the fracture process was not performed on every beam that was studied in bending conditions. Only a set of nine beams was used to study the crack growth. The reason was linked to the fact that before performing the 3-point bending tests most of the beams were sprayed with some modeling flock

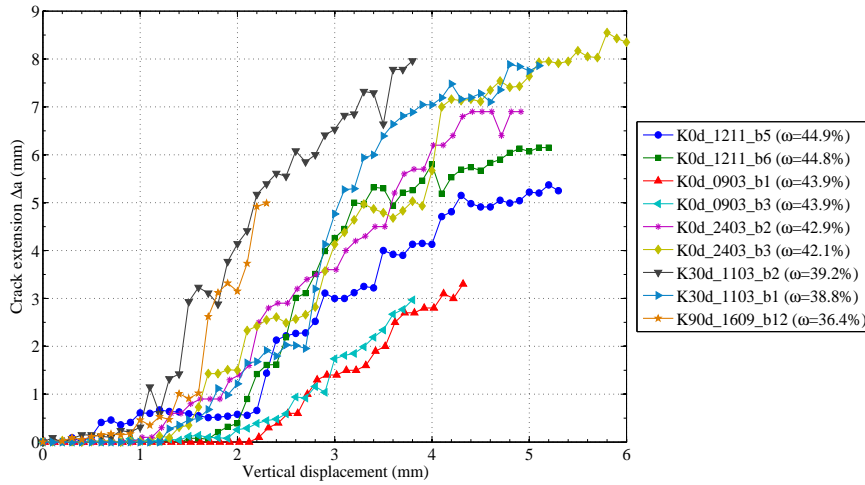


Figure 6.5: Crack extension related to the amount of vertical displacement applied during the test

in order to create a texture for a future analysis with the GeoPIV (White, 2002). A small set of kaolin beams were not sprayed with modeling flock. This set of 9 beams was then used to analyse the fracture process. They were supposed to be used to validate by a visual interpretation what was thought to be calculated using the GeoPIV.

At the beginning of the laboratory tests, the use of the Particle Image Velocimetry (PIV) was thought to be able to detect the crack during the tests. Despite the ability of the GeoPIV to track the crack development, the Matlab routine could not detect the crack front and its movements. However, GeoPIV was able to track the crack formation through the sample height. The arrows of displacements calculated through the sample's height show the crack growth, but the crack front is not visible from the GeoPIV output (Figure 6.6). From the GeoPIV analysis, only the crack mouth opening  $V_{pl}$  and the crack tip opening displacement  $\delta$  (or CTOD) were calculated.

For that, the GeoPIV was used to confirm the results determined by the visual analysis on the kaolin beams with no texture.

Flocked beams with different moisture contents were studied with GeoPIV in order to compare the results found in the visual analysis. The area chosen to be meshed was close to the initial notch to focus on the movements of the opening faces (Figure

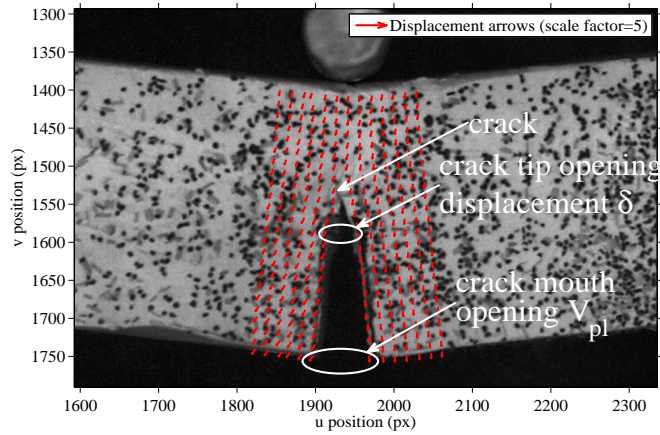


Figure 6.6: Results of the PIV analysis on the beam K0d.1609\_b2 with  $\omega = 45.2\%$

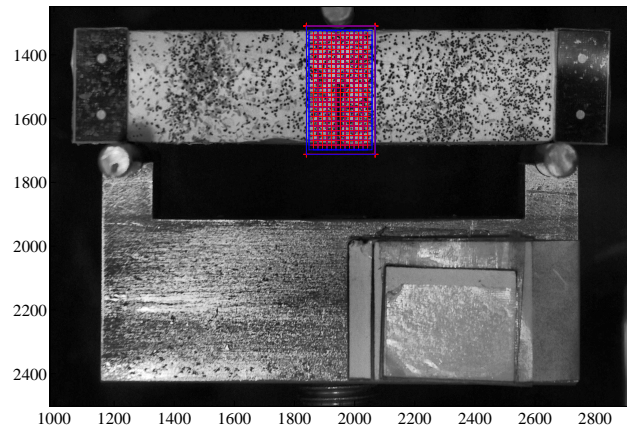


Figure 6.7: GeoPIV mesh used to analyse the beam K0d.1609\_b2 with  $\omega = 45.2\%$

6.7). In particular, attention was paid to the patches at the bottom edge of the beams and at the tip of the initial notch. In order to measure the opening  $V_{pl}$  the first patch on the left and the first patch on the right of the notch were chosen.

The opening at the end and at the tip of the notch was measured. Typical results are plotted in Figure 6.8. At the beginning of the test the load applied on the beam did not cause any significant deformation around the notch: in this first part the displacement of the patches at the beginning and at the end of the notch were of equal magnitude. This part indicated where the sample behaved elastically with

no plastic deformation accumulated. The left and the right part were translating horizontally.

With the continuation of the test, the notch bottom and tip started to behave differently. The bottom started to open quicker than before, while the tip remained almost constant in length. This corresponded to the blunting process, in which plastic deformations were caused by the rotation of the notch faces and blunting of the sharp notch.

After this phase the sample continued to deform plastically until a crack started to develop from the blunted notch tip. This point was highlighted in the graph by a visible variation of the inclination. From this point there was a direct correlation between the vertical displacements applied to the beam and the notch opening: an increase of the vertical displacement corresponded to an exact amount of increase in the notch opening. The point at which this behaviour started allowed the determination of the critical value of the crack tip opening displacement  $\delta_t$  at which the crack initiated. This was calculated as the tip opening corresponding to a vertical displacement pointed with the letter A in Figure 6.8.

After that point, the crack continued to develop as the graph shows. The data followed the identity line so an increase of horizontal displacement corresponded to an equal increase in vertical displacement. During this phase the crack tip opening  $\delta$  remained almost constant. The failure of the sample was highlighted by the increase of the horizontal opening in respect to the vertical displacements indicating that the beam notch was opening more than the magnitude of the vertical displacements applied. In this phase the crack tip opening displacement also started to increase again, reaching a final value which was half of that reached by the crack mouth opening  $V_{pl}$ . The beam can be seen as a rigid body. Figure 6.9 shows that the crack tip opening displacement  $\delta$  and the crack-mouth opening  $V_{pl}$  are related mathematically. Both  $\delta$  and  $V_{pl}$  are calculated from the vertical displacements. The crack-mouth opening results equal to half of the applied vertical displacement. Moreover,  $\delta$  results half of  $V_{pl}$ , as shown in Figure 6.8. However, the results were found ignoring the roller thickness at the top centre support.

Dry beams followed a similar behaviour. However, the point A was not visible in

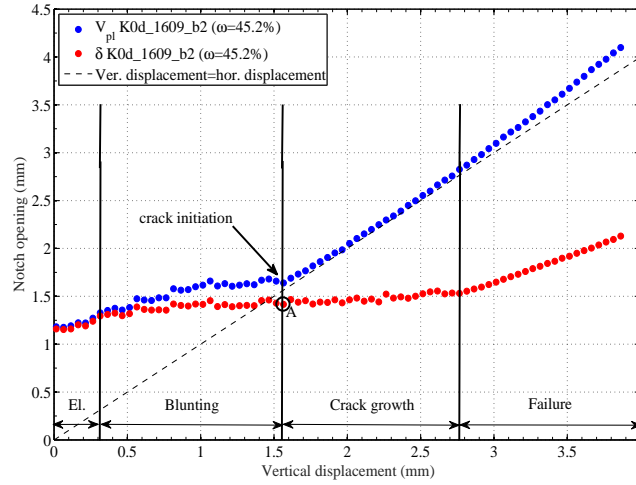


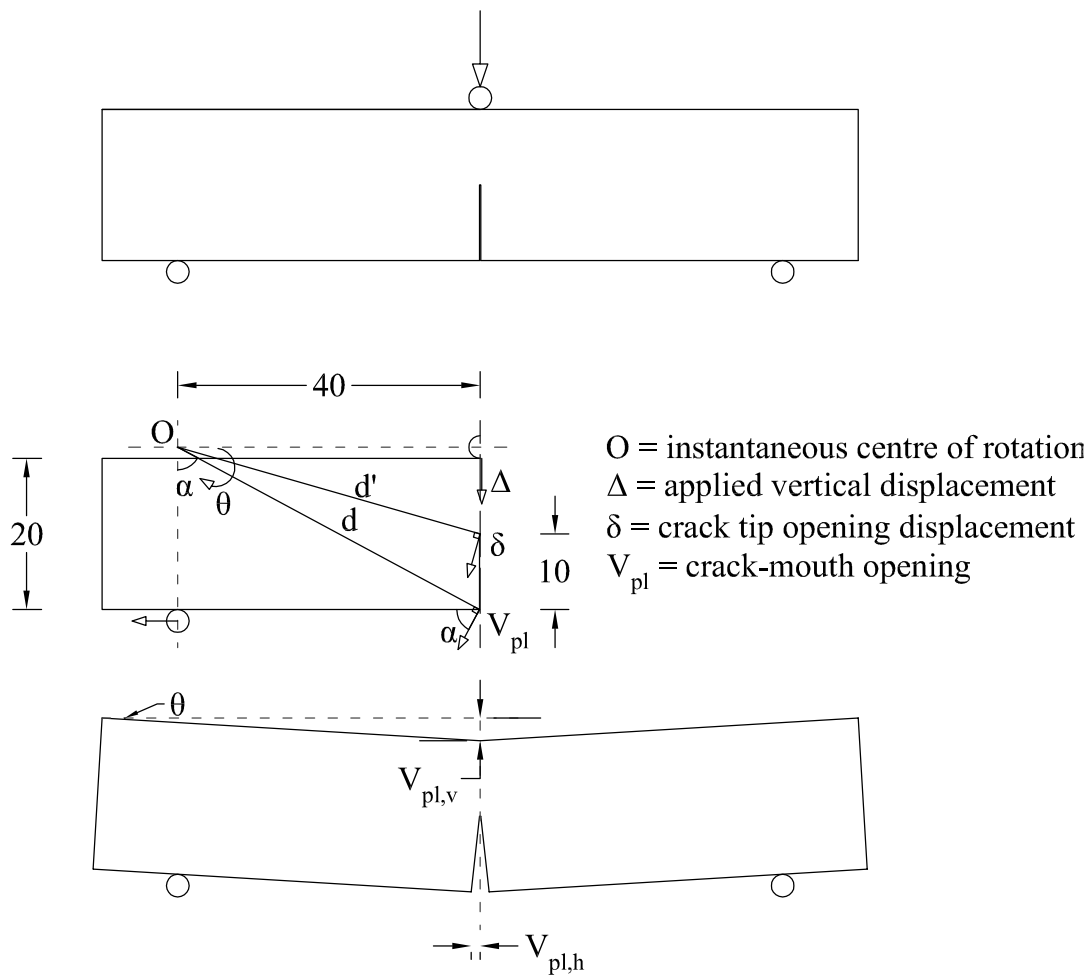
Figure 6.8: Horizontal displacements tracked in beam K0d\_1609\_b2 ( $\omega = 45.2\%$ )

dry samples because the crack developed more instantly. Figure 6.10 shows the data points that reach the identity line gradually. A sharp change of inclination is not seen in the  $V_{pl}$  graph for beam K90d\_1109\_b4 ( $\omega = 38.7\%$ ).

The use of GeoPIV confirmed the behaviour found previously during the visual analysis. The notch opens and then the crack starts to develop after a crack tip opening displacement  $\delta_t$  is reached. An attempt of comparison between the value of CTOD  $\delta_t$  found during the PIV analysis and the visual analysis was done, but the values differ from each other. Figure 6.11 shows the values of  $\delta_t$  found in both the types of analysis. It is clear to see that the values found with the GeoPIV were higher than those found in the previous analysis. However, a general decreasing trend with the decrease of moisture content was followed by all values found.

## 6.2 Ductile cracks

The ductile cracking behavior is described using different parameters that characterised the initial notch opening and the angle at which the crack formed. This approach was suggested by Hallett and Newson (2001, 2005) in their 3-point bending studies on kaolinite beams.



$$\theta = \Delta/40 \quad V_{pl} = \theta d$$

$$\text{tg}\alpha = \frac{40}{20} \quad \text{cos}\alpha = 20/d$$

$$V_{pl,h} = V_{pl} \text{cos}\alpha = \theta d * 20/d = \theta 20 = \Delta/40 * 20 = \Delta/2$$

$$\delta = \theta d'$$

$$\text{cos}\alpha' = 10/d'$$

$$\delta_h = \delta \text{cos}\alpha' = \theta d' * 10/d' = \theta 10 = \Delta/40 * 10 = \Delta/4$$

Figure 6.9: Rigid body movement in bending tests

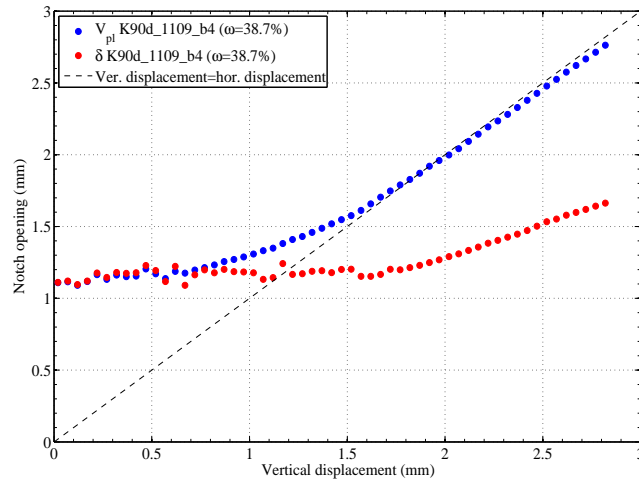


Figure 6.10: Horizontal displacement tracked in beam K90d\_1109\_b4 ( $\omega = 38.7\%$ )

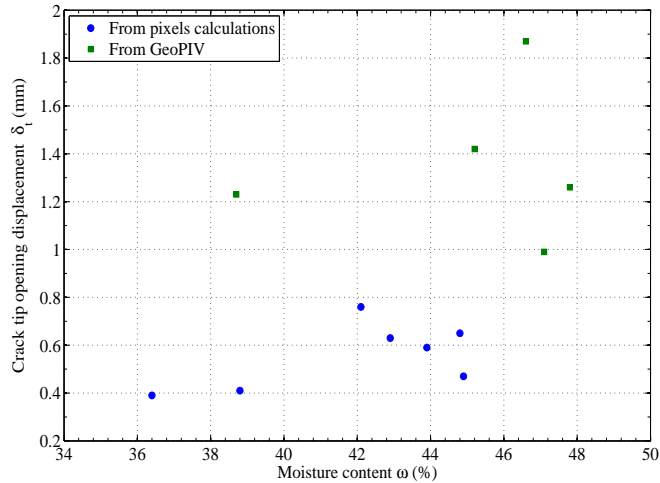


Figure 6.11: Crack tip opening displacement  $\delta_t$  calculated from the images analysis and from the GeoPIV

### 6.2.1 Crack-mouth opening $V_{pl}$

According to the test results, before the initiation of the crack the initial notch passed from a sharp shape to a blunted shape (Figure 6.1, 6.12). The initial notch opened during the tests. The distance between the opening faces of the initial notch is called crack-mouth opening  $V_{pl}$  (Figure 2.40). The subscript ‘ $pl$ ’ introduced by Hallett and Newson (2001, 2005) indicates the plastic stage of the test.

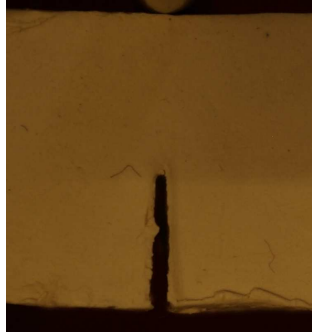
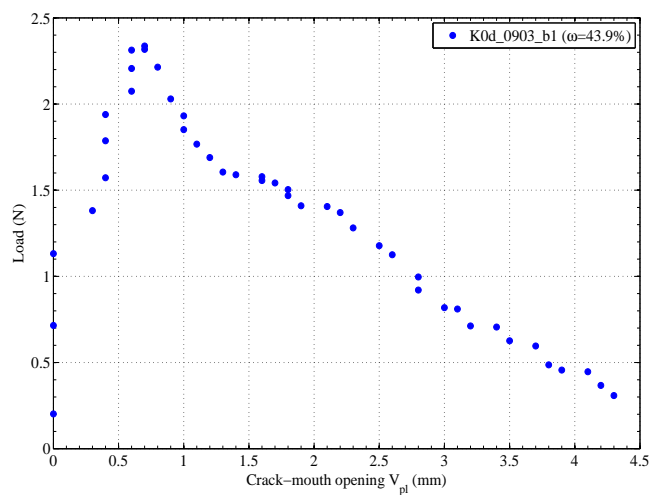


Figure 6.12: Blunted notch seen during test K0d\_2403.b2

At the beginning of the test the initial notch kept its original shape while the beam underwent bending. This phase corresponded to the elastic stage of the test. After the elastic stage, it started to deform and the two faces started to rotate and move apart (Figure 6.13).

$V_{pl}$  is also plotted against the vertical displacement showing an almost linear relationship between these two parameters. Figure 6.14 shows that an increase of vertical displacement corresponded to an almost equal increase of the horizontal opening of the notch faces. The equivalence in displacement/opening magnitude was seen particularly at the end of the tests where beams failed by crack propagation. Only at the beginning of the tests this linear behaviour was not followed.

Figure 6.13: Load-crack mouth displacement  $V_{pl}$  graph for the beam test K0d\_0903.b1

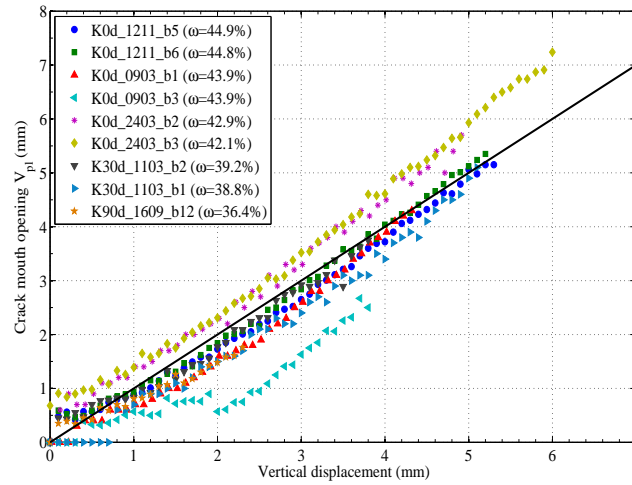


Figure 6.14: Relationship between the crack-mouth opening  $V_{pl}$  and the vertical displacement

Among the tests, K0d\_0903\_b3 showed a slightly different behaviour to the rest. At the beginning of the test, only the bottom part of the notch started to rotate while the tip remained closed. The two faces of the notch stuck together even though the beam was cut. In this manner the beam acted like an intact beam deforming the notch only locally at the bottom. As soon as the bond between the two faces broke due to the increase of the tensile force, the notch tip started to open. This particular behaviour affected the magnitude of the notch opening and therefore test K0d\_0903\_b3 was not considered in the following analysis. The process is pointed out in Figure 6.15.

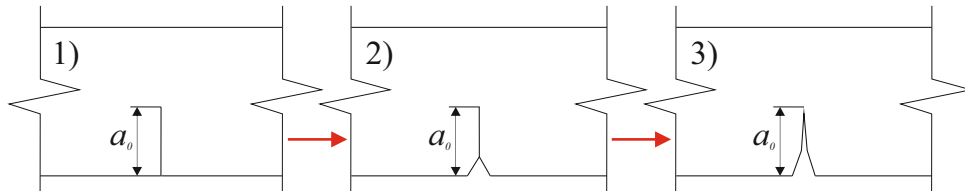


Figure 6.15: Notch geometry modification in beam K0d\_0903.b3

### 6.2.2 Crack opening angle COA

As Hallett and Newson (2001) suggested, the crack-opening mouth did not showed the moment at which the crack started due to the continuous deformation of the ductile beams.  $V_{pl}$  showed an increasing tendency from the beginning to the end of the tests.

Due to the ductility of the samples and their slow cracking process, the measurement of the angle at which the crack formed was more appropriate to describe the whole behaviour of the crack (Hallett and Newson, 2001). They called this angle crack opening angle, COA.

The crack opening angle COA was calculated from the data collected during the tests dividing the crack-mouth opening  $V_{pl}$  by the crack length  $a$  ( $COA = V_{pl}/a$ ). This parameter allowed the calculation of the COA at which the initial notch opened. Figure 6.16 shows the COA plotted against the normalised ligament length  $b/b_0$  to describe the bending process.

At the beginning of the experiments, the ligament length remained equal to its initial value, while the COA increased. At the moment of crack initiation the data moved from the initial vertical trend. The tip of the notch opened until a limit value was reached, then the crack started to appear, reducing the ligament length. The COA increased in all the tests but had different inclinations. Figure 6.16 shows that decreasing the moisture content the crack opening angle inclination decreased. Reducing the moisture content, the COA at which the crack initiated decreased passing from a maximum of  $\approx 0.19^\circ$  in the test K0d\_0903\_b1 to a minimum of  $\approx 0.075^\circ$  in the test K0d\_1103\_b2. The drier the tests, the less deformation and blunting were developed at the notch tip. This indicated that kaolin with a moisture content close to the optimum required less energy to initiate the crack compared to that required for kaolin with a moisture content close to 45 %. However, the COA showed the global behaviour of the samples to lose the ability to deform before and during the crack development as moisture content reduced. Less rotation and consequently less opening of the notch tip were sustained during bending when the moisture content decreased.

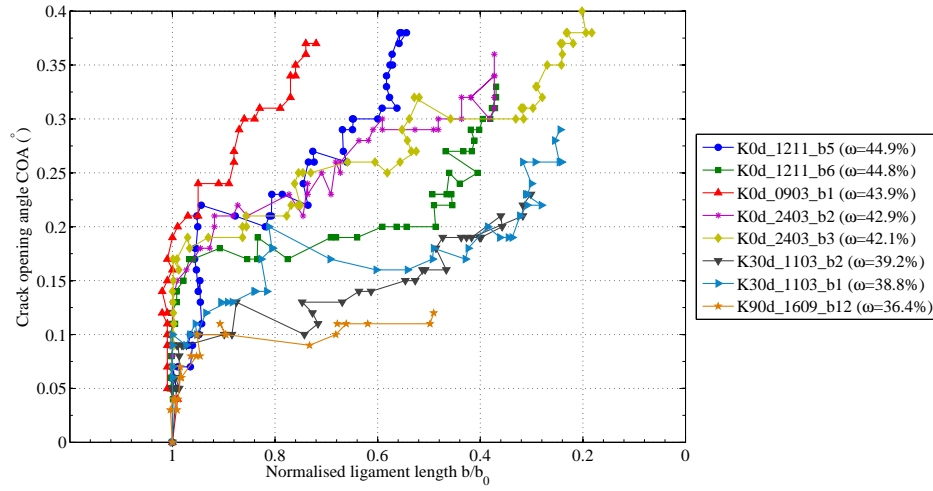


Figure 6.16: Relationship between the Crack Opening Angle COA and the normalised ligament length  $b/b_0$

### 6.2.3 Crack tip opening angle CTOA

Assuming the beam bending behaved as a fully plastic hinge, the CTOA can be calculated from the negative slope of the graph that relates the logarithmic measure of the ligament length  $b$  with the vertical displacement (Hallett and Newson, 2001). The slope of the linear trend that approximated the series of points gives the ratio between the CTOA and the distance measured from the crack tip to the centre of rotation of the two halves of the sample  $\alpha_{g,pl}/r_{pl}$  (Equation 2.20).

Figure 6.17 shows the data collected for the kaolin tests when the deformation was only plastic. The CTOA was then calculated multiplying  $\alpha_{g,pl}/r_{pl}$  for the distance between the center of rotation and the crack tip  $r_{pl}$ , as defined by Equation 2.21. The  $r_{pl}$  value can be determined as the slope of the linear trend that approximates the data of the vertical displacement and the crack-mouth opening during plastic deformation (Figure 6.18).

Table 6.1 reports the values of  $\alpha_{g,pl}/r_{pl}$ ,  $r_{pl}$  and  $\alpha_{g,pl}$  for the clay beams studied. The decrease in moisture content resulted in a decrease of  $\alpha_{g,pl}$ . Figure 6.17 shows a decrease of inclination of the data series when the moisture content is reduced. The highest  $\alpha_{g,pl}/r_{pl}$  are obtained from the wettest beams, while low values of  $\alpha_{g,pl}/r_{pl}$  are calculated from the kaolin beams with lower moisture contents. So, moving towards

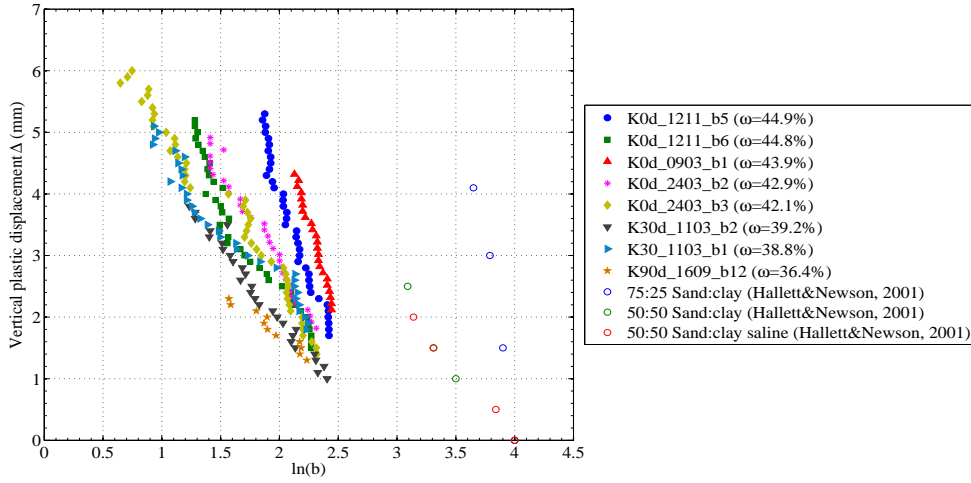


Figure 6.17: Relationships between the logarithm of the ligament length  $b$  and the vertical displacement. The equations of the linear relationships are reported in Table 6.2

samples with a moisture content close to the optimum suggests a decrease of the amount of energy necessary to fracture the beams, as the decrease of CTOA shows. Logically a decrease of the CTOA indicated a more instantaneous crack, while a high value of CTOA underlined a more plastic behaviour with large deformations and a slow crack growth. The CTOA can be seen as the level of strain that was necessary for the crack to propagate into the beam thickness (Hallett and Newson, 2001, 2005). A small  $\alpha_{g,pl}$  indicated that kaolin was more susceptible to cracking (e.g. Test K30d\_1103\_b1,  $\alpha_{g,pl}=2.25$ ) compared to a wet ductile kaolin with a high  $\alpha_{g,pl}$  (e.g. Test K0d\_0903\_b1,  $\alpha_{g,pl}=8.18$ ). Anomalous values were found in beams K0d\_1211\_b5 and K0d\_1211\_b6. Despite the high moisture content the CTOA was lower than that found in beams with  $\omega = 43.9\%$ .

The data found by Hallett and Newson (2001) had a similar behaviour to that of the kaolin beams studied in this investigation (Figure 6.17). But, the  $\ln(b)$  values found in Hallett and Newson (2001) were completely different from those calculated in this study, although the same height was used in the fracturing beams (20 mm). In addition, Hallett and Newson (2001) did not vary the moisture content inside the samples but they studied the influence of the amount of kaolin inside the soil mixture on the fracturing behaviour.

Test No.	Moisture content $\omega$ (%)	$\alpha_{g,pl}/r_{pl}$	$r_{pl}$	$\alpha_{g,pl}$
K0d_1211_b5	44.9	5.57	1.06	5.90
K0d_1211_b6	44.8	3.03	1.10	3.33
K0d_0903_b1	43.9	6.54	1.28	8.37
K0d_2403_b2	42.9	3.11	1.14	3.55
K0d_2403_b3	42.1	2.55	1.20	3.06
K30d_1103_b2	39.2	2.38	1.03	2.45
K30d_1103_b1	38.8	2.06	1.09	2.25
K90d_1609_b12	36.4	1.37	0.70	0.96
75:25 Sand:clay <sup>a</sup>	-	0.22	0.69	0.19
50:50 Sand:clay <sup>a</sup>	-	0.15	1.65	0.24
50:50 Sand:clay saline <sup>a</sup>	-	0.14	1.69	0.25

Table 6.1: Fracture mechanics parameters determined from the 3-point bending tests performed on wet kaolin beams. The tests with the subscript ‘*a*’ are taken from Hallett and Newson (2001)

Test No.	Moisture content $\omega$ (%)	Equation linear approximation	$R^2$
K0d_1211_b5	44.9	$\Delta = -5.57 \ln(b) + 15.25$	0.96
K0d_1211_b6	44.8	$\Delta = -3.03 \ln(b) + 8.51$	0.93
K0d_0903_b1	43.9	$\Delta = -6.54 \ln(b) + 18.25$	0.98
K0d_2403_b2	42.9	$\Delta = -3.11 \ln(b) + 9.05$	0.97
K0d_2403_b3	42.1	$\Delta = -2.55 \ln(b) + 7.67$	0.97
K30d_1103_b2	39.2	$\Delta = -2.38 \ln(b) + 6.72$	0.98
K30d_1103_b1	38.8	$\Delta = -2.06 \ln(b) + 6.66$	0.94
K90d_1609_b12	36.4	$\Delta = -1.37 \ln(b) + 4.46$	0.93

Table 6.2: Equations of the linear relationships between the logarithmic measurement of the ligament length  $b$  and the vertical displacement applied on the beams

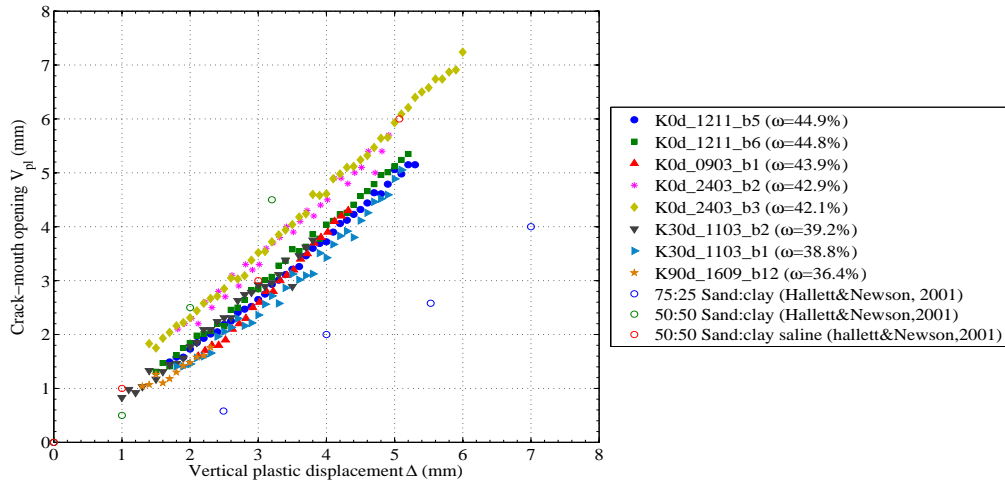


Figure 6.18: Linear relationships between the vertical plastic displacement and the crack-mouth opening. The equations of the linear relationships are reported in Table 6.3

### 6.3 J-integral

The second parameter associated with nonlinear elastic fracture mechanics is the J-integral. It represents the energy release rate in the case of nonlinear material response and it is equivalent to the energy release rate  $G$  in the case of materials

Test No.	Moisture content $\omega$ (%)	Equation linear approximation	$R^2$
K0d_1211_b5	44.9	$V_{pl}=1.06\Delta-0.46$	1.00
K0d_1211_b6	44.8	$V_{pl}=1.10\Delta-0.41$	1.00
K0d_0903_b1	43.9	$V_{pl}=1.28\Delta-1.23$	1.00
K0d_2403_b2	42.9	$V_{pl}=1.14\Delta-0.03$	0.99
K0d_2403_b3	42.1	$V_{pl}=1.20\Delta-0.08$	1.00
K30d_1103_b2	39.2	$V_{pl}=1.03\Delta-0.27$	0.98
K30d_1103_b1	38.8	$V_{pl}=1.09\Delta-0.78$	0.99
K90d_1609_b12	36.4	$V_{pl}=0.70\Delta+0.08$	0.92

Table 6.3: Equations of the linear relationships between the vertical displacement applied on the beams and the crack-mouth opening  $V_{pl}$

with linear elastic behaviour.

The COA and CTOA analysis were already applied to clay for studying fracture, but fracture analysis through the calculation of the J-integral was studied in the past only by Chandler (1984) on beams having a different geometry. For this reason, the procedure adopted was the one suggested by the ASTM:E1820-15 (2015) to study the metal response in similar tensile conditions. The aim was to determine if the procedure used for metals could be applied, with appropriate modifications, to clay behaviour.

### 6.3.1 J-integral calculation

The standard ASTM:E1820-15 (2015) calculates the J-integral in plane strain conditions as the sum of two different parts, one for the elastic field and one for the plastic field (Equation 2.13).

$$J = J_{el} + J_{pl} \quad (6.1)$$

where the elastic component is given by:

$$J_{el} = \frac{K^2(1 - \nu^2)}{E} \quad (6.2)$$

and the plastic component by:

$$J_{pl} = \frac{\eta_{pl} A_{pl}}{B_N b_0} \quad (6.3)$$

$K$  is the fracture toughness calculated in the linear elastic conditions, defined by the Equations 6.4 and 6.5.

$$K_{(i)} = \left[ \frac{P_i S_p}{B W^{3/2}} \right] f(a_i/W) \quad (6.4)$$

$$f\left(\frac{a_i}{W}\right) = \frac{3\left(\frac{a_i}{W}\right)^{1/2} \left[ 1.99 - \left(\frac{a_i}{W}\right) \left(1 - \frac{a_i}{W}\right) \left( 2.15 - 3.93 \left(\frac{a_i}{W}\right) + 2.7 \left(\frac{a_i}{W}\right)^2 \right) \right]}{2 \left(1 + 2 \frac{a_i}{W}\right) \left(1 - \frac{a_i}{W}\right)^{3/2}} \quad (6.5)$$

where:

$P_i$  is the load at the instant  $i$ ;

$S_p$  is the beam span;

$W$  is the beam height;

$a_i$  is the crack length at the instant  $i$ ;

$\nu$  is the Poisson's ratio;

$E$  is the Young's modulus;

$\eta_{pl}$  is equal to 1.9 (metals case);

$A_{pl}$  is the area under the load-displacement graph (Figure 6.19);

$B_N = B$  is the specimen width in case of no side grooves;

$b_0 = W - a_0$  is the original resistant ligament length.

The subscript  $i$  represents the generic instant at which the parameters are calculated.

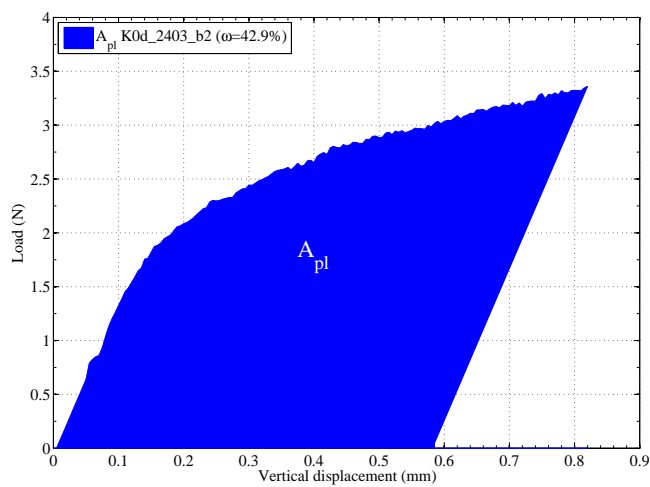


Figure 6.19: Calculation of the plastic area for the test K0d\_2403\_b2 ( $\omega = 42.9\%$ )

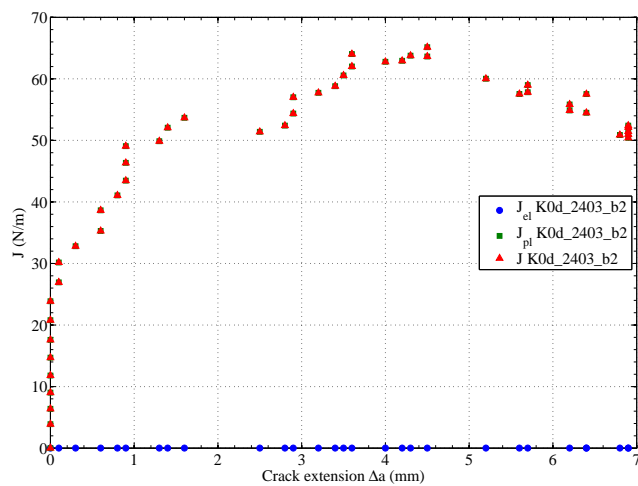


Figure 6.20: Different contributions in the calculation of the J-integral for the test K0d\_2403\_b2 ( $\omega = 42.9\%$ )

The width  $B_N$  used in the formula was corrected in order to account for the difference of geometry between that adopted in the ASTM:E1820-15 (2015) where  $B = 0.5W$  and in the clay beams tested. The clay beams used had  $B_{N,clay} = 2B_{N,metals}$  with  $B_N = B$  because there were no side grooves.

Using these formulas, the J-integral was calculated for all the kaolin beams. Figure 6.20 reports the influence of the elastic and plastic components and the final values of the J-integral for the beam test K0d\_2403\_b2. The parameter was calculated at steps of 0.1 mm (step adopted choosing 1 photo every 20 photos of the series recorded in the test). The contribution of the elastic part was negligible in comparison to the plastic contribution. In addition, at the beginning of the test the J-integral increased in magnitude without any increase of the crack length. The energy was dissipated with the rotation of the two beam halves and the notch blunting. Moreover, the increment of crack length due to the blunting process was so small that it was not possible to measure it from a visual analysis of the photos.

Figure 6.21 shows the J-integral curve reported in ASTM:E1820-15 (2015) as an example of the results found in metals. From a first comparison the two curves are similar. The clay data decreased at the end of the test because they were not limited in the range  $0 - \Delta a_{max}$  as the curve of Figure 6.21,  $\Delta a_{max}$  being the maximum crack capacity of the beam.

Different behaviours of the J-integral were expected in relation to the different moisture contents adopted. Figure 6.22 compares the J-integrals calculated for the eight tests analysed. The influence of the moisture content on the behaviour is visible from the graph in which the magnitude of the J-integral decreases with the increase of moisture content. The only exception to this response was seen with the beam K30d\_1103\_b2. Despite the low moisture content, the energy required to propagate the crack was lower than that required for beams with  $\omega = 43.9\%$ . So, this test was not considered in the further analysis due to its anomalous behaviour.

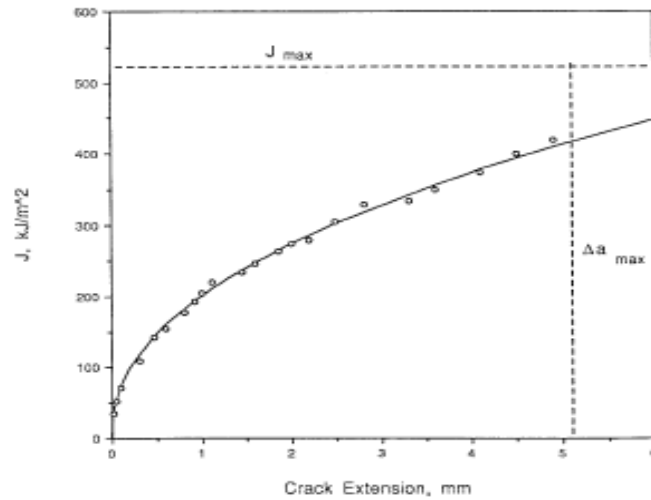


Figure 6.21: Typical curve obtained from metals in tensile conditions taken from ASTM:E1820-15 (2015)

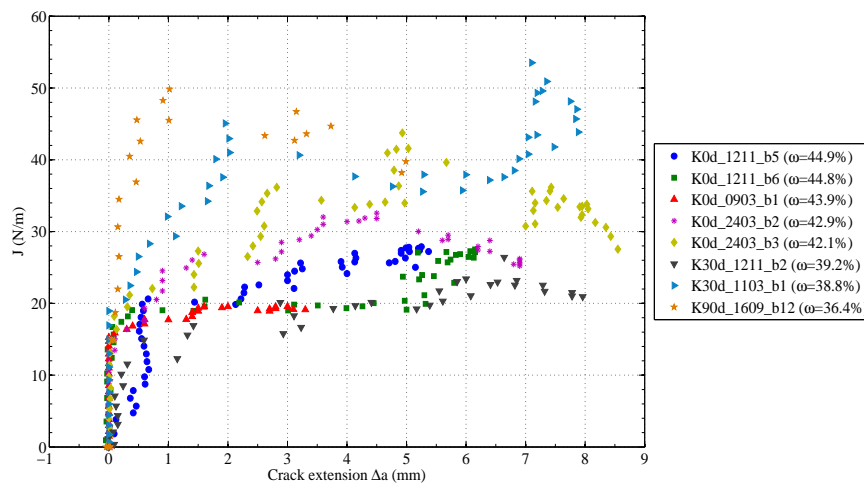


Figure 6.22: J-integral values calculated during the tests

### 6.3.2 Fracture toughness calculation

The nonlinear analysis explained in the standard ASTM:E1820-15 (2015) then determines the range of data to consider in the calculation of the critical value of the J-integral (or fracture toughness). The first step is the calculation of the J-R curve. The limits of the specimen capacity were determined by the parameters  $J_{max}$  and  $\Delta a_{max}$ . They defined a range of points that could be used to define the J-R curve

and in metals they are calculated empirically as a percentage of the initial geometry parameters using the equations:

$$J_{max} = \min \begin{cases} b_0\sigma_Y/10, \\ B\sigma_Y/10, \end{cases} \quad (6.6)$$

$$\Delta a_{max} = 0.25b_0 \quad (6.7)$$

where  $\sigma_Y$  is the effective yield strength equal to the 0.2 % offset yield strength  $\sigma_{YS}$  and the ultimate tensile strength  $\sigma_{TS}$ :  $\frac{\sigma_{YS} + \sigma_t}{2}$ ,  $b_0$  is the initial ligament length,  $B$  is the beam width.

$J_{max}$  and  $\Delta a_{max}$  were calculated for the clay tests using the yield strength and the tensile strength determined during the direct tensile tests (Section 4.3). For every moisture content,  $\sigma_{YS}$  and  $\sigma_t$  were calculated using the fitting curve used to approximate the data of the beams on the wet side of the optimum moisture content.

However, while the value  $\Delta a_{max}$  seemed to be reasonable in the clay cases,  $J_{max}$  cannot be used on soils due to the low magnitude of the effective yield strength of wet clays. Figure 6.23 shows the values of  $\Delta a_{max}$  and  $J_{max}$  in relation to the J-integral values found in test K0d.2403\_b2.  $J_{max}$  cannot be used in the case of wet clays as it excluded the majority of the tests data. So, only  $\Delta a_{max}$  was used in the determination of the J-R curve, while  $J_{max}$  was neglected in the fracture analysis done in this investigation.

In the standards, the J-R curve is calculated as a power law regression line and represents the best approximation of the J-integrals. Using the same procedure, the J-R curves were calculated also for the kaolin beams. Figure 6.24 shows the J-R curve for the beam test K0d.2403\_b2 obtained using the data included in the range of crack extension  $0 - \Delta a_{max}$ . As in the case of metals, the J-integrals were approximated using a power law regression curve.

As expected, moisture content had an influence on the J-integral trend, as it is possible to see in Figure 6.25. Higher moisture contents indicated lower magnitudes of the J-integral.

The determined J-R curve were used for the calculation of the  $J_{Ic}$  parameter which is the toughness of the material at the beginning of crack propagation. In the case of

metals, the ASTM:E1820-15 (2015) suggests to calculate  $J_{Ic}$  from the intersection of a straight line, called the offset or blunting line, with the power law regression curve (Figure 2.18).

Due to the similarity between the data obtained from the clay beams and the curves found for metals in the standards ASTM:E1820-15 (2015), in Janssen et al. (2002) and Anderson (2005), the procedure of the blunting line calculation could also be appropriate for the clay results. Some modifications to the original formula coefficients were suggested due to the difference in resistance of the clays in comparison with that of metals.

The first step is drawing the blunting line in the graph  $J-\Delta a$  to describe the apparent crack extension caused by the notch blunting. In the case of metals the line is determined using the equation that relates the effective yield stress with the crack extension:  $J = M\sigma_Y\Delta a$  (ASTM:E1820-15, 2015). A similar equation can also be used to relate  $J$  to the yielding stress and the crack tip opening displacement through the  $M$  parameter:  $J = M\sigma_{YS}\delta_t$ .  $\delta_t$  is the crack tip opening displacement and represents the opening at the notch tip registered at the moment of crack initiation. For metals the constant  $M$  is usually assumed equal to 2 but it can also be determined experimentally as the gradient of the line that best approximates the  $J-\delta_t$  data. This experimental method was applied to clay beams, as Figure 6.26 shows for the test

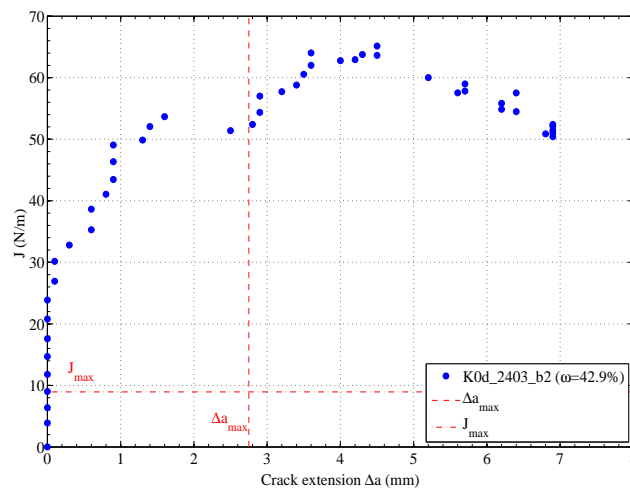


Figure 6.23: Range of values delimited by  $\Delta a_{max}$  and  $J_{max}$  for the test K0d\_2403\_b2 ( $\omega = 42.9\%$ )

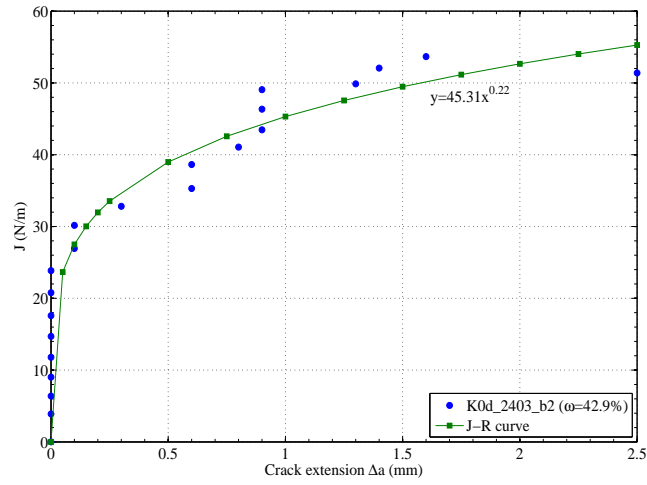


Figure 6.24: J-R curve approximation for the test K0d\_2403\_b2 ( $\omega = 42.9 \%$ )

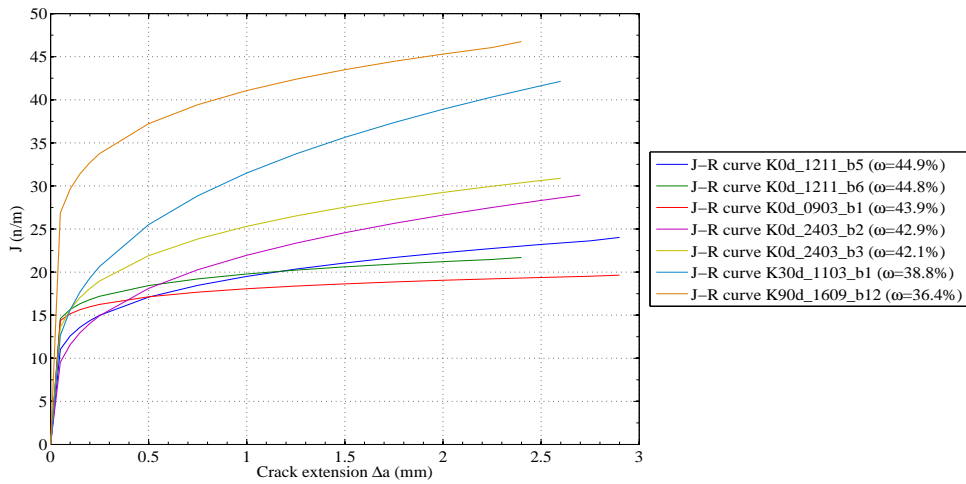


Figure 6.25: J-R curve approximation for the kaolin tests calculated in the range  $0 - \Delta a_{max}$

K0d\_0903.b1. The gradient of the straight line is equal to  $16.86 = M\sigma_Y S$ , which gave  $M$  equal to 10.22. Substituting it in the equation  $J = M\sigma_Y \Delta a$  it was possible to calculate a blunting line similar to that proposed for metals in the ASTM:E1820-15 (2015) (Figure 6.27). Repeating the procedure for the remaining tests, different values of  $M$  were calculated (Table 6.4).

Plotting  $M$  in relation to the moisture content the trend varied following a nonlinear curve.  $M$  was influenced by the moisture content of the clay beams. Differently from

Test No.	Moisture content $\omega$ (%)	$M$	$J_Q$ (N/m)
K0d_1211_b5	44.9	15.18	16.40
K0d_1211_b6	44.8	18.18	17.94
K0d_0903_b1	43.9	10.22	17.01
K0d_2403_b2	42.9	11.42	16.16
K0d_2403_b3	42.1	11.20	20.88
K30d_1103_b1	38.8	6.68	23.22
K90d_1609_b12	36.4	6.07	35.47

Table 6.4: Fracture parameters related to the slope of the blunting line and the proposed fracture toughness

metals which presented only one constant value for  $M$ , clay presented an  $M$  parameter that diminished with the decrease of water inside the soil.  $M$  had a value equal to 6.68 in the sample with  $\omega = 38.8$  %, then  $M$  increased to 11.42 for  $\omega = 42.9$  % and in the end increased to 18.18 for  $\omega = 44.8$  % (Figure 6.28).

A different approximation line was also considered in order to have a better relationship between  $\delta_t$  and the J-integral. In many tests the points seemed to follow a parabolic trend suggesting a different approximation to that adopted in the case of metals. However the parabola followed by the data points was caused by the method

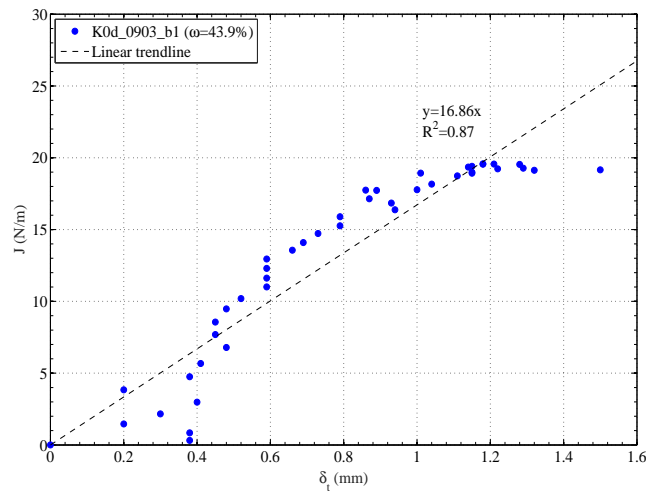


Figure 6.26:  $J$ - $\delta_t$  relationship and best linear approximation for the test K0d\_0903\_b1 ( $\omega = 43.9$  %)

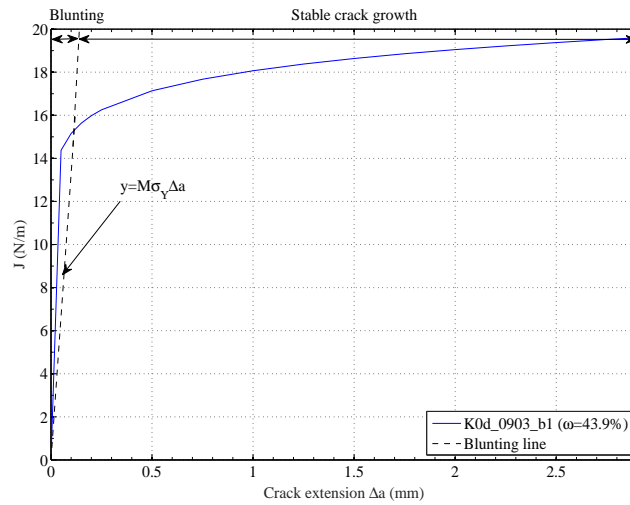


Figure 6.27: Blunting line drawn in relation to the R-curve for the test K0d\_0903\_b1 ( $\omega = 43.9\%$ )

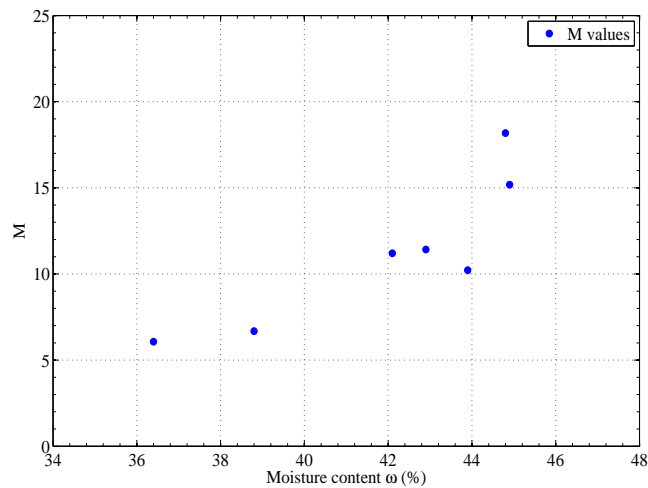


Figure 6.28: Variation of the parameter  $M$  in relation to the moisture content

of analysis: at the beginning of the test the apparent crack growth related to the notch blunting was difficult to detect. For this reason, the data found should have been more scattered compared to the actual trend. To avoid any incorrect estimate, the points at the beginning of the test were neglected during the calculation of  $M$ . The value of  $M$  was then calculated as the gradient of the linear approximation curve with the exclusion of the data at the beginning of the test where the crack was not visible. In this manner, the value of  $M$  is underestimated with respect to

the real values.

The next step in the calculation of the fracture toughness was represented by drawing an exclusion line parallel to the initial blunting line which intersected the abscissa 0.15 mm. A second exclusion line was plotted at the intersection with the abscissa 1.5 mm. The area in between these two lines defined the points taken in consideration during the calculation of the fracture toughness  $J_{Ic}$ . The last exclusion line was drawn at the offset value of 0.2 mm. The intersection between the regression line with the exclusion line passing at 0.2 mm identified the values of  $J_Q$  (Figure 6.29). The subscript  $Q$  indicates a provisional value which has to meet some validity requirements to be considered the final value.

In the case of clays the abscissas at which the exclusion lines were drawn were not modified from those used for metals. According to Janssen et al. (2002) the 0.15 mm exclusion line is chosen to guarantee a crack measuring at least 0.15 mm. Such crack length can be measured precisely. Instead, 1.5 mm is taken as a limit to ensure that the crack extension is less than 6 % of the remaining resistant ligament. These limits can also be used in the case of clay beams.

The provisional fracture toughness are reported in the Table 6.4 and plotted in Figure 6.30 in relation to the moisture content. Similarly to the  $M$  values, they varied in a nonlinear manner and decreased with the increase of the moisture content. But more data are necessary to determine a precise trend of behaviour.

Two requirements had to be met (ASTM:E1820-15 (2015)) to consider the provisional fracture toughness as the plane-strain fracture toughness. The first requirement was related to the minimum thickness that is allowing the crack growth under plane strain, while the second defined the minimum ligament length necessary to prevent the yielding of the section:

$$\begin{aligned} B &> 10J_Q/\sigma_Y \\ b_0 &> 10J_Q/\sigma_Y \end{aligned} \tag{6.8}$$

These two empirical requirements were calculated on the results found in tests on steels. For that, they cannot be used in the case of wet clays. However, the requirements were satisfied for the analysed beams with the lowest moisture contents.

For the state of the research, the provisional fracture toughness  $J_Q$  was considered

the final value which characterised the tensile behaviour of kaolin beams.

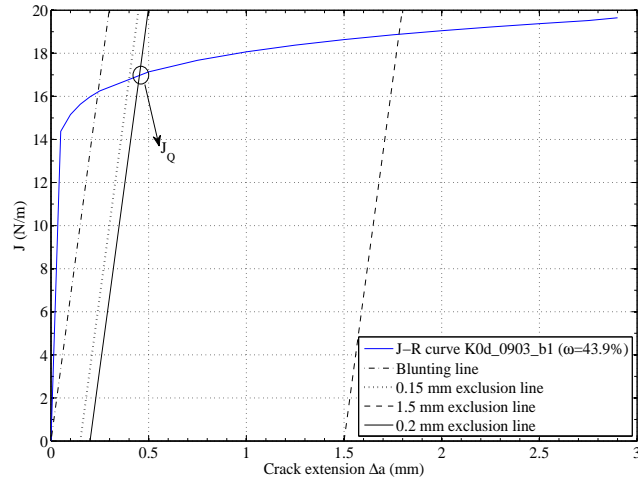


Figure 6.29: Graphic construction to determine  $J_Q$  (N/m) for the test K0d\_0903\_b1 ( $\omega = 43.9\%$ )

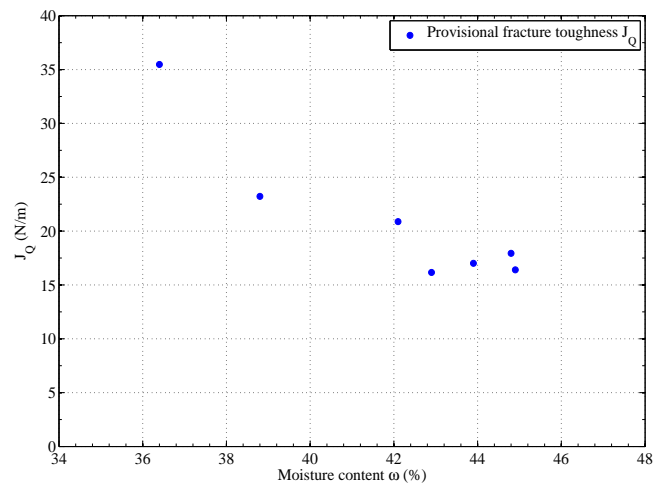


Figure 6.30: Provisional fracture toughness  $J_Q$  in relation to the variation of the moisture content

## 6.4 Summary

The analysis showed that in wet beams the fracture and subsequently the collapse happened after the beam underwent significant deformations. Before the development of the crack the notch blunted at the tip. The notch blunting was especially

influenced by the clay moisture content. GeoPIV confirmed the ductile behaviour of wet beams in which the notch initially deformed and then a crack formed.

The fracture analysis on the beams tested in t3-point bending also suggested that the crack formation was not a constant process as the strain was applied. The process was similar to raveling in which one part reached failure and a crack initiated. As soon as the next part reached the failing condition the crack extended further. This process was repeated until the beam failed by crack propagation.

The fracture analysis shows that less energy was required to break samples with a moisture content close to the optimum (low CTOA). Ductile samples allowed more deformations and required more energy to reach fracture (high CTOA).

A provisional value of fracture toughness was then calculated by applying the standard procedure adopted for metals. With appropriate modifications the procedure seemed to be suitable also for the case of wet clay fracture.

Both the fracture toughness and the crack tip parameters show that a moisture content close to the optimum represents the worst condition for clays overlying cavities. The resistance to crack propagation  $J_Q$  is high (or CTOA is low) when clays have a moisture content near the optimum and they can only sustain low deformations, leading to sudden collapse. Instead wet clays undergo fracture easily but the failure occurs after clays undergo large deformations before cracking to failure, providing some indication of the critical condition.

To conclude, clays characterised by a moisture content close to the optimum represent a danger for their sudden collapse. The design using clays with such moisture contents requires larger safety factor, despite the clay ability to sustain higher loads. Instead, clays with  $\omega/\omega_{OMC} > 1.2$  (in the kaolin case  $\omega > 42\%$ ) showed a ductile behaviour in which failure is preceded by large deformations. This suggested the possibility to design using reduced safety factors.

## Chapter 7

# Conclusions

The aim of this research was to investigate the fracture behaviour of clayey soils in tensile conditions and how this is affected by varying the moisture content and plasticity index. The findings showed trends of behaviour that can be used in the future to develop a sinkhole prediction model.

### 7.1 Main findings

The main results found from the laboratory testing can be summarised as follows:

- few data were reported in literature regarding the geotechnical characteristics of the fined grained soils involved in the formation of sinkholes. Generally mixtures of clay and sand or silt were involved in collapses for lowering of the water table. Dimensions of sinkholes were usually small which can be explained by the small depth at which the clay layers were placed and by the small height of the clay layers.
- the tensile strength was dependent on the moisture content of the clay. The relationship between the tensile strength and the moisture content followed a nonlinear curve in which the tensile strength diminished with the increase of moisture content. The maximum tensile strength was recorded for moisture contents slightly below the OMC.

- the plasticity index affected the tensile strength. An increase of plasticity index produced a corresponding increase of the maximum tensile strength sustained by the samples. Moisture content was more important for the determination of the clay fracture behaviour.
- the flexural strength determined during bending tests was affected by the moisture content. Assuming valid the linear-elastic conditions, the flexural strength diminished with the increase of moisture content. The data found from the bending tests were in agreement with those determined from the direct tensile tests.
- wet clays allowed the development of large deformations before collapsing. Before crack propagation, the beam notch underwent large deformations without any propagation of the crack. This behaviour gradually disappeared moving towards drier samples.
- the crack propagation was not constant during the beam bending but it followed a raveling process, in which the clay height failed in stages.
- the fracture process in clays could be studied by applying nonlinear fracture theory. Corrections to the standard procedure for metals were required to find appropriate fracture coefficients in clays.

## 7.2 Potential use in design

With the increase in the number of dropout sinkholes appeared in the last 30 years, the determination of a predictive method has become more pressing. However, dropout sinkholes are complex phenomena and they started to be studied only recently. Geophysical methods can be used to determine the position of underground cavities. McCann et al. (1987) suggested different methods to use for the determination of the cavities location: seismic, resistivity, gravity, magnetic and electromagnetic methods. As reported in Chapter 1, once the void is detected, the characteristics of the soils overlying the cavity are of vital importance for the study of dropout sinkholes. For this reason, the results of this investigation can be used

for a better understanding of the clay strata behaviour and will be helpful in the future for a sinkhole predictive method.

The analysis of previous sinkhole events pointed out that dropout sinkholes usually form in clayey layers of height  $< 15$  m, located at depth  $< 20$  m, due to a lowering of the water table. Relatively thin heights of clay layer confirm the possible failure through crack formation, when the arching process cannot form.

The water table lowering affects the soil behaviour when the clay spans over a cavity. The water inside the underground void sustained the roof of the cavity. When the water table is lowered, it causes bending in the soil roof and the passage of the soil from a wet to a dry condition. From the test results in clays, dry conditions represent a more dangerous situation in clays spanning over cavities. Even though the tensile strength of clays on the dry side of optimum is high, the beam collapse happens without any deformation in the most catastrophic manner (brittle collapse). When the clay strata are characterised by a high moisture content ( $\omega/\omega_{OMC} > 1.2$ ) the beam collapse is a slow process. Wet clays showed a lower tensile strength and fracture toughness than those with a moisture content close to the optimum. However, upon fracture initiation, wet clays could undergo large deformation before failure. The ability of the clay beam to deform when it is in wet conditions can explain why sinkholes usually happen some time after the rainfall event. As the clay gets wet and starts to bend, some energy is spent by the soil to deform. Similarly to the initial notch blunting, the clay strata deform and then the fracture process starts. This slow process of strata deformation and consequent dropout sinkhole formation can explain why in February 2014 many sinkholes occurred across UK (British Geological Survey, Chapter 1), when despite heavy rainfall between December 2013 and January 2014, dropout sinkholes mostly started to appear in the second half of the following month. The wet clayey soils which cover many areas of the UK initially deformed slowly, reaching the collapse a few weeks after the rain event. This means that clay layers overlying cavities need to be monitored after heavy rainfall.

The mode with which the crack develops suggests a mode of proceeding similar to soil raveling. The clay height of the beam failed in stages with a crack propagation through steps. A more instantaneous crack formation, without many steps, was seen

in clay having a lower moisture content. This behaviour confirms a more dangerous situation when the clay is dry. The same procedure is also applicable to clay strata that lead to sinkhole formation.

The results determined from the direct tensile and bending tests confirmed that the plasticity index is less useful than the moisture content and its relationship with the optimum moisture content. Both the tests gave data that had a similar behaviour despite their varied plasticity index. The tensile and the flexural strength follow a nonlinear trend of behaviour in relation to the moisture content. With the increase of the moisture content the ultimate tensile strength decreases. But, the increase of moisture content was not always reflected in a more plastic behaviour. This can be seen as the ability of the clay to deform plastically under tensile stresses (ductility). Clays as kaolin show a high strain at the moment of fracture, while clays similar to London clay have a lower strain at the moment of fracture. Layers of clay spanning over cavities that present a low ductility for the same moisture content deform less than clays with a higher ductility. The ductility and the moisture content affect the ability of the clay to deform in tensile condition and consequently determine the instantaneous or slow appearance of the dropout sinkhole.

In conclusion, the results found in this investigation are not directly applied to a predictive method of sinkhole appearance. But, they can be used to understand the behaviour of the clay strata spanning over cavities. Once the voids are detected into the ground, the main concern for sinkhole prediction is to determine the behaviour of the soil layers overlying the cavity. This investigation shows that three geotechnical parameters are important in the determination of the tensile behaviour of clayey soils: ductility, moisture content and optimum moisture content. These parameters determine the collapse behaviour of the clay layers, with large deformation or in a less plastic manner with an almost instantaneous crack. The plasticity index resulted less important in the determination of the tensile behaviour of clays.

### 7.3 Suggestions for future research

This research highlighted the importance of studying fine-grained soils under tensile loads. This area is especially critical for the study of sinkhole formation in particular for the study of the soil covering the underground cavities.

Many aspects of the research can be developed for a better understanding of the behaviour of cracked clayey soils. A large part of this research was based on the study of digital images recorded during tests on clay beams, limiting the study to fractures visible on the beam surface. But crack development takes place across all the sample width. Thus, the analysis of the fracture mechanism along the sample width is recommended to determine if the behaviour found in the surface is followed also through the sample or if the cracking process is different. This would require testing in a CT scanner or 3D scanner, which would provide a valuable insight into the 3D nature of fracture mechanisms.

During this research clayey layers overlying cavities are simplified using square beams. However, the use of different geometries, like deep beams or thin plates, is recommended to represent a problem more similar to real sinkholes. Bending in beams with different heights could also confirm the gradual failure of clays through a raveling process, as found during the bending tests, and the arch formation.

This study focused on the laboratory experiments conducted. However, in order to create an assessment of sinkhole stability a numerical simulation is required. The numerical model needs to be able to simulate collapse modes in clayey soils and can be validated against the results of this study. While recent numerical models for sinkhole formation were investigated (Helm et al., 2013; Tao et al., 2015; Jia et al., 2015), few studies have concentrated on crack propagation (i. e. Amarasiri et al. (2011) related to 3-point bending tests). Simulations of sinkholes which include crack formation will provide a more comprehensive understanding of sinkhole formation.

Wetting and drying cycles are usual phases of the everyday weather. In fine grained soils the continuous change of behaviour between wet and dry conditions affects soil stiffness. A gradual softening of cohesive soil was found by Tharp (1999), Take

(2003), Take and Bolton (2011). The continuous change from brittle to ductile collapse determines the creation of tensile cracks and a gradual reduction of soil resistance due to the accumulation of plastic strain. These phenomena affect the fracture behaviour of the clay layers.

Finally, this research only studied cracks formed in tensile conditions. However mode I fracture is not the only possible fracture mode of cracking that can take place in clay layers spanning over cavities. Mixed mode cracks can form where the clay layer stops deforming under bending. Investigations on mode II or mixed mode cracks are recommended to encompass all the possible factors which affect sinkhole formation. Interactions between developing cracks can affect the deformation and speed with which the sinkhole appears and this would produce a more comprehensive review of fracture behaviour.

# References

- Ahmad, S., Alnuaim, A. M. and Naggar, M. H. E. (2015), Dynamic shear modulus of kaolin-silt clay using a novel technique, *in* 'Deformation characteristics of geomaterials. Proceedings of the 6th international symposium of deformation characteristics of geomaterials', pp. 331–341.
- Ajaz, A. and Parry, R. H. G. (1975), 'Stress-strain behaviour of two compacted clays in tension and compression', *Géotechnique* **25**(3), 495–512.
- Amarasiri, A. L., Costa, S. and Kodikara, J. (2011), 'Determination of cohesive properties for mode I fracture from compacted clay beams', *Canadian Geotechnical Journal* **38**, 1163–1173.
- Anderson, T. L. (2005), *Fracture Mechanics. Fundamentals and Applications*, Taylor & Francis.
- Andrejchuk, V. (2002), 'Collapse above the world's largest potash mine (Ural, Russia)', *International Journal of Speleology* **31**(1), 137–158.
- ASTM:E1820-15 (2015), 'Standard test method for measurement of fracture toughness'.
- ASTM:E399-12 (2013), 'Standard test method for linear-elastic plane-strain fracture toughness  $K_{IC}$  of metallic materials'.
- ASTM:E8/E8M-15a (2015), 'Standard test method for tension testing of metallic materials'.

- Beaupre, M. and Schroeder, J. (1989), Collapse sinkhole at the inlet tunnel of a powerhouse, Pont-Rouge, Quebec, *in* B. F. Beck, ed., 'Engineering and Environmental Impacts of Sinkholes and Karst. Proceedings of the 3rd Multidisciplinary Conference on Sinkholes and Engineering and Environmental Impacts of Karst', pp. 83–87.
- Begley, J. A. and Landes, J. D. (1972), 'The J-integral as a fracture criterion', *ASTM STP 514* pp. 1–20.
- Bishop, A. W. (1959), 'The principle of effective stress', *Teknisk Ukeblad. Norwegian Geotechnical Institute* **106**(39), 859–863.
- Bloomberg, D., Upchurch, B., Hayden, M. L. and Williams, R. C. (1988), 'Cone-penetrometer exploration of sinkholes: stratigraphy and soil properties', *Environmental Geology and Water Sciences* **12**(2), 99–105.
- Boatwright, B. A. and Allman, D. W. (1975), 'The occurrence and development of guest sink, Hernando County, Florida', *Groundwater* **13**(4), 372–375.
- Burdon, D. J. (1987), Some ancient dolines in the karst of Ireland, *in* B. F. Beck and W. L. Wilson, eds, 'Karst Hydrogeology: Engineering and Environmental Applications. Proceedings of the 2nd Multidisciplinary Conference on Sinkholes and Engineering and Environmental Impacts of Karst', pp. 65–71.
- Chandler, H. W. (1984), 'The use of non-linear mechanics to study the fracture properties of soils', *Journal of Agricultural Engineering Research* **29**, 321–327.
- Charles, W. W. and Menzies, B. (2007), *Advanced unsaturated soil mechanics and engineering*, Tylor & Francis. London and New York.
- Chenu, C. and Guérif, J. (1998), 'Mechanical strength of clay minerals as influenced by an adsorbed polysaccharide', *Soil Science Society Of America Journal* **55**, 1076–1080.
- Cooper, A. H. (1995), Subsidence hazards due to the dissolution of Permian gypsum in England: Investigation and remediation, *in* B. F. Beck, ed., 'Karst Geohazards:

- Engineering and Environmental problems in Karst. Proceedings of the 5th Multidisciplinary Conference on Sinkholes and Engineering and Environmental Impacts of Karst', pp. 23–29.
- Cooper, A. H. and Saunders, J. M. (2002), 'Road and bridge construction across gypsum karst in England', *Engineering Geology* **65**, 217–223.
- Delage, P., Cui, Y. J. and Antoine, P. (2005), Geotechnical problems related with loess deposits in Northern France, *in* 'Proceedings of the International Conference on Problematic Soils', pp. 517–540.
- Divya, P. V., Viswanadham, B. V. S. and Gourc, J. P. (2014), 'Evaluation of tensile strength-strain characteristics of fiber-reinforced soil through laboratory tests', *Journal of Materials in Civil Engineering* **26**(1), 14–23.
- Donnelly, L. J. (2008), 'Subsidence and associated ground movements on the Pennines, northern England', *Quarterly Journal of Engineering Geology and Hydrogeology* **41**, 315–332.
- Dougherty, P. H. and Perlow, M. (1987), The Macungie sinkhole, Lehigh Valley, Pennsylvania: cause and repair, *in* B. F. Beck and W. L. Wilson, eds, 'Karst Hydrogeology: Engineering and Environmental Applications. Proceedings of the 2nd Multidisciplinary Conference on Sinkholes and Engineering and Environmental Impacts of Karst', pp. 425–435.
- Ewalds, H. L. and Wanhill, R. J. H. (1984), *Fracture Mechanics*, Edward Arnold.
- Fang, H. Y. and Hirst, T. J. (1973), 'A method for determining the strength parameters of soils, presented at the 52d annual meeting of Highway Research Board, January 1973', *Fritz Laboratory Reports* .
- Farrell, D. A., Greacen, E. L. and Larson, W. E. (1967), 'The effect of water content on axial strain in a loam soil under tension and compression', *Soil Science Society of America Proceedings* **31**, 445–450.
- Fredlund, D. G., Fredlund, M. D. and Rahardjo, J. (2012), *Soil mechanics for unsaturated soils in engineering practice*, J. Wiley and Sons, Inc., New York, N.Y.

- Fredlund, D. G. and Rahardjo, H. (1993), *Soil mechanics for unsaturated soils*, J. Wiley and Sons.
- Gao, Y., Luo, W., Jiang, X., Lei, M. and Dai, J. (2013), Investigations of large scale sinkhole collapses, Laibin, Guangxi, China, *in* L. Land, D. H. Doctor and J. Stephenson, eds, 'Proceedings of the 13th Multidisciplinary Conference on Sinkholes and Engineering and Environmental Impacts of Karst', pp. 327–331.
- Glendinning, S., Hughes, P., Helm, P., Chambers, J., Mendes, J., Gunn, D., Wilkinson, P. and Uhlemann, S. (2014), 'Construction, management and maintenance of embankments used for road and rail infrastructure: implications of weather induced pore water pressures', *Acta Geotechnica* **9**, 799–816.
- Goehring, R. L. and Sayed, S. M. (1989), Mann Road sinkhole stabilization: A case history, *in* B. F. Beck, ed., 'Engineering and Environmental Impacts of Sinkholes and Karst. Proceedings of the 3rd Multidisciplinary Conference on Sinkholes and Engineering and Environmental Impacts of Karst', pp. 319–325.
- Gordon, M. M. (1987), The sinkhole repair: The bottom line, *in* B. F. Beck and W. L. Wilson, eds, 'Karst Hydrogeology: Engineering and Environmental Applications. Proceedings of the 2nd Multidisciplinary Conference on Sinkholes and Engineering and Environmental Impacts of Karst'.
- Griffith, A. A. (1920), 'The phenomena of rupture and flow in solids', *Philosophical Transactions* **221**(Series A), 163–198.
- Gutierrez, M. (2012), Geotechnical investigation report for repair of sinkholes on embankment slope on route 105, PM R2.55, Technical report, Department of Transportation Division of Engineering Services.
- Hallett, P. D. and Newson, T. A. (2001), 'A simple fracture mechanics approach for assessing ductile crack growth in soil', *Soil Science Society of America Journal* **65**, 1083–1088.
- Hallett, P. D. and Newson, T. A. (2005), 'Describing soil crack formation using elastic-plastic fracture mechanics', *European Journal of Soil Science* **56**, 31–38.

- He, K., Liu, C. and Wang, S. (2003), 'Karst collapse related to over-pumping and a criterion for its stability', *Environmental Geology* **43**, 720–724.
- Helm, P. R., Davie, C. T. and Glendinning, S. (2013), 'Numerical modelling of shallow abandoned mine working subsidence affecting transport infrastructure', *Engineering Geology* **154**, 6–19.
- Hughes, P. N., Mendes, J., Parkin, G., Toll, D. G., Gallipoli, D. and Miller, P. E. (2009), 'Full-scale testing to assess climate effects on embankments', *Proceedings of the Institution of Civil Engineers: Engineering Sustainability* **162**(2), 67–69.
- Indraratna, B. and Lasek, G. (1996), 'Laboratory evaluation of the load-deflection behaviour of clay beams reinforced with galvanised wire netting', *Geotextiles and Geomembranes* **14**, 555–573.
- Irwin, G. R. (1956), Onset of fast crack propagation in high strength steel and aluminum alloys, in 'Sagamore Research Conference Proceedings', Vol. 2, pp. 289–305.
- Jammal, S. E. (1984), Maturation of the Winter Park sinkhole, in B. F. Beck, ed., 'Sinkholes: Their Geology, Engineering and Environmental Impact. Proceedings of the 1st Multidisciplinary Conference on Sinkholes and Engineering and Environmental Impacts of Karst', pp. 363–369.
- Jammal, S. E. (1986), The Winter Park sinkhole and central Florida sinkhole type subsidence, in 'Proceedings of the 3rd International Symposium on Land Subsidence', number 151, pp. 585–594.
- Janssen, M., Zuidema, J. and Wanhill, R. J. H. (2002), *Fracture Mechanics*, Spon Press.
- Jia, L., Meng, Y. and Liu, Z. G. L. (2015), Numerical simulation of karst soil cave evolution, in 'NCKRI Symposium 5. Proceedings of the 14th Multidisciplinary Conference on Sinkholes and the Engineering and Environmental Impacts of Karst', pp. 493–500.

- Kiernan, K. (1989), Sinkhole hazards in Tasmania, *in* B. F. Beck, ed., 'Engineering and Environmental Impacts of Sinkholes and Karst. Proceedings of the 3rd Multidisciplinary Conference on Sinkholes and Engineering and Environmental Impacts of Karst', pp. 123–128.
- Kiflu, H., Kruse, S. and Wightman, M. (2013), Statistical analysis of GPR and SPT methods for sinkhole investigation in covered karst terrain, west-central Florida, USA, *in* L. Land, D. H. Doctor and J. Stephenson, eds, 'Proceedings of the 13th Multidisciplinary Conference on Sinkholes and Engineering and Environmental Impacts of Karst', pp. 247–253.
- Klimchouk, A. and Andrejchuk, V. (2002), 'Karst breakdown mechanisms from observations in the gypsum caves of the Western Ukraine: Implications for subsidence hazard assessment', *International Journal of Speleology* **31**(1), 55–88.
- Lakshmikantha, M. R., Prat, P. C., Tapia, J. and Ledesma, A. (2008), Effect of moisture content on tensile strength and fracture toughness of a silty soil, *in* C. Press, ed., 'Proceedings of the first European Conference on Unsaturated soils', pp. 405–409.
- Lamoreaux, P. E. and Newton, J. G. (1986), 'Catastrophic subsidence: an environmental hazard, Shelby County, Alabama', *Environmental Geology and Water Sciences* **8**(2), 25–40.
- Lei, M., Jiang, X., Guan, Z. and Gao, Y. (2013), Emergency investigation of extremely large sinkholes, Maohe, Guangxi, China, *in* L. Land, D. H. Doctor and J. Stephenson, eds, 'Proceedings of the 13th Multidisciplinary Conference on Sinkholes and Engineering and Environmental Impacts of Karst', pp. 293–298.
- Lu, N., Godt, J. and Wu, D. (2010), 'A closed-form equation for effective stress in variably saturated soil', *Water Resources Research* **46**(5).
- Lu, N., Sture, T. H. and Likos, W. J. (2009), 'Tensile strength of unsaturated sand', *Journal of Engineering Mechanics* pp. 1410–1419.

- Martin, A. D. (1995), Maryland Route 31 sinkhole, *in* B. F. Beck, ed., 'Karst Geohazards: Engineering and Environmental problems in Karst. Proceedings of the 5th Multidisciplinary Conference on Sinkholes and Engineering and Environmental Impacts of Karst', pp. 319–334.
- Mavroulidou, M., Zhang, X., Gunn, M. J. and Cabarkapa, Z. (2011), An investigation of the effects of cementation and suction on lime treated london clay, *in* 'Unsaturated soils: Theory and practice', Jotisankasa, Sawangsuriya, Sorlump and Mairaing, pp. 527–531.
- Mavroulidou, M., Zhang, X., Kichou, Z. and Gunn, M. (2013), Hydro-mechanical properties of lime-treated London clay, *in* 'Proceedings of the 18th International Conference on Soil Mechanics and Geotechnical Engineering', pp. 1151–1154.
- McCann, D. M., Jackson, P. D. and Culshaw, M. G. (1987), 'The use of geophysical surveying methods in the detection of natural cavities and mineshafts', *Quarterly Journal of Engineering Geology and Hydrogeology* **20**, 59–73.
- McDowell, P. (1989), Ground subsidence associated with doline formation in chalk areas of southern England, *in* B. F. Beck, ed., 'Engineering and Environmental Impacts of Sinkholes and Karst. Proceedings of the 3rd Multidisciplinary Conference on Sinkholes and Engineering and Environmental Impacts of Karst', pp. 129–134.
- Mellett, J. S. and Maccarillo, B. J. (1995), A model for sinkhole formation on interstate and limited access highways, with suggestions on remediation, *in* B. F. Beck, ed., 'Karst Geohazards: Engineering and Environmental problems in Karst. Proceedings of the 5th Multidisciplinary Conference on Sinkholes and Engineering and Environmental Impacts of Karst', pp. 335–339.
- Murdoch, L. C. (1992), 'Hydraulic fracturing of soil during laboratory experiments. part 1. methods and observations', *Géotechnique* **43**, 255–265.
- Neal, J. T. and Myers, R. E. (1995), Salt dissolution sinkhole at the Weeks Island, Louisiana, strategic petroleum storage site, *in* B. F. Beck, ed., 'Karst Geohazards:

- Engineering and Environmental problems in Karst. Proceedings of the 5th Multidisciplinary Conference on Sinkholes and Engineering and Environmental Impacts of Karst', pp. 61–65.
- Newton, J. (1984), Review of induced sinkhole development, *in* B. F. Beck, ed., 'Sinkholes: Their Geology, Engineering and Environmental Impact. Proceedings of the 1st Multidisciplinary Conference on Sinkholes and Engineering and Environmental Impacts of Karst', pp. 3–9.
- Nichols, J. R. and Grismer, M. E. (1997), *Measurement of fracture mechanics parameters in silty-clay soils*, Vol. 162, pp. 309–322.
- Perera, Y. Y., Padilla, J. M. and Fredlund, D. G. (2004), Determination of soil-water characteristic curves using the Fredlund SWCC device, *in* 'Presentation material for mining & waste management short course, Vail, Co'.
- Plé, O., Minicacci, A., Gourc, J. P. and Camp, S. (2012), 'Flexural behaviour of a clay layer: experimental and numerical study', *Canadian Geotechnical Journal* **49**, 485–493.
- Price, D. J. (1984), Karst progression, *in* B. F. Beck, ed., 'Sinkholes: Their Geology, Engineering and Environmental Impact. Proceedings of the 1st Multidisciplinary Conference on Sinkholes and Engineering and Environmental Impacts of Karst', pp. 17–22.
- Pusey, J. T. and Caccese, J. M. (2013), Geotechnical case history for sinkhole investigation and stabilization methods along a high pressure petroleum pipeline, *in* L. Land, D. H. Doctor and J. Stephenson, eds, 'Proceedings of the 13th Multidisciplinary Conference on Sinkholes and Engineering and Environmental Impacts of Karst', pp. 13–21.
- Raghu, D., Lifrieri, J. J. and Rhyner, F. C. (1984), Use of percussion probes for the design and construction of foundations in and on carbonate formations, *in* B. F. Beck, ed., 'Sinkholes: Their Geology, Engineering and Environmental Impact. Proceedings of the 1st Multidisciplinary Conference on Sinkholes and Engineering and Environmental Impacts of Karst', pp. 171–176.

- Rice, J. R. (1968), 'A path independent integral and the approximate analysis of strain concentration by notches and cracks', *Journal of Applied Mechanics* **35**, 379–386.
- Scarborough, J. A. (1995), Risk and reward: pipes and sinkholes in East Tennessee, *in* B. F. Beck, ed., 'Karst Geohazards: Engineering and Environmental problems in Karst. Proceedings of the 5th Multidisciplinary Conference on Sinkholes and Engineering and Environmental Impacts of Karst', pp. 349–354.
- Scarborough, J. A., Ben-Hassine, J., Ketelle, R. H., Kane, W. F. and Drumm, E. C. (1989), Surface deformation of residual soil over cavitose bedrock, *in* B. F. Beck, ed., 'Engineering and Environmental Impacts of Sinkholes and Karst. Proceedings of the 3rd Multidisciplinary Conference on Sinkholes and Engineering and Environmental Impacts of Karst', pp. 143–149.
- Sivakumar, V., Anderson, C., Solan, B., Rankin, B. and Mackinnon, P. (2015), Influence of testing on permeability of compacted fine soils, *in* 'ICE Proceedings. Geotechnical Engineering', Vol. 168, pp. 422–438.
- Soilmoisture (2008), '5 Bar Ceramic Plate Extractor. operating instructions'.
- Stelmack, M. J., Sheridan, T. and Beck, B. F. (1995), Cap reinforcement over a sinkhole as part of a landfill closure, *in* B. F. Beck, ed., 'Karst Geohazards: Engineering and Environmental problems in Karst. Proceedings of the 5th Multidisciplinary Conference on Sinkholes and Engineering and Environmental Impacts of Karst', pp. 389–395.
- Stirling, R. A., Hughes, P., Davie, C. T. and Glendinning, S. (2015), 'Tensile behaviour of unsaturated compacted clay soil - A direct assessment method', *Applied Clay Science* **112-113**, 123–133.
- Take, W. A. (2003), The influence of seasonal moisture cycles on clay slopes, PhD thesis, University of Cambridge.
- Take, W. A. and Bolton, M. D. (2011), 'Seasonal ratcheting and softening in clay slopes, leading to first-time failure', *Géotechnique* **61**(9), 757–769.

- Tang, C., Pei, X., Wang, D., Shi, B. and Li, J. (2015), 'Tensile strength of compacted clayey soil', *Journal of Geotechnical and Geoenvironmental Engineering* **141**(4), 65–75.
- Tao, X., Ye, M., Wang, D., Castro, R. P., Wang, X. and Zhao, J. (2015), Experimental and numerical investigation of sinkhole development and collapse in Central Florida, in 'NCKRI Symposium 5. Proceedings of the 14th Multidisciplinary Conference on Sinkholes and the Engineering and Environmental Impacts of Karst', pp. 501–506.
- Tharp, T. M. (1999), 'Mechanics of upward propagation of cover-collapse sinkholes', *Engineering Geology* **52**, 23–33.
- Thusyanthan, N. I., Take, W. A., Madabhushi, S. P. G. and Bolton, M. D. (2007), 'Crack initiation in clay observed in beam bending', *Géotechnique* **57**(7), 581–594.
- Toll, D. G., Mendes, J., Gallipoli, D., Glendinning, S. and Hughes, P. N. (2012), 'Investigating the impacts of climate change on slopes: field measurements', *Geological Society* **26**, 151–161.
- Towner, G. D. (1987), 'The mechanics of cracking of drying clay', *Journal of Agricultural Engineering Research* **36**, 115–124.
- Trabelsi, H., Jamei, M., Zenzri, H. and Olivella, S. (2012), 'Crack patterns in clayey soils: Experiments and modeling', *International Journal for Numerical and Analytical Methods in Geomechanics* **36**, 1410–1433.
- Tschebotarioff, G. P., Ward, E. R. and DePhilippe, A. A. (1953), The tensile strength of disturbed and recompacted soils, in 'Proceedings of the 3rd International Conference on Soil Mechanics and Foundation Engineering', Vol. 1, pp. 207–210.
- Upchurch, S. B., Dobecki, T. L., Scott, T. M., Meiggs, S. H., Fratesi, S. E. and Alfieri, M. C. (2013), Development of sinkholes in a thickly covered karst terrane, in L. Land, D. H. Doctor and J. Stephenson, eds, 'Proceedings of the 13th Multi-

- disciplinary Conference on Sinkholes and Engineering and Environmental Impacts of Karst', pp. 273–277.
- Vattano, M., Maggio, C. D., Madonia, G., Parise, M., Lollino, P. and Bonamini, M. (2013), Examples of anthropogenic sinkholes in Sicily and comparison with similar phenomena in southern Italy, *in* L. Land, D. H. Doctor and J. Stephenson, eds, 'Proceedings of the 13th Multidisciplinary Conference on Sinkholes and Engineering and Environmental Impacts of Karst', pp. 263–271.
- Viswanadham, B. V. S., Jha, B. K. and Pawar, S. N. (2010), 'Experimental study on flexural testing of compacted soil beams', *Journal of Materials in Civil Engineering* **22**, 460–468.
- Waltham, T., Bell, F. and Culshaw, M. (2005), *Sinkholes and subsidence. Karst and cavernous rocks in engineering construction*, Praxis Publishing, Chichester, UK.
- Wang, J., Zhu, J., Chiu, C. F. and Zhang, H. (2007a), 'Experimental study on fracture behaviour of a silty clay', *Geotechnical Testing Journal* **30**(4), 309–322.
- Wang, J., Zhu, J., Chiu, C. F. and Zhang, H. (2007b), 'Experimental study on fracture toughness and tensile strength of a clay', *Engineering Geology* **94**, 65–75.
- Weibull, W. (1951), 'A statistical distribution function of wide applicability', *Journal of Applied Mechanics* **18**, 293–305.
- Weiguo, X. and Guirong, Z. (1988), 'Mechanism and prevention of karst collapse near mine areas of china', *Environmental Geology and Water Sciences* **12**(1), 37–42.
- Wells, A. A. (1961), Unstable crack propagation in metals: cleavage and fast fracture, *in* 'Proceedings of the Crack Propagation Symposium', Vol. 1, pp. 210–230.
- White, D. J. (2002), An investigation into the behaviour of pressed-in piles, PhD thesis, University of Cambridge.
- Wilson, W. L. and Beck, B. F. (1992), 'Hydrogeologic factors affecting new sinkhole development in the Orlando area, Florida', *Groundwater* **30**(6), 918–930.

- Zeh, R. M. and Witt, K. J. (2007), The tensile strength of compacted clays as affected by suction and soil structure, *in* 'Experimental Unsaturated Soil Mechanics', Springer.

## Appendix A

# Historical cases database

<b>No.</b>	<b>Author</b>	<b>Place</b>	<b>Collapsed soil</b>	<b>Triggering factor</b>
1	Klimchouk and Andrejchuk (2002)	Ukraine	Kosovsky clay	Not found
2	Cooper and Saunders (2002)	Ripon, UK	Clay and silt	Not found
3	Weiguo and Guirong (1988)	Huai Nan, China	Residual clay (limestone)	Not found
4	He et al. (2003)	Guizhou Prov., China	Silty - sandy loam	Not found
5	Lamoreaux and Newton (1986)	Dry Valley, Shelby County, Alabama	Residual clay (Carbonate rocks)	Not found
6	Bloomberg et al. (1988)	Hillsborough County, Florida	Clayey silt	Not found
7	Andrejchuk (2002)	Ural Russia	Clay-marl sequence	Not found
8	Pusey and Caccese (2013)	Plymouth Meeting, Pennsylvania	Clayey soil	Not found
9	Kiflu et al. (2013)	West-central Florida	Sand, silty sand, sandy clay deposits (Quaternary sediments)	Not found
10	Vattano et al. (2013)	Sicily, south Italy	Sand and grey sandy clays	Not found
11	Upchurch et al. (2013)	Tampa Bay, Florida	Clayey sand	Not found
12	Upchurch et al. (2013)	Plant City, Hillsborough County, Florida	Clay and clayey sand	Heavy groundwater withdrawal

Table A.1: Database of the past sinkholes cases

No.	Author	Place	Collapsed soil	Triggering factor
13	Upchurch et al. (2013)	South east Hillsborough	Clayey sand	Pumpage
14	Lei et al. (2013)	Maohe village, Liuzhou, Guangxi, China	Colluvium clay, silty clay, rounded gravels, red clay	Heavy rainfall
15	Gao et al. (2013)	Laibin Guangxi, China	Silty clay, clay containing gravels, clay (Quaternary deposits)	Drought and then heavy rain
16	Boatwright and Allman (1975)	Guest sink, Hernando County, Florida	Soft sand and clayey sand	Well drilling
17	Wilson and Beck (1992)	Orlando area, Florida	Clayey Hawthorn group strata (Miocene clay)	Ground water table (GWT) lowering
18	Jammal (1986)	Winter Park, Florida	Clayey sands, with silt, shell phosphate and dolomite fragments (Hawthorn clay)	Aquifer withdrawal
19	Helm et al. (2013)	Dolphingstone, Scotland, UK	Boulder clay (sandy gravelly clay)	Mine collapse
20	Newton (1984)	South Carolina	Residual clay	Decline of the water table
21	Newton (1984)	Tampa, Florida	Residual clay	Decline of the water table
22	Newton (1984)	Alabama	Residual clay	Decline of the water table
23	Newton (1984)	Shelby County, Alabama	Residual clay	Decline of the water table
24	Newton (1984)	Alabama, Sylocanga	Residual clay	Decline of the water table
25	Newton (1984)	Hershey Valley, Pennsylvania	Residual clay	Decline of the water table

Table A.2: Database of the past sinkholes cases

No.	Author	Place	Collapsed soil	Triggering factor
26	Price (1984)	Florida	Sand, clay, sandy silty calcareous units (Hawthorn clay)	Not found
27	Raghu et al. (1984)	New Jersey	Residual clay	Not found
28	Jammal (1984)	Winter Park, Florida	Clayey sand with silt, shell, phosphate and dolomite fragments	Not found
29	Delage et al. (2005)	Northern France	Calcareous loess (silty sediments) with some clay	Wetting of unsaturated soil under load
30	Gutierrez (2012)	Los Angeles County	Silty and clayey sand	Not found
31	Burdon (1987)	Tynagh, Co. Galway, Ireland	Boulder clay	Not found
32	Burdon (1987)	Ballygaddy, Co. Offaly	Stony clay	Not found
33	Burdon (1987)	Ballyellin, Co. Carlow	Midlandian till	Not found
34	Gordon (1987)	Keystone Heights, Florida	Sandy clay and clay	Water percolation
35	Gordon (1987)	Gainesville, Florida	Sandy clay	Water percolation
36	Gordon (1987)	Gainesville, Florida	Sandy clay and clay	Not found
37	Dougherty and Perlow (1987)	Lehigh Valley, Pennsylvania	Organic clays, silts, silty sands, reworked residual soils	Not found
38	Beaupre and Schroeder (1989)	Pont-Rouge, Quebec	Clayey till	Not found

Table A.3: Database of the past sinkholes cases

No.	Author	Place	Collapsed soil	Triggering factor
39	McDowell (1989)	Summersdale, south England	Silty clay	Heavy rain after a hot and dry summer
40	Kiernan (1989)	Loatta area, North-centre Tasmania	Periglacial alluvial sediments	Heavy rain
41	Kiernan (1989)	Sassfras Creek Valley, centre-north Tasmania	Sandy-silty matrix	Deforestation
42	Goehring and Sayed (1989)	Orange County, Florida	Sandy silts, silts	Not found
43	Scarborough et al. (1989)	Oak Ridge, Tennessee	Residual silty clays	Not found
44	Cooper (1995)	Ripon, North Yorkshire, UK	Glacial and post-glacial deposits	Changes in water table
45	Cooper (1995)	Hell Kettles, south Darlington, UK	Not found	Water abstraction
46	Cooper (1995)	Cumbria, UK	Not found	Earthquake activity
47	Neal and Myers (1995)	Weeks Islands, Louisiana	Alluvial deposits	Collapse of underground mines
48	Martin (1995)	Roadway of Maryland route, Maryland	Residual soils (red clays, silty clays)	Not found
49	Mellet and Maccarillo (1995)	New Jersey	Not found	Not found

Table A.4: Database of the past sinkholes cases

<b>No.</b>	<b>Author</b>	<b>Place</b>	<b>Collapsed soil</b>	<b>Triggering factor</b>
50	Scarborough (1995)	Knoxville, Tennessee	Residual soils (reddish-brown silty clays)	Not found
51	Scarborough (1995)	Morristown, Tennessee	Residual soils (reddish-brown silty clays)	Not found
52	Scarborough (1995)	Johnson city, Tennessee	Reddish-brown silty clays overlain by brown clayey silt	Not found
53	Stelmack et al. (1995)	Landfill, Missouri	Silty clay	Not found

Table A.5: Database of the past sinkholes cases

No.	$H_t$	$H$	PI	Sand/silt?	Composition	Other	$\emptyset$	$d$	$H_1/\emptyset$	$H/\emptyset$
1	5-60	29.5-106.2	28	Not found	Montmorillonite ( $<38\%$ ), hydro-illite (25-30%)	$\omega=17-18\%$ , $\rho = 2.1 \text{ g/cm}^3$ , $n=35.6\%$ , $\gamma_d = 17.36 \text{ kN/m}^3$	3-5	2-5	1-20	5.9-35.4
2	$<8$	30	Not found	Not found	Not found	Not found	30	20	0.27	1
3	11-13	Not found	Not found	Not found	Not found	Not found	60	30	0.18-0.22	Not found
4	0.8-1.1	1-1.3	Not found	Not found	Not found	$\gamma =$ 16.4 – 18.6 kN/m <sup>3</sup> , $c = 6 - 18 \text{ kPa}$ , $\phi = 8.72 - 18.22^\circ$ , $K_{0,aver} = 0.65$	30x16.2	10	0.027- 0.068	0.033- 0.08
5	$>9.14$	9.14	Not found	Not found	Clay: chert debris	Not found	Not found	Not found	Not found	Not found
6	$2.0 \pm 0.6$	$19.9 \pm 4.7$	Med.	Organic content: 2.69%	Siliciclastic clay and silt	LL=153.0%, $\omega = 175.4\%$ , $G_s = 2.65$	Not found	Not found	Not found	Not found
7	50	235-425	Not found	Not found	Not found	Not found	40x80	$\approx 140$	0.63-1.25	2.94- 55.31

Table A.6: Soil properties of the past sinkhole cases

No.	$H_t$	$H$	PI	Sand/silt?	Composition	Other	$\emptyset$	$d$	$H_t/\emptyset$	$H/\emptyset$
8	21.3	21.3	Not found	Not found	Not found	3.3 m found in the bedrock	3	3	7.1	7.1
9	0-60	0-60	Not found	Not found	Not found	GWL=2.6 m	Not found	Not found	Not found	Not found
10	Not found	Not found	Not found	Not found	Microfossils	Not found	130x90	2.4	Not found	Not found
11	Not found	120	Not found	Not found	Not found	Not found	Not found	>30	Not found	Not found
12	24	39	42	High clay content	Not found	$\omega \approx LL$ , $LL = 140\%$	<50	<5	0.48	0.78
13	Not found	Not found	Not found	Not found	Not found	Not found	45	60	Not found	Not found
14	Not found	3.70-17.10	Not found	Not found	Not found	Water table (WT)=1.60-5.95 m	4-30	2-10	Not found	0.12-4.28
15	Not found	Not found	Not found	Not found	Not found	Not found	100	Not found	Not found	Not found
16	7.62	22.86-24.38	Not found	Not found	Not found	Not found	45.72	17.98	0.17	0.5-0.53

Table A.7: Soil properties of the past sinkhole cases

No.	$H_l$	$H$	PI	Sand/silt?	Composition	Other	$\emptyset$	$d$	$H_l/\emptyset$	$H/\emptyset$
17	27.43- 45.72	36.58- 64.01	Not found	Not found	Not found	Low permeability	9.39	4.72	2.92-4.87	3.89-6.82
18	27	45	Not found	Not found	Not found	WT=30 m below the surface	107	30	0.25	0.42
19	1.8-2	9.2	Not found	Not found	Not found	$c' = 10$ kPa, $\phi = 29.5^\circ$ , $c_u = 150 - 450$ kPa	1.5-2	Not found	1-1.33	4.5-6
20	Not found	Not found	Not found	Not found	Chert debris	Not found	$\approx 6$	3	Not found	Not found
21	Not found	Not found	Not found	Not found	Chert debris	Not found	$\approx 6$	3	Not found	Not found
22	Not found	Not found	Not found	Not found	Chert debris	Not found	1-100	1-30	Not found	Not found
23	Not found	Not found	Not found	Not found	Chert debris	Not found	$\approx 30$	Not found	Not found	Not found
24	Not found	Not found	Not found	Not found	Chert debris	Not found	9-30	Not found	Not found	Not found

Table A.8: Soil properties of the past sinkhole cases

No.	$H_t$	$H$	PI	Sand/silt?	Composition	Other	$\emptyset$	$d$	$H_t/\emptyset$	$H/\emptyset$
25	Not found	Not found	Not found	Not found	Chert debris	Not found	0.3-6.1	0.6-3	Not found	Not found
26	<21.3	30.5-33.5	Not found	Not found	Not found	Not found	Not found	Not found	Not found	Not found
27	0.61	7.92 ( $H^*$ )	Not found	Not found	Not found	Not found	Not found	Not found	Not found	Not found
28	27	72	Not found	Not found	Not found	Not found	106	30	0.25	0.68
29	3-8	Not found	Low plasticity	Clay content: % < 2 $\mu m = 16 - 20$	Smectite, vermiculite, illite, chlorite	$\rho = 2.712 - 2.719 \text{ g/cm}^3$ , $LL = 26 - 30\%$ , $PL = 20 - 22\%$ , $\omega = 16.6 - 23.7\%$ , $\rho_d = 1.39 - 1.55 \text{ g/cm}^3$ , $s = 14 - 34 \text{ kPa}$	Not found	Not found	Not found	Not found
30	Not found	Not found	Not found	Not found	Not found	Not found	0.61-0.76 x 0.91-3.05	3.35-3.66	Not found	Not found

Table A.9: Soil properties of the past sinkhole cases

No.	$H_t$	$H$	PI	Sand/silt?	Composition	Other	$\emptyset$	$d$	$H_t/\emptyset$	$H/\emptyset$
31	4.57-12.2	4.57-12.2	Not found	Not found	Not found	Not found	91.44	60.96	0.05-0.67	0.05-0.67
32	3	Not found	Not found	Not found	Fossiliferous chert, limestone pebbles, limonite	Not found	Not found	Not found	Not found	Not found
33	8	8	Not found	Not found	Not found	Not found	15	Not found	0.53	0.53
34	19-21	15-23.5	Not found	Not found	Not found	Not found	15	14	1.27-1.4	1-1.57
35	11	11	Not found	Not found	Not found	WT at 13 m from the surface	Not found	Not found	Not found	Not found
36	11	11	Not found	Not found	Not found	Not found	Not found	Not found	Not found	Not found
37	Not found	Not found	Not found	Not found	Not found	Not found	30.48-38.10	12.19-13.72	Not found	not found
38	<10	Not found	Not found	Calcareous	Not found	10x5	Not found	1-2	Not found	Not found
39	Not found	Not found	Not found	Not found	Not found	Not found	Not found	Not found	Not found	Not found

Table A.10: Soil properties of the past sinkhole cases

No.	$H_t$	$H$	PI	Sand/silt?	Composition	Other	$\emptyset$	$d$	$H_1/\emptyset$	$H/\emptyset$
40	Not found	Not found	Not found	Not found	Not found	Not found	10	4-5	Not found	Not found
41	Not found	Not found	Not found	Not found	Not found	Not found	10-15	2	Not found	Not found
42	Not found	38	Not found	Not found	Not found	Not found	15	Not found	Not found	2.53
43	2-40	41	Not found	Not found	Chert content	Variable amount of chert and boulders, nodules and gravels. High $\omega$ (%)	22-62	0.2-5	0.03-1.81	0.66-1.86
44	22	Not found	Not found	Not found	Not found	Not found	10-30	20	0.73-2.20	Not found
45	Not found	Not found	Not found	Not found	Not found	Not found	35	6	Not found	Not found
46	Not found	Not found	Not found	Not found	Not found	Not found	2	Not found	Not found	Not found

Table A.11: Soil properties of the past sinkhole cases

No.	$H_t$	$H$	PI	Sand/silt?	Composition	Other	$\emptyset$	$d$	$H_1/\emptyset$	$H/\emptyset$
47	56	Not found	Not found	Not found	Not found	Not found	11	9	0.20	Not found
48	Not found	Not found	Not found	Not found	Not found	Not found	9	6-7	Not found	Not found
49	Not found	Not found	Not found	Not found	Not found	Not found	0.5-1.0	Not found	Not found	Not found
50	9.14-18.29	Not found	Not found	Not found	Not found	Very high $\omega$ close to the bedrock, dryer and stiffer soil above	Not found	Not found	not found	not found
51	7.62-15.24	Not found	Not found	Not found	not found	Voids in the soil	3.05 x 4.57	Not found	0.20-0.60	Not found
52	2.13-9.14	Not found	Not found	Not found	Not found	Not found	Not found	Not found	Not found	not found
53	1.52-3.05	3-4.9	Not found	Not found	Not found	Not found	30	1.8	0.05-0.10	Not found

Table A.12: Soil properties of the past sinkhole cases



## Appendix B

# Direct tensile test tables

The chapter reports the data found in the direct tensile tests on Kaolin, Durham and London clays.

The acronym used to identify the samples is explained below:

i. e. K\_300316\_b3

- The first letter indicates the type of clay studied. K is used for kaolin, DC for Durham clay and LC for London clay. The example quotes a sample of Kaolin.
- The first number reports the date of test. The sample of the example was tested on the 30th of March 2016.
- The last letter and number show the beam number. In the example, the direct tensile test was performed on the beam numbered 3.

## B.1 Tensile strength

### B.1.1 Kaolin

#	Test	Tensile strength $\sigma_t$ (kPa)	Moisture content $\omega$ (%)	Strain at max stress (%)
1	K_190116_b1	341.9	23.5	0.9
2	K_220116_b1	248.5	31.3	1.4
3	K_220116_b2	171.0	32.3	2.2
4	K_110316_b1	332.9	29.4	0.8
5	K_110316_b2	330.9	29.0	0.5
6	K_090316_b2	313.9	30.6	1.1
7	K_090316_b1	270.5	34.1	2.0
8	K_220316_b1	149.0	30.6	0.2
9	K_220316_b2	198.8	30.6	0.2
10	K_220316_b3	185.2	30.6	0.6
11	K_300316_b2	15.9	41.7	5.0
12	K_300316_b3	18.6	39.5	3.9
13	K_060416_b2	187.7	21.7	0.4
14	K_060416_b1	141.4	15.3	0.3

Table B.1: Tensile strength, moisture content and maximum strain for the kaolin tensile tests

## B.1.2 Durham clay

#	Test	Tensile strength $\sigma_t$ (kPa)	Moisture content $\omega$ (%)	Strain at max stress (%)
1	DC_100216.b1	136.2	18.8	0.5
2	DC_100216.b2	162.9	18.8	0.5
3	DC_230216.b1	12.6	40.6	0.4
4	DC_230216.b2	24.1	24.0	0.5
5	DC_230216.b3	16.4	26.9	0.4
6	DC_260216.b1	20.3	22.3	1.3
7	DC_260216.b2	35.4	21.1	0.7
8	DC_030316.b2	26.9	21.1	0.9
9	DC_030316.b3	9.9	24.1	1.1
10	DC_030316.b4	32.2	20.8	0.8
11	DC_030316.b5	16.9	23.8	1.8
12	DC_110316.b2	147.8	16.0	0.3
13	DC_290416.b1	190.6	14.0	0.7

Table B.2: Tensile strength, moisture content and maximum strain for the Durham clay tensile tests

## B.1.3 London clay

#	Test	Tensile strength $\sigma_t$ (kPa)	Moisture content $\omega$ (%)	Strain at max stress (%)
1	LC_020216.b1	440.3	24.9	1.6
2	LC_020216.b2	416.5	22.9	0.8
3	LC_080416.b2	353.7	24.6	0.9
4	LC_080416.b3	425.9	24.7	1.3
5	LC_080416.b4	402.5	24.4	1.0
6	LC_130416.b4	57.2	8.8	0.8
7	LC_150416.b3	466.8	25.1	1.3
8	LC_150416.b1	368.2	26.4	1.5
9	LC_150416.b2	392.9	26.2	1.2
10	LC_020616.b6	526.2	21.9	1.1
11	LC_070616.b9	618.8	22.3	1.0
12	LC_070616.b6	496.9	22.6	0.8
13	LC_090616.b1	83.3	29.1	1.1
14	LC_070616.b2	528.4	22.9	0.8
15	LC_090616.b5	55.5	29.5	0.8
16	LC_090616.b3	216.2	27.7	1.7

Table B.3: Tensile strength, moisture content and maximum strain for the London clay tensile tests

## B.2 Yield strength and Initial Young's modulus

### B.2.1 Kaolin

#	Test	Young's modulus $E_0$ (MPa)	Moisture content $\omega$ (%)	Yield strength $\sigma_{YS}$ (kPa)
1	K_190116_b1	129.0	23.5	73.8
2	K_220116_b1	85.3	31.3	48.4
3	K_220116_b2	56.1	32.3	28.2
4	K_110316_b1	106.0	29.4	105.0
5	K_110316_b2	214.5	29.0	45.7
6	K_090316_b2	127.0	30.6	90.3
7	K_090316_b1	37.4	34.1	92.2
8	K_220316_b1	152.2	30.6	86.4
9	K_220316_b2	134.4	30.6	76.4
10	K_220316_b3	97.6	30.6	54.8
11	K_300316_b2	1.6	41.7	1.2
12	K_300316_b3	0.7	39.5	3.8
13	K_060416_b2	124.5	21.7	133.8
14	K_060416_b1	47.9	15.3	53.9

Table B.4: Initial Young's modulus and yield strength for the kaolin tensile tests

**B.2.2 Durham clay**

#	Test	Young's modulus $E_0$ (MPa)	Moisture content $\omega$ (%)	Yield strength $\sigma_{YS}$ (kPa)
1	DC.100216.b1	32.8	18.8	67.9
2	DC.100216.b2	41.2	18.8	56.0
3	DC.230216.b1	10.5	40.6	2.3
4	DC.230216.b2	14.8	24.0	5.4
5	DC.230216.b3	10.2	26.9	5.1
6	DC.260216.b1	2.4	22.3	2.1
7	DC.260216.b2	13.9	21.1	15.8
8	DC.030316.b2	13.2	21.1	4.7
9	DC.030316.b3	2.7	24.1	2.1
10	DC.030316.b4	13.0	20.8	9.3
11	DC.030316.b5	1.8	23.8	1.4
12	DC.110316.b2	73.5	16.0	42.1
13	DC.290416.b1	22.4	14.0	36.8

Table B.5: Initial Young's modulus and yield strength for the Durham clay tensile tests

**B.2.3 London clay**

#	Test	Young's modulus $E_0$ (MPa)	Moisture content $\omega$ (%)	Yield strength $\sigma_{YS}$ (kPa)
1	LC_020216_b1	97.0	24.9	126.5
2	LC_020216_b2	104.6	22.9	121.2
3	LC_080416_b2	75.0	24.6	128.2
4	LC_080416_b3	64.5	24.7	123.8
5	LC_080416_b4	131.4	24.4	65.0
6	LC_130416_b4	7.8	8.8	38.6
7	LC_150416_b3	57.3	25.1	153.9
8	LC_150416_b1	30.9	26.4	76.8
9	LC_150416_b2	55.0	26.2	123.2
10	LC_020616_b6	81.4	21.9	127.1
11	LC_070616_b9	159.9	22.3	124.1
12	LC_070616_b6	85.5	22.6	114.3
13	LC_090616_b1	17.9	29.1	34.1
14	LC_070616_b2	104.1	22.9	109.9
15	LC_090616_b5	12.6	29.5	16.1
16	LC_090616_b3	64.5	27.7	123.8

Table B.6: Initial Young's modulus and yield strength for the London clay tensile tests



## Appendix C

# Bending test tables

The chapter reports the data found in the bending tests on Kaolin, Durham and London clays.

The acronym used to identify the samples is explained below:

i. e. K90d.0915.b12

- The first letter indicates the type of clay studied. K is used for kaolin, DC for Durham clay and LC for London clay. The example quotes a sample of Kaolin.
- The following number indicates the time in which the the sample dried in the oven. The letter d stands for ‘drying’. In the example the clay beam was dried for 90 minutes.
- The following number reports the date of test. The sample of the example was tested in September 2015.
- The last letter and number show the beam number. In the example, 3-point bending test was performed on the beam numbered 12.

## C.1 Flexural strength

### C.1.1 Kaolin

#	Test	Flexural strength $f_t$ (kPa)	Moisture content $\omega$ (%)	Strain at max force $\varepsilon$ (%)
1	K90d.0715_b10	74.9	39.1	1.2
2	K150d.0715_b7	128.1	33.2	1.0
3	K0d.0915_b8	16.0	47.8	1.4
4	K90d.0915_b5	74.9	39.1	1.2
5	K90d.0915_b4	105.5	38.7	1.1
6	K90d.0915_b2	122.4	38.2	1.1
7	K90d.0915_b13	121.0	36.8	1.1
8	K0d.0915_b2	22.3	45.2	1.3
9	K0d.0915_b1	14.7	46.6	1.4
10	K0d.0915_b4	18.00	46.8	1.4
11	K150d.0915_b6	210.1	32.4	1.0
12	K30d.0915_bD	43.8	41.6	1.2
13	K0d.0715_b7	33.9	44.8	1.3
14	K90d.0715_b1	122.3	36.5	1.1
15	K150d.0715_b4	145.7	34.0	1.0
16	K90d.0915_b12	120.2	36.4	1.1
17	K0d.0915_b2	15.2	47.1	1.4
18	K0d.1115_b2	37.8	45.0	1.3
19	K0d.1115_b4	48.4	45.1	1.3
20	K0d.1115_b5	37.5	44.9	1.3
21	K0d.1115_b6	35.1	44.8	1.3
22	K0d.1215_b4	86.4	40.1	1.2
23	K0d.1215_b5	78.4	40.7	1.2

*continued on next page*

<i>continued from previous page</i>				
#	Test	Flexural strength $f_t$ (kPa)	Moisture content $\omega$ (%)	Strain at max force $\varepsilon$ (%)
24	K0d.1215_b6	83.5	40.4	1.2
25	K0d.1215_b7	68.9	39.6	1.2
26	K0d.1215_b1	75.5	40.6	1.2
27	K0d.1215_b2	59.4	40.8	1.2

Table C.1: Peak loads, moisture contents and displacements at the point of maximum load for the kaolin bending tests

## C.1.2 Durham clay

#	Test	Flexural strength $f_t$ (kPa)	Moisture content $\omega$ (%)	Strain at max force $\varepsilon$ (%)
1	DC0d_1115_b13	8.9	26.4	0.6
2	DC0d_1115_b11	6.2	26.6	0.6
3	DC0d_1115_b12	10.8	26.4	0.9
4	DC0d_1115_b7	3.7	26.3	0.8
5	DC90d_1115_b8	90.5	18.7	0.6
6	DC90d_1115_b12	76.3	19.3	0.6
7	DC90d_1115_b2	61.9	19.3	0.6
8	DC90d_1115_b4	96.9	18.4	0.5
9	DC90d_1115_b10	96.3	18.2	0.5
10	DC90d_1115_b3	70.9	17.3	0.5
11	DC30d_1115_b3	44.8	22.4	0.5
12	DC30d_1115_b5	69.3	21.6	0.5
13	DC30d_1115_b6	59.2	21.4	0.6
14	DC30d_1115_b7	59.5	21.7	0.7
15	DC30d_1115_b10	54.5	21.6	0.6
16	DC30d_1115_b11	41.5	21.9	0.7
17	DC30d_1115_b13	64.3	21.7	0.4
18	DC0d_1115_b15	4.8	26.0	0.4
19	DC0d_1115_b14	3.2	26.6	0.2
20	DC0d_1115_b8	5.3	26.3	0.4
21	DC0d_1115_b6	7.6	25.8	0.8
22	DC0d_1115_b1	11.4	26.0	0.6
23	DC90d_1115_b15	71.1	17.7	0.4

*continued on next page*

<i>continued from previous page</i>				
#	Test	Flexural strength $f_t$ (kPa)	Moisture content $\omega$ (%)	Strain at max force $\varepsilon$ (%)
24	DC90d_1115_b14	83.1	18.9	0.4
25	DC90d_1115_b6	66.4	19.2	0.8
26	DC90d_1115_b5	67.2	18.3	0.4
27	DC90d_1115_b11	68.3	19.2	0.5
28	DC90d_1115_b9	97.5	17.0	0.5
29	DC30d_1115_b1	41.2	22.8	0.5
30	DC30d_1115_b2	43.8	22.5	0.5
31	DC30d_1115_b9	44.2	21.7	0.5
32	DC30d_1115_b14	51.7	21.6	0.5
33	DC30d_1115_b15	51.2	20.8	0.4

Table C.2: Peak loads, moisture contents and displacements at the point of maximum load for the Durham clay bending tests

## C.1.3 London clay

#	Test	Flexural strength $f_t$ (kPa)	Moisture content $\omega$ (%)	Strain at max force $\varepsilon$ (%)
1	LC0d_1115_b9	66.0	34.4	1.4
2	LC0d_1115_b5	78.0	37.4	1.5
3	LC0d_0116_b1	24.8	49.5	2.0
4	LC0d_0116_b2	21.3	50.0	2.0
5	LC0d_0116_b10	29.1	49.7	2.0
6	LC0d_0116_b8	20.6	50.6	2.1
7	LC45d_0116_b10	46.7	34.9	1.4
8	LC90d_0116_b9	64.5	32.5	1.3
9	LC0d_0116_b4	14.2	50.5	2.1
10	LC0d_0116_b7	13.4	50.2	2.1
11	LC0d_0116_b5	20.9	49.9	2.0
12	LC45d_0116_b7	40.5	36.2	1.5
13	LC90d_0116_b4	123.5	30.1	1.2
14	LC90d_0116_b3	139.6	30.5	1.2

Table C.3: Peak loads, moisture contents and displacements at the point of maximum load for the London clay bending tests